Retrieval of stratospheric aerosol characteristics from spaceborne limb sounders

Dissertation zur Erlangung des akademischen Grades des
Doktor der Naturwissenschaften
(Dr. rer. nat)

am
Fachbereich Physik und Elektrotechnik
der
Universität Bremen

vorgelegt von
Dipl.-Met. Elizaveta Malinina

1. Gutachter: Prof. Dr. John P. Burrows
2. Gutachter: PD Dr. Michael Höpfner

Datum des Kolloquiums: 26.03.2019

Bremen
2019

Abstract

Stratospheric aerosols play an important role in atmospheric chemistry and climate. In particular, information about the amount and distribution of stratospheric aerosols is required to initialize climate models, as well as validate aerosol microphysics models and investigate geoengineering. Besides, good knowledge of stratospheric aerosol loading is needed to increase the retrieval accuracy of key trace gases (e.g. ozone or water vapor), when interpreting remote sensing measurements of the scattered solar light. The most commonly used characteristic to describe stratospheric aerosols is the aerosol extinction coefficient (Ext), and there are several datasets providing this parameter in the stratosphere. However, it is well-known, that for the limb-scatter instruments, this parameter contains uncertainties due to the need to assume an aerosol particle size distribution (PSD) within the retrieval process. These uncertainties can be mitigated if PSD parameters are provided for each profile.

In this thesis, the methods to retrieve Ext and PSD parameters from the remote sensing instruments measuring the scattered solar light in the limb-viewing geometry are presented. The Ext retrieval algorithm is applied for Scanning Imaging Absorption Spectrometer for Atmospheric Chartography (SCIAMACHY) instrument, which was operating from 2002 till 2012, as well as for Ozone Mapper and Profiler Suite (OMPS) measurements, which started in 2012 and are conducted ever since. These products compose global stratospheric aerosol databases, which are covering over 16 years. Additionally, the aerosol PSD parameters are retrieved in the tropical region (20° N – 20° S) from SCIAMACHY limb measurements, creating a unique product.

SCIAMACHY Ext retrieval algorithm is improved since the previous version, and the obtained results are compared to the datasets from Stratospheric Aerosol and Gas Experiment (SAGE) II and Optical Spectrograph and InfraRed Imager System (OSIRIS) instruments. In the tropical region, the agreement between the instruments is within 20%, while in the high latitudes of both hemispheres the differences increase. This is related to the fixed PSD assumed in the retrieval. Retrieving the Ext profiles from SCIAMACHY and comparing them to SAGE II it is shown, that in the high latitudes the change of the PSD parameters within realistic values is responsible for up to 100% of the errors, while

for the tropical region the used PSD does not play a significant role. The Ext retrieval algorithm was applied as well to OMPS measurements, but the validation of the results is still ongoing.

Since the choice of PSD parameters influences the retrieved Ext, it was decided to develop an algorithm to retrieve PSD parameters. The algorithm is designed for SCIAMACHY limb measurements and uses the spectral information at seven wavelengths. There is a possibility to retrieve two out of three parameters of the assumed uni-modal lognormal aerosol PSD (mode radius (R_{mod}) and distribution width parameter (σ)) with this algorithm. The sensitivity studies show that limb measurements are much less sensitive to the third parameter (particle number density (N)). For that reason, N is fixed in the retrieval. Additionally, the sensitivity studies show that the limb instruments have a better potential for PSD retrieval than occultation ones, because the scattered solar light radiances are more sensitive to the smaller aerosol particles than the transmissions.

As N is fixed in the retrieval of the PSD parameters, an extensive error analysis was conducted through the synthetic retrievals. It is shown, that in the cases with unperturbed N, R_{mod} is retrieved with better than 20% accuracy, while σ is obtained with 5% accuracy. For the cases with perturbed N, the errors for R_{mod} are around 25% and for σ around 10%. Furthermore, such parameter as absolute distribution width (w) is implemented. The errors in w calculated from R_{mod} and σ are around 2% for the background cases, while for perturbed N they can reach up to 40%. Using Mie scattering theory the Exts and Ångström exponents were recalculated using the retrieved PSD parameters. The accuracy of these parameters is estimated to be within 25% for Ext and within 5% for Ångström exponent.

The retrieval algorithm is applied for SCIAMACHY data in the tropical region. Analysis of the dataset shows, that R_{mod} increases after volcanic eruptions, while w and Ångström exponent can increase, decrease or remain the same. It is also shown, that there is no simple relation between the Ångström exponent and the PSD because the same value of Ångström exponent can be obtained from an infinite number of combinations of the PSD parameters. The retrieved PSD parameters as well as recalculated Exts and Ångström exponents from SCIAMACHY limb measurements were compared to the other remote sensing instruments (SAGE II, OSIRIS) and in situ balloon-borne measurements from Optical Particle Counters (OPCs). The comparisons show good agreement and indicate the consistency of the results.

At the end of the thesis the case studies analyzing changes in Ext and PSD parameters after volcanic eruptions of Manam and Tavurvur are presented. Additionally, the evolution of Ext after eruptions of Sarychev Peak and Kelut as well as after Canadian Wildfires of 2017 is analyzed. It is shown, that tape-recorder effect is strong in the tropical region. If volcanic eruption occurred in the tropical region under certain dynamical conditions the equatorial plume serves as a reservoir for aerosols, which are transported polewards to both hemispheres with the Brewer-Dobson Circulation (BDC). For the extratropical eruptions, the volcanic perturbations usually stay at the hemisphere, where the eruption happened.

Publications

Peer-reviewed publications

Malinina, E., Rozanov, A., Rozanov, V., Liebing, P., Bovensmann, H., and Burrows, J. P.: Aerosol particle size distribution in the stratosphere retrieved from SCIAMACHY limb measurements, Atmos. Meas. Tech., 11, 2085-2100, https://doi.org/10.5194/amt-11-2085-2018, 2018.

Malinina, E., Rozanov, A., Rieger, L., Bourassa, A., Bovensmann, H., Burrows, J. P., and Degenstein, D.: Stratospheric aerosol characteristics from space-borne observations: extinction coefficient and Ångström exponent, Atmos. Meas. Tech. Discuss., https://doi.org/10.5194/amt-2018-328, in review, 2018.

Rieger, L. A., **Malinina, E. P.**, Rozanov, A. V., Burrows, J. P., Bourassa, A. E., and Degenstein, D. A.: A study of the approaches used to retrieve aerosol extinction, as applied to limb observations made by OSIRIS and SCIAMACHY, Atmos. Meas. Tech., 11, 3433-3445, https://doi.org/10.5194/amt-11-3433-2018, 2018.

Arosio, C., Rozanov, A., **Malinina, E.**, Eichmann, K.-U., von Clarmann, T., and Burrows, J. P.: Retrieval of ozone profiles from OMPS limb scattering observations, Atmos. Meas. Tech., 11, 2135-2149, https://doi.org/10.5194/amt-11-2135-2018, 2018.

Arosio, C., Rozanov, A., **Malinina, E.**, Weber, M., and Burrows, J. P.: Merging of ozone profiles from SCIAMACHY, OMPS and SAGE II observations to study stratospheric ozone changes, Atmos. Meas. Tech. Discuss., https://doi.org/10.5194/amt-2018-275, in review, 2018.

Conference contributions

Poster presentations

Malinina, E., Chubarova, N., Sviridenkov, M., Rozanov, A., Burrows, J. P.: Assessment of the aerosol loading based on the in-situ and remote sensing data, 8th Atmospheric Limb Workshop, Gothenburg, Sweden, 15-17 September 2015.

Malinina, E., Rozanov, A., Rozanov, V., Burrows, J. P., Bovensmann, H.: Aerosol particle size distribution in the stratosphere from SCIAMACHY limb measurements, 2nd SSiRC Workshop, Potsdam, Germany, 25-28 April 2016.

Malinina, E., Rozanov, A., Rozanov, V., Burrows, J. P., Bovensmann, H.: Stratospheric aerosols from SCIAMACHY-Limb measurements: particle size distribution, Living Planet symposium 2016, 9-13 May 2016, Prague, Czech Republic.

Arosio, C., Rozanov, A., Eichmann, K.-U., **Malinina, E.**, Burrows, J. P., Jaross, G., Bhartia P. K.: Retrieval of vertical distributions of stratospheric ozone from OMPS measurements in limb viewing geometry, Quadrennial Ozone Symposium, Edinburgh, UK, 4-9 September 2016.

Arosio, C., Rozanov, A., Eichmann, K.-U., **Malinina, E.**, Burrows, J. P., Jaross, G., Bhartia P. K.: Retrieval of ozone profiles from OMPS limb observations, DPG Frühjahrstagung, Bremen, Germany, 13-17 March 2017.

Arosio, C., Rozanov, A., Eichmann, K.-U., **Malinina, E.**, Burrows, J. P., Jaross, G., Bhartia P. K.: Retrieval of stratospheric ozone profiles from OMPS measurements in limb viewing geometry, European Geosciences Union General Assembly, Vienna, Austria, 23–28 April 2017.

Rozanov, A., **Malinina, E.**, Bovensmann, H., Burrows J. P.: Particle size distribution of the stratospheric aerosol from SCIAMACHY limb measurements, European Geosciences Union General Assembly, Vienna, Austria, 23–28 April 2017.

Rieger, L., **Malinina, E.**, Bourassa, A., Rozanov, A., Degenstein, D., Burrows, J. P.: Systematic errors in limb scatter aerosol retrievals, 9th Atmospheric Limb Workshop, Saskatoon, SK, Canada, 12-14 June 2017.

Malinina, E., Rozanov, A., Rieger, L., Rozanov, V., Liebing, P., Bovensmann, H., Bourassa, A., Degenstein, D., Burrows, J. P.: Stratospheric aerosol particle size distribution by SCIAMACHY limb measurements, Fall 2017 Virtual Poster Showcase, American Geophysical Union, Washington, DC, December 2017.

Malinina, E., Rozanov, A., Rieger, L., Rozanov, V., Bourassa, A., Degenstein, D., Bovensmann, H., Burrows, J. P.: Aerosol particle size distribution and extinction coefficients from SCIAMACHY limb measurements, Chapman conference Stratospheric aerosol

in the post-Pinatubo era: Processes, Interactions, and Importance, Puerto de la Cruz, Tenerife, Spain, 18-23 March 2018.

Arosio, C., **Malinina, E.**, Rozanov, A., Burrows, J. P.: Merging dataset of stratospheric ozone profiles from OMPS, SCIAMACHY and MLS limb observations, COSPAR 42nd Assembly, Pasadena, CA, USA, 14-22 July 2018.

Oral presentations

Rozanov, A., **Malinina, E.**, Rozanov, V., Hommel, R., Burrows, J. P.: Particle size distribution of the stratospheric aerosol from SCIAMACHY limb measurements, European Geosciences Union General Assembly, Vienna, Austria, 17–22 April 2016.

Malinina, E., Rozanov, A., Rozanov, V., Burrows, J. P., Bovensmann, H.: Particle size distribution of the stratospheric aerosol from SCIAMACHY: sensitivity studies and first results, Atmospheric Composition Validation and Evolution workshop, Frascati, Italy, 18-20 October 2016.

Rozanov, A., Arosio, C., **Malinina, E.**, Rozanov, V., Weigel, K., Bovensmann, H., Burrows, J. P.: Radiative transfer and retrieval in limb viewing geometry: the potential and challenges in transferring SCIAMACHY experience to the ALTIUS mission, First ALTIUS Symposium, Brussels, Belgium, 2-3 May 2017.

Malinina, E., Rieger, L., Rozanov, A., Rozanov, V., Bovensmann, H., Bourassa, A., Degenstein, D., Burrows, J. P.: Particle size sistribution of stratospheric aerosol retrieved from SCIAMACHY limb data, 9th Atmospheric Limb Workshop, Saskatoon, SK, Canada, 12-14 June 2017.

Arosio, C., Rozanov, A., **Malinina, E.**, Eichmann, K.-U., Burrows, J. P.: Retrieval of stratospheric ozone profiles from OMPS measurements in limb viewing geometry, 9th Atmospheric Limb Workshop, Saskatoon, SK, Canada, 12-14 June 2017.

Rozanov, A., Arosio, C., Eichmann, K.-U., **Malinina, E.**, Sofieva, V., Weigel, K., Rahpoe, N., Rozanov, V., Bovensmann, H., Burrows, J. P.: Remote sensing of the Earth's atmosphere in limb viewing geometry: recent developments at the University of Bremen, International Symposium om Atmospheric Radiation and Dynamic, Saint-Petersburg-Petrodvorets, Russia, 27-30 June 2017.

Malinina, E., Rieger, L., Rozanov, A., Rozanov, V., Bovensmann, H., Bourassa, A., Degenstein, D., Burrows, J. P.: Comparison of SCIAMACHY and OSIRIS aerosol products, SSiRC Workshop on Measurement of Stratospheric Aerosol, Boulder, CO, USA, 6-8 September 2017.

Malinina, E., Rozanov, A., Rieger, L., Rozanov, V., Bourassa, A., Bovensmann, H., Degenstein, D., Burrows, J. P.: Stratospheric aerosol characteristics retrieved from spaceborne observations in limb viewing geometry, COSPAR 42nd Assembly, Pasadena, CA, USA, 14-22 July 2018.

Malinina, E., Rozanov, A., Rieger, L., Bourassa, A., Degenstein, D., Bovensmann, H., Burrows, J. P.: Größenverteilung von stratosphärischen Aerosolen aus SCIAMACHY Limb Daten, 22. Deutsche Physikerinnen Tagung, Oldenburg, Germany, 27-30 September 2018.

Rozanov, A., **Malinina, E.**, Fussen, D., Burrows, J. P.: Particle size distribution of stratospheric aerosols: from SCIAMACHY to ALTIUS, ATMOS 2018, Salzburg, Austria, 26-29 November 2018.

Technical reports

Hommel, R., Burrows, J. P., Rozanov, A., Noel, S., **Malinina, E.**, Brinkhoff, L. A., Galytska, E.: Role of stratospheric aerosol in climate and atmospheric science (ROSA), Teilprojektspezifischer Schlussbericht des IUP, Universität Bremen, für das ROMIC-Verbundvorhaben, FKZ 01LG1212A, Technische Informationsbibliothek (TIB) Hannover, doi: 10.2314/GBV:881360309, 2017.

Acknowledgements

I never thought that I would write a PhD thesis in environmental physics, but here I am. This journey was exciting and tough, but I would never be able to complete it without the number of people who were advising, helping, teaching and inspiring me for the last three and a half years.

Firstly, I would like to thank Prof. John P. Burrows and Dr. Alexei Rozanov, who accepted me as a PhD student at the Institute of Environmental Physics, University of Bremen (IUP) and were guiding the whole time. Your encouragement, support, acceptance of sometimes not perfect results as well as constructive criticism motivated me to work harder and allowed me to succeed.

I am very grateful to be surrounded by wonderful people, working in the institute. In particular, I wanted to thank my officemate Carlo Arosio, who have prepared for me OMPS level 1 data and have shared the best and the worst moments of my research. Besides, I am very grateful to Tina Hilbig, Evgenia Galytska, Andrea Orfanoz-Cheuquelaf, Nora Mettig and Tobias Küchler who made the lunches as well as time outside the institute fun and entertaining. You have been a great support and help in particular in the last year of the of the studies.

Additionally, I wanted to thank Prof. Adam Bourassa and Prof. Doug Degenstein and all the colleagues in the Institute of Space and Atmospheric Studies of the University of Saskatchewan (USask) for hosting me as the guest researcher there. This three-months stay has been a big step in becoming an independent scientist. And I am deeply thankful to the Postgraduate International Programme in Physics and Electrical Engineering and the University of Bremen for providing a grant to visit the USask.

For the TOMCAT/SLIMCAT data, used in Ch. 9, my gratitude goes to Prof. Martyn Chipperfield.

I would also like to thank my mom and aunt for supporting my moving abroad. And the last, but definitely not least I am deeply grateful to Landon Rieger for being not only an amazing colleague in Bremen and Saskatoon and teaching me programming in Python, but also for being the most supportive and caring partner.

Motivation and outline

According to the Fifth Assessment Report of IPCC [2013] (Intergovernmental Panel on Climate Change) clouds and atmospheric aerosols contribute the largest uncertainty to the estimates and interpretations of the Earth's climate. While there is a substantial number of publications and initiatives related to the role of the tropospheric aerosols [e.g. Popp et al., 2016], the role of stratospheric aerosols is currently not well addressed. However, stratospheric aerosols have a significant influence on climate through two primary mechanisms. First, they scatter solar radiation and, during heavy aerosol loading conditions, absorb the thermal infrared radiation upwelling from the troposphere; thus, changing the radiative budget of the Earth, and resulting in tropospheric cooling and stratospheric warming. As mentioned by Thomason and Peter [2006], the radiative effects of stratospheric aerosols are negligible during volcanically quiescent periods. However, after even small eruptions the influence of stratospheric aerosols on the climate becomes significant [Solomon et al., 2011, Fyfe et al., 2013]. Furthermore, stratospheric aerosols play a crucial role in the stratospheric ozone depletion, which increases during the enhanced aerosol loading periods [Solomon, 1999, Ivy et al., 2017].

Accurate information about stratospheric aerosols is essential for different research fields. Among others, stratospheric aerosol parameters are needed for modeling the processes related to the stratosphere, including aerosol microphysics model validation. Modelers require stratospheric aerosol climatologies as initial conditions and/or validation sources for climate model simulations and predictions [e.g. Solomon et al., 2011, Fyfe et al., 2013]. All the above mentioned data is needed not only for improving global climate models but is also required for the investigation of geoengineering advantages and drawbacks. In addition, accurate knowledge of the stratospheric aerosol loading is essential in the retrieval of the stratospheric trace gases, e.g. water vapor [Rozanov et al., 2011b] and ozone [Arosio et al., 2018, Zawada et al., 2018], from remote sensing instruments.

There are many aerosol extinction coefficient (Ext) datasets retrieved from space-borne instruments measuring in occultation and limb viewing geometry [e.g. Bourassa et al., 2012, Damadeo et al., 2013, von Savigny et al., 2015, Vanhellemont et al., 2016, ACE-MAESTRO-Team, 2018], however the aerosol particles properties are rarely retrieved.

While algorithms to obtain some aerosol PSD parameters have been developed for the occultation instruments [Bingen et al., 2004, Thomason et al., 2008], for limb viewing instruments there have been only limited attempts to do it [Rieger et al., 2014]. For that reason, the main questions of this dissertation are, which stratospheric aerosol parameters can be retrieved from the space-borne observations of the scattered solar light, which assumptions need to be made and how these assumptions influence the final product.

For example, it is well known that the retrieval of Ext from the occultation measurements is straightforward, while multiple studies [e.g. Ernst, 2013, Loughman et al., 2018] show that retrieval of this parameter from limb-scatter instruments is dependent on the assumed PSD. These studies show the general dependency of the retrieved Ext on the PSD parameters, but lack an extensive evaluation of the error in the retrieved Ext due to the assumed PSD. To fill the gap in the scientific understanding of those errors, a high-quality product from the limb-scatter instrument is needed. This resulted in the improvement of the previously published [Ernst et al., 2012, Ernst, 2013, von Savigny et al., 2015] Ext retrieval algorithm from SCIAMACHY limb measurements, which is presented in the thesis. To validate the product, the Ext profiles were compared to ones from the occultation as well as other limb-scatter instruments. This enabled to answer the posed question. SCIAMACHY stopped its operation in 2012, which limits the possible analysis in time. Therefore, the developed Ext retrieval algorithm was applied to the measurements from the other limb viewing instrument, OMPS. The obtained product lacks calibration, and for that reason, its application is limited.

A related open scientific question is, whether it is possible to retrieve PSD parameters from the space-borne measurements in the ultraviolet (UV) – visible – near-infrared (NIR) spectral range. The existing datasets from the occultation measurements provide the values which differ by almost an order of magnitude, even being retrieved from the same instrument [see values in Bingen et al., 2004, Thomason et al., 2008]. The only known product from a limb-scatter instrument contains the Ångström exponent [Rieger et al., 2014], which is an empirical coefficient showing some correlation to the PSD [Ångström, 1929]. To answer the question, this thesis addresses the problems associated with the aerosol PSD parameter retrievals from the limb-scatter instruments as well as the difference in the sensitivity of limb and occultation instruments to the particle size parameters. As a result, in the thesis, the first retrieval algorithm yielding two out of three parameters of the aerosol PSD from the measurements of the scattered light in limb viewing geometry is presented. However, since it is possible to retrieve just two parameters, the assumptions on the third one need to be made. Therefore, the in-depth analysis of the errors resulting from this assumption is conducted.

Another geophysical question, which this thesis is focusing on, can be reformulated from Robock [2015]: what happens to stratospheric aerosols after a volcanic eruption? Is there an increase in the stratospheric aerosol parameters following a volcanic eruption? And how strong is this increase? Do the stratospheric aerosols from a volcanic eruption stay in the latitude band, where the eruption happened or are they transported over the globe? Those raised geophysical questions can be answered using the stratospheric aerosol products mentioned above. For this reason, in the thesis, the evolution of stratospheric aerosol parameters after some volcanic eruptions is analyzed.

Since the thesis covers a variety of topics and questions, it is split into four parts. The fundamental information on stratospheric aerosol is summarized in Part I. There is a brief historical overview as well as a description of sources and processes, related to stratospheric aerosol formation, evolution and transport. A summary of the role of stratospheric aerosol in climate as well as of aerosol parametrization are also presented in this Part. Furthermore, the datasets and the instruments used throughout the thesis and some basics of the radiative transfer theory are discussed.

In Part II the improved SCIAMACHY aerosol extinction coefficient retrieval algorithm as well as its adaptation to OMPS measurements are presented. The obtained global aerosol extinction coefficient datasets are analyzed. Additionally, SCIAMACHY aerosol extinction coefficients are compared with the results from occultation and another limb viewing instruments. In this Part, the dependency of the aerosol extinction coefficient retrieval from the limb-scatter instruments on the assumed PSD parameters is evaluated.

Part III is dedicated to the aerosol PSD retrieval algorithm and its implementation. An extensive study, covering the overall sensitivity of limb and occultation measurements to the PSD parameters, as well as an error estimation of the retrieved and recalculated parameters is provided. Tropical datasets of multiple PSD parameters are compared to the existing space-borne and in situ datasets.

The obtained aerosol extinction coefficient and PSD products are used to investigate the major enhanced aerosol loading events of the last one and a half decades. The results are presented in Part IV. At the end of the thesis, the summary and an outlook for the future studies are presented.

Contents

Part I.

Fundamentals

1 Stratospheric aerosols

1.1. Historical overview

The first documentations on the effects related to the changes in stratospheric aerosols are dated early 19th century. According to Oppenheimer [2003], who provided a substantial description of the consequences of a super-colossal volcanic eruption of Tambora in 1815, the largest volcanic eruption of the last millennium, paintings of J. M. W. Turner dated around 1816 were characterized by orange and red skies, which were inspired by the stratospheric optics, changed by the huge amount of stratospheric aerosols. Later in 1883, in a year of the colossal volcanic eruption of Krakatoa in Indonesia, it was again documented that the sunsets changed around the globe [Bishop, 1884]. Nevertheless, those were just the records of the responses to the change in stratospheric aerosol loading. The first measurements containing information on stratospheric aerosol loading, i.e. atmospheric optical extinction, started in 1883 in Montpelier and other sites in the Northern Hemisphere [Sato et al., 1993]. However, those measurements were conducted for the total column and were not directly related to the stratosphere.

The fundamental breakthrough in the stratospheric aerosol science happened in 1961 when Christian Junge detected and described in details the stratospheric aerosol layer. Using balloon-borne [Junge et al., 1961] and aircraft measurements, Junge and Manson [1961] formulated the theses, which are used until this day. For the study, they measured sizes of aerosol particles, and based on the collected data, proposed the shape of stratospheric aerosol PSD to be lognormal. They also measured total particle concentration and showed that the aerosol maximum is located in mid-latitudes between 15 and 23 km. This maximum was called later "Junge layer". The chemical analysis of aerosols showed that most of those are sulfuric; however, Junge and Manson [1961] did not indicate possible sources. A couple of years later after a paroxysmic eruption of Mount Agung in 1963 researchers showed that the stratospheric sulfur is coming from explosive volcanic eruptions [e.g. Hogg, 1963, Volz, 1964, Cronin, 1971]. Crutzen [1976] was the first who suggested that carbonyl sulfide (OCS) is a source of the background stratospheric aerosol layer.

Stratospheric aerosol characteristics started to be measured regularly since the early 1970s with the balloon-borne OPC and remotely by ground-based lidars. In the late 1970s, the first spaceborne missions were launched. More detailed information on the history of the observations can be found in Sect. (1.6).

Another important moment in the history of stratospheric aerosols was the proposal to use them in geoengineering. Budyko [1974] was the first, who suggested injecting with the airplanes sulfuric compounds in the stratosphere to mitigate the global warming. Many studies [e.g. Rasch et al., 2008] were conducted since, assessing the procedure and the amount of aerosols, which could be released. However, the idea has not been implemented yet, because of the possible negative effects (more detailed in Sect. 1.4).

1.2. Sources of stratospheric aerosols [1]

Most commonly, talking about stratospheric aerosols scientists mean spherical droplets composed of a mixture of sulfuric acid (H_2SO_4) and water (H_2O). Usually, the ratio of this mixture is 75% of H_2SO_4 and 25% of H_2O. Some studies show as well a presence of the non-sulfate material. For example, there is some amount of organic particles; other solid particles (incl. soot) can be released with a volcanic eruption or a significant biomass burning event. Meteoritic dust also seems to be present in the stratosphere. However, the amount of the non-sulfate material is noticeably smaller in comparison to the amount of the sulfuric aerosol. For that reason in this section, and in the dissertation in general, the emphasis will be put on the later one. A brief sketch representing the stratospheric aerosol sources and processes influencing their distribution is shown in Fig. 1.1.

The most important sources of stratospheric aerosols are carbonyl sulfide (OCS) and sulfur dioxide (SO_2) which are oxidized to H_2SO_4. If the conditions are favorable, short-lived sulfuric species like carbon disulfide (CS_2), dimethyl sulfide (DMS) and hydrogen sulfide (H_2S) also contribute to stratospheric H_2SO_4 production. It should be noted, that carbonyl sulfide and other sulfur compounds are firstly oxidized to SO_2, and then to H_2SO_4. Sulfur dioxide of any origin can dissolve in cloud, fog or rain droplets, and moist aerosols, where S_4^+ ($=[SO_2 \cdot H_2O]+[HSO_3^-]+[SO_3^{2-}]$) can be oxidized by various substances to S_6^+ ($=[H_2SO_4 \cdot H_2O]+ [HSO_4^-] +[SO_4^{2-}]$). The chemical cycle of the sulphuric compounds in the atmosphere is presented in Fig. 1.2.

OCS, the longest-lived and most abundant sulfur gas in the atmosphere, plays the primary role in the formation of the background stratospheric aerosol layer. Transported with the convection from the troposphere, OCS is oxidized to SO_2 and then to H_2SO_4. The primary direct sources of atmospheric OCS are the marine emissions of this gas. A noticeably smaller amount is coming from biomass burning, volcanic outgassing and its flux from the anoxic soils. According to Watts [2000], the smallest amount of directly emitted OCS is coming from anthropogenic activity (e.g. coal combustion, industrial sulfur recovery, cars emissions and aluminum production).

[1] Main literature sources: Kremser et al. [2016], Thomason and Peter [2006], Crutzen [1976].

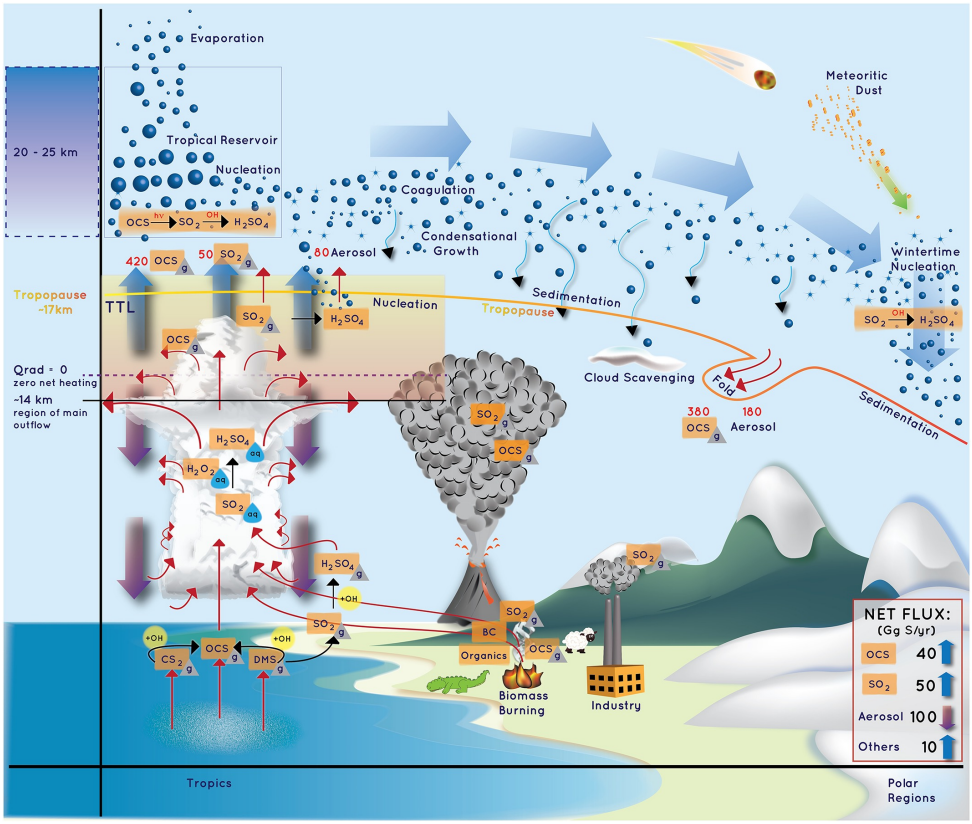

Figure 1.1. Schematic representation of the relevant processes that govern the stratospheric aerosol life cycle and distribution. Source: Kremser et al. [2016].

Opposite to the constantly emitted OCS, sulfur dioxide is the gas, which is responsible for the stratospheric aerosol variability. This is because SO_2 is primarily released with volcanic eruptions directly into the stratosphere, where it is oxidized to H_2SO_4. Since the influence of SO_2 on the stratospheric aerosols is so strong, scientists usually separate volcanically active and quiescent periods. The effect of colossal or super-colossal eruptions, e.g. Mount Pinatubo in 1991 or Tambora in 1815, can last multiple years; however, even smaller eruptions result in the increase of the stratospheric aerosol parameters for several months (some examples are presented in Chs. 5, 8 and 9). Sometimes SO_2 is not directly released into the stratosphere, but to the upper troposphere, and then it is dynamically transported to the higher atmospheric layers. Even though stratospheric aerosol precursors have predominantly natural sources, some studies show increased SO_2 from fossil fuel combustion transported to the lower stratosphere via the Asian monsoon [Randel et al., 2010].

Biomass burning of both, natural and anthropogenic origin, can also lead to an enhanced amount of stratospheric aerosols. The significant biomass burning events cause the formation of the convective clouds (PyroCb), which transport soot, SO_2 and OCS into the stratosphere. For example, multiple instruments registered the increase in the measured quantities during the Australian "Black Saturday" in 2009 [e.g Siddaway and Petelina, 2011] and Canadian Wildfires of 2017 [Khaykin et al., 2018] (some results are also presented in Sec. 9.4).

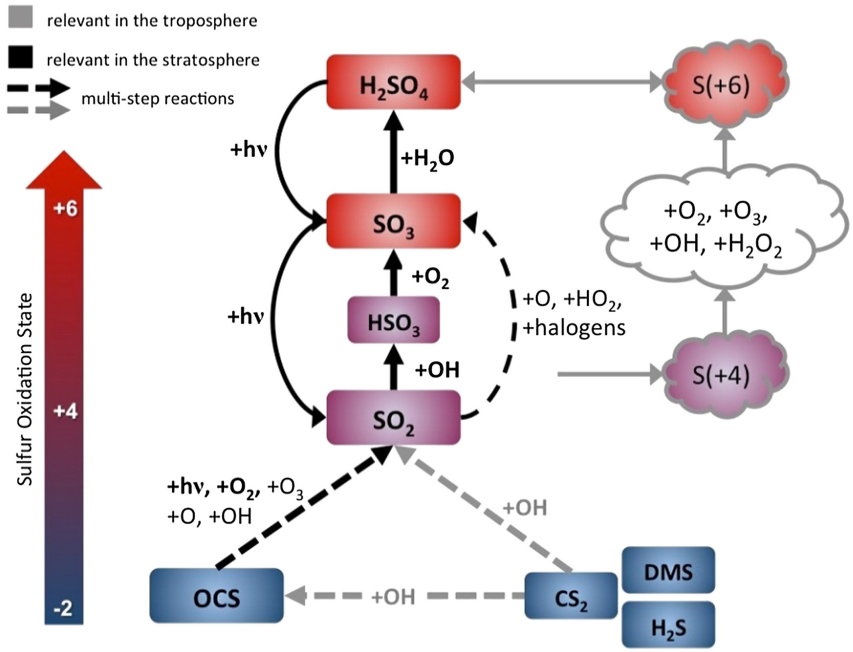

Figure 1.2. Primary atmospheric sulfur species and conversion reactions in gas (left part) and aqueous phase (right part). Grey arrows represent conversions mainly relevant in the troposphere, while black arrows indicate mainly stratospheric reactions. Important reactions are highlighted in bold. Several conversions involve multistep reactions (dashed) with intermediate products, which are not shown here. The color coding shows the oxidation state of the different sulfur compounds. Source: Kremser et al. [2016]

Short-lived sulfuric compounds are never transported to the stratosphere directly, but reacting with OH they are oxidized to OCS or SO_2 and then are transported with the deep convection to the stratosphere. The most significant sources of these compounds emissions are the ocean, anthropogenic activity, anoxic soils, wetlands and vegetation. Some amount of H_2S and C_2S can be released through volcanic outgassing [Watts, 2000].

1.3. Processes influencing stratospheric aerosol [1]

There are three types of processes influencing the stratospheric aerosol distribution: dynamical, chemical and microphysical. Chemical processes, responsible for the stratospheric aerosol formation were described in the previous section. In this section just the dynamical and microphysical process are taken into consideration. Most of these processes are schematically presented in the Fig. 1.1.

In the stratosphere the most important transport mechanism, responsible for air and trace constituents movement, is the Brewer-Dobson Circulation (BDC). Furthermore, the BDC is responsible for the exchange of the air between the troposphere and stratosphere, and thus for the transport of the sulfuric compounds from their sources to the stratosphere. The general BDC pattern is characterized by the rising air in the tropics, poleward flow

[1] Main literature source: Kremser et al. [2016].

in the stratosphere and sinking air at the high latitudes [Oberländer et al., 2013]. This general pattern is usually divided into shallow and deep branches. The shallow or lower branch moves the air within a few kilometers from the tropopause, with transport being stronger into the winter hemisphere. With the deep or upper branch air moves higher up to the upper stratosphere and mesosphere and descends over the winter pole [Trepte and Hitchman, 1992].

Additionally, aerosol transport is influenced by the secondary meridional circulation, which is associated with quasi-biennial oscillation (QBO). According to Holton [2004], QBO is identified by alternations in zonally symmetric easterly and westerly wind regimes on a time scale from 24 to 30 months. The QBO firstly appears at the altitudes above 30 km; however, it propagates downward to 23 km with a rate of 1 km per month. Trepte and Hitchman [1992] have noticed, that during the easterly phase of the QBO, equatorial aerosols are sequestered around the equator and are not as effectively transported towards the poles, instead they are moved vertically up. During the westerly phase the equatorial air is sinking, while the meridional motion is responsible for the subtropical air moving up. QBO usually does not affect the transport of the aerosol precursors, but the aerosols themselves, and its signatures in the aerosol parameters were reported in multiple publications [e.g. Trepte and Hitchman, 1992, Brinkhoff et al., 2015].

Another mechanism responsible for the transport of the aerosol precursors to the stratosphere is Asian Monsoon. In the Upper Troposphere Lower Stratosphere (UTLS) region, it contains a strong anticyclonic vortex over Asia and the Middle East. This anticyclone is characterized by a fast vertical transport from the polluted boundary layer with the deep convection confined with the strong anticyclonic circulation. On the eastern side of this anticyclone, a mean upward circulation extends the transport into the lower stratosphere, where the emitted by the anthropogenic activity SO_2 leads to the enhanced amount of stratospheric aerosol. In general, Asian Monsoon is considered to be a transport pathway for Asian pollution to the stratosphere [Randel et al., 2010].

To the microphysical processes, influencing the stratospheric aerosol number concentration and particle size distribution, belong such mechanisms as nucleation, coagulation, condensation, evaporation and sedimentation. Nucleation is responsible for the formation of the new aerosol. Thus, in the stratosphere the gaseous H_2SO_4 is generally supersaturated, which results in the quick H_2SO_4 condensation. Since water vapor is relatively abundant in the UTLS region, co-condensation of H_2SO_4 and water creates new aerosols through binary homogeneous nucleation. In the presence of condensation nuclei (e.g. meteoritic dust) heterogeneous nucleation occurs, even if the H_2SO_4 saturation ratio is not as high as in the condensation processes. The growth of the aerosol is regulated through coagulation and condensation. Coagulation, or the collision of the aerosol particles of various sizes and composition into one large particle, is mainly defined by aerosol number concentration. Coagulation, as well as nucleation, are relatively quick processes, while the condensational growth can last over the whole stratospheric aerosol lifetime. The later process is an uptake of water and H_2SO_4 by a particle, and it is dependent on the H_2SO_4 concentrations, its thermodynamic properties as well as on ambient temperatures. For the loss of stratospheric aerosols, evaporation and sedimentation are responsible. Evaporation mostly occurs in cases if an aerosol particle moves towards the warmer environment, and

then the particle changes its state from liquid to gaseous. The gravitational settling, or sedimentation, is noticeable in the situation when the aerosol particles are moved upwards by the BDC. The larger particles, obviously, are moved slower than the smaller ones, or in case, the particle is large enough it moves even downwards. Sedimentation is particularly important after larger volcanic eruptions when it is responsible for the vertical distribution of stratospheric H_2SO_4.

1.4. Climate influence

As it was noticed earlier, stratospheric aerosols play a highly important role in climate. Usually scientists emphasize two mechanisms of the climate influence: the first one is related to the radiative properties of the aerosol particles and the second is linked to the chemical processes, which lead to the ozone destruction.

Due to their physical properties, stratospheric aerosols scatter solar shortwave radiation back to space and absorb both, thermal infrared radiation from the troposphere and NIR solar radiation, which is especially noticeable during the strong aerosol loading conditions. This results in the changes in the Earth's radiative budget, and stratospheric warming and tropospheric cooling. The radiative forcing of stratospheric aerosols is negative for the typical background distribution, and it is even intensified during the increased load, e.g. after the volcanic eruptions. According to Self et al. [2004] Tambora eruption of 1815 caused a radiative forcing of -6 W/m^2 and about 1.0 - 1.5 K global cooling and "a year without summer" in 1816. By the estimates of Oppenheimer [2003] about 71 000 people died because of the eruption itself as well as from famine caused by cold summer and crops failure. The eruption of Mount Pinatubo in 1991 lead to -4 W/m^2 radiative forcing and a surface temperature cooling of 0.4 K [Robock and Mao, 1995]. But not only colossal volcanic eruptions influence the global temperature, according to Solomon et al. [2011], a series of smaller eruptions in 2000s decreased the radiative forcing by 0.1 W/m^2 and temperature by 0.07 K. Fyfe et al. [2013] concluded that due to the radiative changes not only temperature is affected by the volcanic eruptions, but also precipitation, sea level pressure and wind speed change in response to the changing aerosol load. Furthermore, it is important to mention, that stratospheric aerosols also change the color of the sky. Thus, the increased amount of aerosols leads to the sky whitening and spectacular red and orange sunsets, happening due to the changed optics [Crutzen, 2006]. Exactly these changes in sunsets color were the first documented observations in stratospheric aerosol changes after Tambora and Krakatoa eruptions (see Sect. 1.1).

Stratospheric aerosols are also involved in the ozone chemistry. In the polar regions, stratospheric aerosols are the precursors of Polar Stratospheric Clouds (PSCs) on whose surface heterogeneous chlorine activation and denitrification processes take place, resulting in the strong ozone depletion [Solomon, 1999]. Additionally, the ozone loss in polar and midlatitudes after the volcanic eruptions which release a large amount of stratospheric aerosols is related to the same heterogeneous reactions but on the liquid aerosol surfaces. That happened, for example, after Pinatubo eruption of 1991 [Solomon, 1999, Crutzen,

2006]. The more recent example is related to the Calbuco eruption in Chile in 2015 [Ivy et al., 2017].

The cooling properties of stratospheric aerosols lead to the proposal to use them for geoengineering. Budyko [1974] was the first, who suggested ejecting sulphuric particles into the stratosphere to mitigate global warming, caused by an increase in greenhouse gases concentrations. For over 40 years passed after that proposal, a lot of studies were conducted, assessing the way, height, amount and particular sulfur compounds to be released [e.g. Rasch et al., 2008]. As Crutzen [2006] suggested in his essay, the question of geoengineering should be studied deeply with all possible positive and negative responses to be considered. However, geoengineering should not necessarily be implemented. Firstly, not all the effects of increased CO_2 will be mitigated with geoengineering, and secondly, unexpected climate consequences should not be underrated.

1.5. Aerosol parametrization [1]

Stratospheric aerosols are usually characterized by their PSD or by the optical properties, such as Ext and/or the related parameters.

A balance of the described in the previous sections processes, which are responsible for creation and removal of the stratospheric aerosols, as well as of the processes influencing the size of aerosol particles commonly results in a size distribution which is well described by a single or multiple mode lognormal shape [e.g Hansen and Travis, 1974]. According to Crow and Shimizu [1988] and Thomason and Peter [2006], lognormal distributions are used to describe stratospheric aerosol particles, because these distributions typically fit the data very well. Furthermore, these distributions are convenient mathematically, because the function, as well as the distributed parameter, always remain positive. Lognormal PSD is used not only for stratospheric aerosols, but for the atmospheric aerosols in general. For example, in the retrievals of the aerosol column properties from the Aerosol Robotic Network (AERONET) a bimodal lognormal PSD is considered [Dubovik et al., 2000].

For the stratosphere, in some cases a bimodal PSD is assumed, e.g. Deshler et al. [2003] uses it to achieve the best approximation to their measurements from in situ OPCs. However, this approach is not suitable for the remote sensing instruments working in the limb or occultation geometry. This is because six independent pieces of information at each altitude level are needed to describe a bimodal lognormal PSD, while measurements from spaceborne instruments commonly provide two to three parameters per altitude level [Bingen et al., 2004, Thomason et al., 2008, Rieger et al., 2014]. Even for the Ext retrievals from the spaceborne instruments unimodal distributions seem to be more suitable. Thus, Loughman et al. [2018] used bimodal lognormal distribution for Ext product V1.0 from OMPS instrument, but for the improved V1.5 of this product Chen et al. [2018] suggests the use of gamma distribution instead. The authors claim, that this distribution showed better results in comparison with SAGE III/ISS. Although the use of gamma distribution

[1] Formulas were partially taken from Johnson et al. [1994], Grainger [2018].

for aerosol PSD is arguable, the study shows, that the use of unimodal distribution is more suitable. Generally, the coarse mode of the distribution can be neglected, because it is remarkably small in comparison to the fine mode. The coarse mode is especially small during the volcanically quiescent periods [Deshler, 2008].

Throughout the thesis, when talking about PSD, the unimodal lognormal shape is considered:

$$\frac{dn}{dr} = \frac{N}{\sqrt{2\pi}\ln(\sigma)r}\exp\left(-\frac{(\ln(r_{med})-\ln(r))^2}{2\ln^2(\sigma)}\right), \tag{1.1}$$

where N is the aerosol particle number density, r_{med} is the median radius and $\ln(\sigma)$ is the standard deviation of the $\frac{dn}{d\ln(r)}$ function. Though the median radius (r_{med}) is directly used in the formula and indicates the maximum of $\frac{dn}{d\ln(r)}$ distribution, discussing the shape of aerosol PSD it is more convenient to work with the R_{mod}:

$$R_{mod} = r_{med}/\exp(\ln^2(\sigma)), \tag{1.2}$$

which determines the maximum of $\frac{dn}{dr}$ distribution and, thus, is more evident for the interpretation of results. Furthermore, discussing the PSD a representation of the w by the standard deviation of the $\frac{dn}{dr}$ distribution will be used:

$$w = \sqrt{r_{med}^2\exp(\ln^2(\sigma))(\exp(\ln^2(\sigma))-1)}. \tag{1.3}$$

For visual interpretation, w is more convenient than σ, as the latter is defined relative to the r_{med} parameter. In the thesis, σ is used when describing retrieval settings, while w is used when discussing the aerosol PSD retrieval results.

In some studies [e.g. Grainger et al., 1995, Thomason et al., 2008], such parameter as effective radius (r_{eff}) is considered. r_{eff} is essentially the ratio of the third moment of the PSD to the second moment, and for the unimodal lognormal distribution is defined as:

$$r_{eff} = r_{med}\exp(2.5\ln^2(\sigma)). \tag{1.4}$$

Providing the formulas of the different distributions, [Grainger, 2018] stated, that r_{eff} could be quite useful, because the energy removed from a light beam by a particle is proportional to the particle's area, which is described by r_{eff}.

Discussing optical characteristics of stratospheric aerosols, Ext is usually meant. At the wavelength λ it is defined as

$$Ext_\lambda = \beta_{aer}(r_{med}, \sigma, \lambda...)N, \tag{1.5}$$

where β_{aer} is the aerosol extinction cross section, which is dependent on the aerosol PSD [e.g. Liou, 2002]. If Ext is obtained independently at least at two wavelengths, some limited information about PSD can be provided by the Ångström coefficient or Ångtröm exponent (α), which was used in the empirical relation introduced by Ångström [1929]:

$$\frac{Ext_{\lambda_1}}{Ext_{\lambda_2}} = \left(\frac{\lambda_1}{\lambda_2}\right)^{-\alpha}. \tag{1.6}$$

The usage of α, however, is associated with certain issues. In his work Ångström [1929] noted that the diameter of the particles calculated from α shows only an approximate coincidence with the average aerosol diameter directly measured. Furthermore, he stated, that the changes in the size of the particles do not necessarily lead to the changes in α. Another complication is related to the fact, that the α value changes depending on the wavelength pair used for its calculation [e.g. Rieger et al., 2015].

In general, if all three parameters of the unimodal lognormal PSD are provided, the optical parameters can be calculated very accurately using Mie scattering theory [Mie, 1908]. From the optical parameters, however, it is hard to do the opposite. Nevertheless, sometimes Ext is provided because of the lack of information. Additionally, due to the specifics of the measurements, for the instruments employing the occultation measurement technique, firstly Ext is retrieved and then based on this information, PSD parameters are obtained. This results in a situation, that the aerosol PSD databases are quite rare, with Ext databases being widely spread. More information on the existing stratospheric aerosol databases and the corresponding measurements is presented in the next section.

1.6. Measurements of stratospheric aerosols

As it was mentioned in Sect. 1.1 regular measurements of the stratospheric aerosol parameters with the methods which are used until today started in the 1970s. As most of the atmospheric species, stratospheric aerosols can be measured in situ and remotely from the different platforms (ground-based, balloons/aircraft or spaceborne). In this section, just the continuous datasets which cover or are planned to cover over two years were taken into consideration. All datasets described below are depicted in Fig. 1.3, which is a time chart, indicating start, end and duration of the measurements. Figure 1.3 ends at the end of 2018, thus the planned missions were not shown there. Color coded are the used measurement techniques.

The most important and the longest in situ observation series is the one from the balloon-borne OPC in Laramie, Wyoming. These observations started in 1971, continue to be done regularly until nowadays and planned to be conducted in the future for unlimited time. OPCs provide highly vertically resolved information on stratospheric aerosol PSD. Depending on the amount of the independent measurements, unimodal or bimodal PSD is applied [Deshler et al., 2003]. The OPCs and the retrieval algorithm are constantly improved. Recently the University of Wyoming group revised their retrieval algorithm and started to reprocess the data; however, it is still work in progress [Deshler et al., 2018]. Occasional measurement campaigns with the OPC launches were done over the years in different sites all over the globe, however the Laramie dataset is considered to be the reference.

Long-term ground-based remote sensing measurements are obtained as well from lidars. Lidars measure aerosol backscatter, which is afterwards converted to Ext with the assumption of the extinction-to-backscatter ratio, which varies depending on the situation. If a lidar makes measurements at more than one wavelength, there is a possibility to

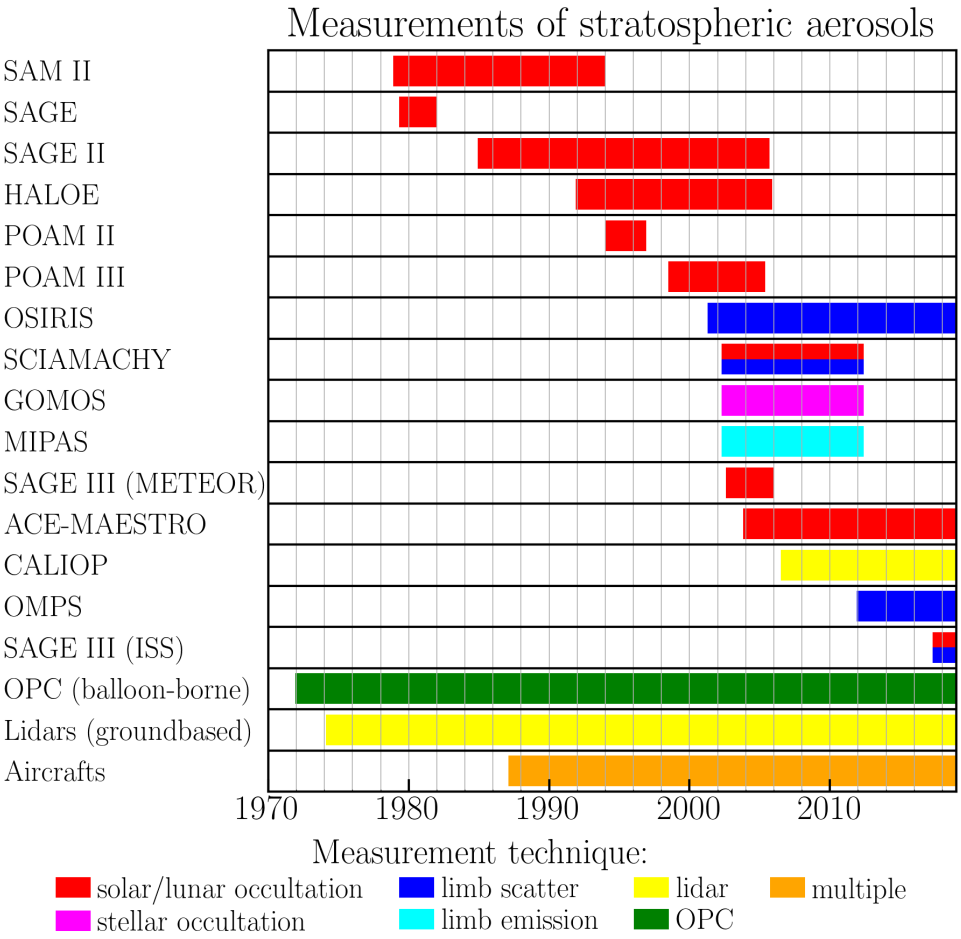

Figure 1.3. Available stratospheric aerosol records between 1970 and 2019. At the figure only the missions operated more than 2 years are shown. Color coded are the different measurements techniques.

obtain some PSD parameters. From the specifics of the measurement technique, lidar observations are limited to the nighttime, providing very high vertical resolution (about 75 m) [Jäger, 2005]. Two longest and continuous datasets of the aerosol backscatter are provided from the instruments in Garmisch-Partenkirchen in Germany [Jäger, 2005] and at the Mauna Loa Observatory in Hawaii [Hofmann et al., 2009]. The observations in these sites started in 1975 and 1974 respectively and are conducted until today.

The airborne measurements are represented by both, in situ and remote sensing observations. Usually, PSD parameters, aerosol concentrations or compositions are reported. From some aircraft campaigns, where lidars were used, aerosol backscatter is provided [Thomason and Peter, 2006]. One of the most remarkable system is Civil Aircraft for Regular Investigation of the Atmosphere Based on an Instrument Container (CARIBIC), which operates from 1997 until today. In these campaigns the measurements are done on board the commercial Lufthansa aircrafts in the routes from Germany. Aerosol PSD is measured with the condensation particle counters, and additionally its composition is assessed after the flights by the analysis of the impactors [Brenninkmeijer et al., 2007]. Another example of the long-term in situ measurements aboard aircrafts are the measurements of the aerosol PSD supervised by the University of Denver. At the Workshop on the

Measurement of Stratospheric Aerosol Willson et al. [2017] mentioned the existence of the dataset from 1987 until nowadays. Even though the instrumentation was changed over the years (in the beginning the measurements were done with Focused Cavity Aerosol Spectrometer (FCAS) and now they are done with the Ultra-High Sensitivity Aerosol Spectrometer (UHSAS)), both instruments provide the same parameters. The major disadvantage of the in situ aircraft measurements is related to the maximal measurement altitude, thus, usually the aircraft observations are done in the UTLS region.

In situ measurements as well as ground-based or airborne lidars among others have the disadvantage of the limited spatial and temporal coverage. Therefore satellite observations are commonly used to obtain knowledge about the global behavior of stratospheric aerosols. Spaceborne measurements of the stratospheric aerosols started in the late 1970s with the launch of the solar occultation instruments Stratospheric Aerosol Measurement (SAM) II (1978-1993) and SAGE (1979-1981). These instruments provided Ext at 1000 nm, with SAGE measuring additionally at 450 nm. Later, in 1984 SAGE II started operation (details on the technical specifications of the instrument can be found in Sec. 2.4). Until nowadays this instrument is considered to be one of the most reliable missions of the occultation measurement era; it provided high-quality data for over 20 years period and is often used for merging and comparison activities. As SAGE II provided Ext information at four wavelengths, some information on PSD was retrieved by the National Aeronautics and Space Administration (NASA) team [Damadeo et al., 2013], as well as by Bingen et al. [2004]. Less known solar occultation instruments, providing Ext information, were Halogen Occultation Experiment (HALOE), Polar Ozone and Aerosol Measurement (POAM) II and POAM III.

At the beginning of 2000s several spaceborne instruments of a newer generation using stellar occultation and limb measurement techniques were launched. In the late 2001 Odin satellite with OSIRIS instrument on-board was launched, and it operates until today. Based on the OSIRIS measurements of scattered solar light in the limb viewing geometry aerosol extinction profiles and Ångström exponents were retrieved (more detailed the instrument and its products are described in Sect. 2.3). Less than a year later several instruments on board Environmental satellite (Envisat) started observations. The satellite operated from 2002 till 2012, and among the scientists this decade is usually called the "golden era of stratospheric observations". One of the Envisat instruments was SCIAMACHY, it had three main measurement modes: nadir, solar/lunar occultation and limb scattering (see Sect. 2.1). Other instruments on board Envisat providing stratospheric aerosol information were Global Ozone Monitoring by Occultation of Stars (GOMOS) and the Michelson Interferometer for Passive Atmospheric Sounding (MIPAS). GOMOS made measurements using the stellar occultation technique; its aerosol product provides Ext at multiple wavelengths [Vanhellemont et al., 2016] and the Belgian Institute for Space Aeronomy (BIRA) group is working on PSD product. The MIPAS instrument measured limb emission spectra [Fischer et al., 2008] and provides vertical profiles of SO_2 and sulfate aerosol (H_2SO_4) volume densities [Günther et al., 2018].

A Canadian Atmospheric Chemistry Experiment (ACE) mission with the Measurement of Aerosol Extinction in the Stratosphere and Troposphere Retrieved by Occultation (MAESTRO) instrument on board started its operation in 2003 and continues to pro-

vide the data until the time of writing. The latest MAESTRO product v3.13 reports Ext at multiple wavelengths [ACE-MAESTRO-Team, 2018].

The most recent instrument, which combines nadir and limb scattering measurements, is the OMPS (the detailed description in Sect. 2.2). OMPS was launched by NASA at the end of 2011 and is still in operation. First results with respect to the retrievals of Ext from this instrument were presented in several publications [Taha et al., 2011, Arosio et al., 2018, Loughman et al., 2018, Chen et al., 2018].

The only known instrument providing aerosol backscatter, which is afterwards converted to the aerosol extinction coefficient, is the space-based lidar Cloud-Aerosol Lidar with Orthogonal Polarization Lidar (CALIOP). Profiles of the Ext from CALIOP have the highest vertical resolution among the spaceborne instruments, but relatively sparse horizontal sampling [Vernier et al., 2011].

2 Instruments

2.1. SCIAMACHY[1]

Scanning Imaging Absorption Spectrometer for Atmospheric Chartography (SCIAMACHY) was a joint German, Dutch and Belgian instrument on board Environmental satellite (Envisat), which was launched by European Space Agency (ESA) on 1 March 2002. The satellite operated in a sun-synchronous orbit at 800 km altitude with a 10:00 a.m. descending node equator-crossing time from August 2002 till April 2012, when the communication with it was suddenly lost. SCIAMACHY operated in three observational modes: nadir, limb and solar/lunar occultation. Additionally, the solar irradiance was measured daily. Measurements were taken in 8 spectral channels, covering the spectral interval between 214 and 2386 nm with spectral resolution varying from 0.2 to 1.5 nm depending on the wavelength. SCIAMACHY had a scanning mirror mechanism: the incoming radiation was directed to a predisperser prism, where it was separated to the channels, and then with the help of a grating was directed to the charge coupled device (CCD).

In order to obtain information on stratospheric aerosols, measurements in the limb viewing geometry were used. In this measurement geometry, the atmosphere was scanned tangentially to the Earth's surface from about 3 km below the horizon, i.e., when Earth's surface is still within the field of view of the instrument, up to about 100 km above the ground. The measurements were taken with a vertical step of 3.3 km and vertical instantaneous geometrical field of view at the tangent point of 2.6 km. The horizontal cross-track field of view of the instrument was 110 km, and a horizontal scan was performed during each observation sequence with the total swath of about 960 km. The horizontal cross-track resolution was mainly determined by the integration time during the horizontal scan, usually reaching about 240 km. For a typical limb measurement, there were four independent limb radiance profiles obtained during one horizontal scan as a result of the fact that the observed signal integrated by the instrument was read out

[1] Main literature sources: Burrows et al. [1995], Bovensmann et al. [1999], Gottwald and Bovensmann [2011].

four times per horizontal scan. The horizontal along-track resolution is estimated to be about 400 km. SCIAMACHY solar scattering angle (SSA), or the angle between the direction to the Sun and line of sight of the instrument, has a strong latitudinal dependency and ranged from 30° in the high latitudes of the northern hemisphere to 150° in the high latitudes in the southern hemisphere. The sketch of SCIAMACHY measuring in the limb viewing geometry is presented in Fig. 2.1.

From SCIAMACHY limb measurements, information on clouds and their top height [Eichmann et al., 2016] as well as vertical profiles of ozone (O_3)[Jia et al., 2015], nitrogen dioxide (NO_2) [Bauer et al., 2012], bromine monoxide (BrO) [Rozanov et al., 2011a], chlorine dioxide (OClO) [Kühl et al., 2008], water vapor (H_2O)[Weigel et al., 2016] and stratospheric aerosols parameters were obtained. The retrieval algorithms of the aerosol extinction coefficient (Ext) and PSD parameters are presented in Ch. 4 and 6 respectively.

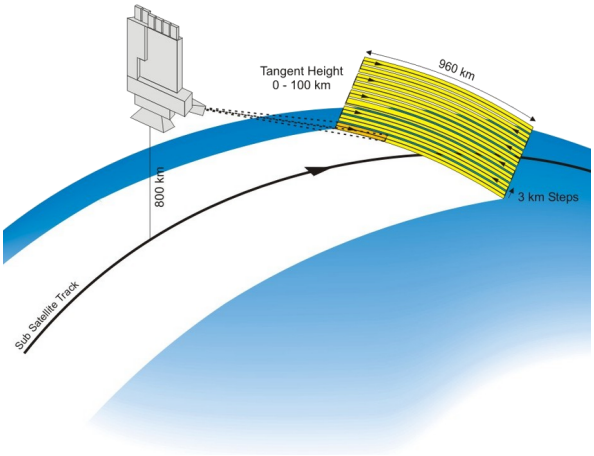

Figure 2.1. Sketch of SCIAMACHY limb measurements. Source: Noël et al. [2002]

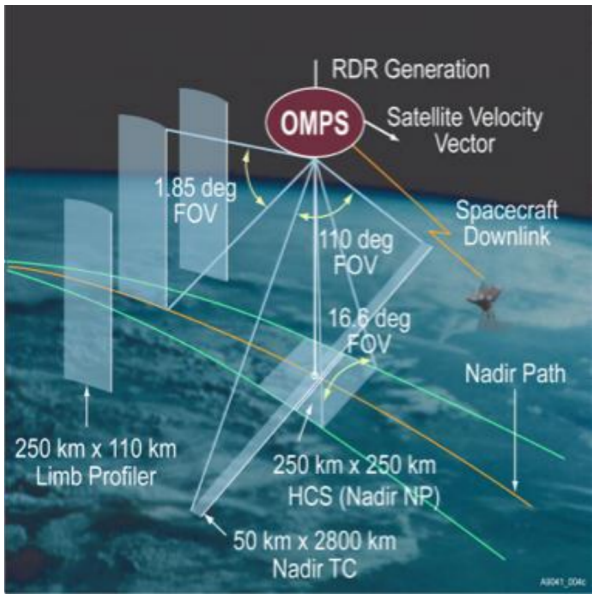

Figure 2.2. Sketch of OMPS measurements. Source: Bhartia et al. [2013]

2.2. OMPS[1]

On 28 October 2011 NASA launched Suomi National Polar-orbiting Partnership (SNPP) spacecraft with Ozone Mapper and Profiler Suite (OMPS) instrument on board. SNPP has a sun-synchronous orbit at about 833 km altitude and 13:30 ascending node equator-crossing time. The instrument started to collect the data in January 2012 and continues measurements by the time of writing. OMPS has three measurement components: nadir profiler, nadir mapper and limb profiler. The instrument registers solar irradiance scattered by the atmosphere in the wavelength range from 290 to 1000 nm, and since OMPS uses a prism disperser the spectral resolution varies from 1 nm in the UV part of the spectrum to 30 nm in the NIR.

[1]Main literature sources: Jaross et al. [2014], Loughman et al. [2018].

Originally, OMPS was designed to provide the ozone measurements, but it is also possible to obtain stratospheric aerosol characteristics from the limb profiler. OMPS uses a two-dimensional CCD detector instead of the scanning mirror mechanism, and thus, the instrument simultaneously captures the spectrally dispersed photons and their vertical distribution. The limb instrument has three vertical slits, which are separated horizontally from each other by 4.25° or 250 km at the Earth's surface. The radiances are registered with the vertical sampling of 1 km at tangent point (TP), and the instantaneous field of view of each detector pixel is 1.5 km. The instrument registers vertically 105 pixels, although the upper maximum and lower minimum tangent altitudes vary depending on the latitude and season with the altitudes from 5 to 80 km being continuously covered. Similar to SCIAMACHY, OMPS has the SSAs varying from 30° to 150° depending on the latitude. Horizontally the measurements are separated from each other by about 125 km. The measurements of OMPS on the orbit are presented schematically in Fig. 2.2.

OMPS measurements are used by multiple groups, thus, at multiple conferences, NASA reports the existence of cloud top height and ozone products. There was also a paper published with the official stratospheric *Ext* retrieval at 675 nm [Loughman et al., 2018]. The USask group created the tomographic ozone retrieval algorithm [Zawada et al., 2018]. IUP provides their own ozone and aerosol retrieval algorithms [Arosio et al., 2018]. The stratospheric aerosol retrieval algorithm, as well as the results, can be found in the following chapters.

2.3. OSIRIS[1]

On 20 February 2001 ESA launched Swedish satellite Odin with Optical Spectrograph and InfraRed Imager System (OSIRIS) instrument on it. Odin has a sun-synchronous orbit at about 600 km altitude with 06:00 a.m. descending node equator crossing-time. OSIRIS began to provide continuous measurements in November 2001 and still operates by the time of writing. OSIRIS is a limb instrument consisting of two parts. The first one, optical spectrograph, takes measurements of the scattered solar light in the spectral interval from 214 to 810 nm with 1 nm spectral resolution. The optical spectrograph is a grating spectrometer similar to SCIAMACHY: it scans the atmosphere tangentially to the Earth's surface in the altitude range from around 7 to 65 km with a vertical sampling of 2 km and vertical resolution of 1 km. OSIRIS does not have a scanning mirror; instead, Odin nods up and down through an angle of 1°– 2°, and this provides information on the vertical structure of the atmospheric composition [McLinden et al., 2012]. The second instrument is the infrared imager employing a different measurement technique: it consists of three vertical photodiode arrays with 128 pixels each and filters at 1260, 1270 and 1530 nm respectively. At the particular altitude a line of sight is measured by each pixel, and thus with each exposure, the entire vertical profile covering around 100 km is created. The rough sketch of OSIRIS measurements is presented in Fig. 2.3.

[1]Main literature source: [Llewellyn et al., 2004].

Among others, OSIRIS was designed to provide the information on the level of anthropogenic changes in the atmospheric environment, thus, in the stratosphere such species as ozone [Bourassa et al., 2018], nitrogen dioxide [Bourassa et al., 2011] and stratospheric aerosol characteristics [Bourassa et al., 2012, Rieger et al., 2014] were retrieved.

In this thesis, OSIRIS is used as an instrument for the comparison, and both currently available stratospheric aerosol products v5.07 [Bourassa et al., 2012] and v6.0 [Rieger et al., 2014] are taken into consideration.

Generally, the Ext retrieval algorithms from any limb-scatter instrument work as follows, first, the aerosol PSD is assumed, then with the radiative transfer model (RTM) the intensities at the desired wavelength are modelled, after that using inversion techniques, the modelled intensities are fitted to the measured ones and the Ext is obtained. In v5.07 in order to provide Ext_{750} from OSIRIS, the USask group used the inversions with RTM SASKTRAN [Zawada et al., 2015] and multiplicative algebraic reconstruction technique (MART). The radiative transfer modelling is conducted by assuming the lognormal PSD with r_{med}=0.08 μm and σ=1.6. In the algorithm the radiances at 750 nm are additionally normalized to the radiance at 470 nm and to the radiance at some upper measurement altitude. This altitude is determined individually for each scan by subtracting from the normalized radiance the normalized modelled radiance with the assumption of the aerosol-free atmosphere and searching the minimum of their difference. Thus, the normalization altitude varies from 25 to 40 km, depending on the latitudes. The Ext retrieval is coupled with the albedo retrieval at 675 nm, assuming the later one to be constant with the wavelength.

For v6.0, Ext_{750} as well as Ångström exponent ($\alpha_{750/1530}$) were retrieved using the same RTM but optimal estimation (OE) and the Levenberg–Marquardt algorithm instead of MART. To obtain $\alpha_{750/1530}$ the information at one wavelength of the optical spectrograph (750 nm) as well as measurements at 1530 nm from the infrared imager were used. As a reference spectrum the measurement at the higher tangent altitude was applied, and, as for the v5.07, the normalization altitude was determined individually for each scan. For this product, not the Ext_{750}, but r_{med} and N were retrieved assuming fixed σ=1.6, and then obtained values were used to calculate the Ångström exponent and Ext_{750}. Due to a lack of the absolute calibration for the infrared imager, only the albedo at 750 nm was retrieved.

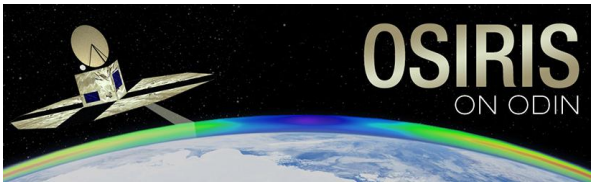

Figure 2.3. Sketch of OSIRIS measurements. Source: `http://www.asc-csa.gc.ca/eng/satellites/odin.asp`

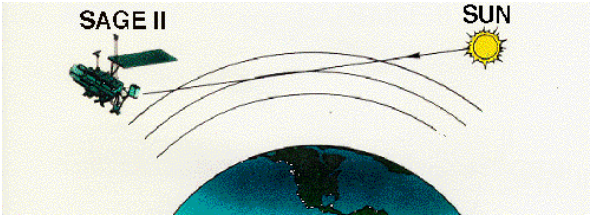

Figure 2.4. Sketch of SAGE II measurements. Source: `https://www.nasa.gov/centers/langley/news/factsheets/SAGE.html`

2.4. SAGE II[1]

Stratospheric Aerosol and Gas Experiment (SAGE) II was a solar occultation instrument on the Earth Radiation Budget Satellite (ERBS), which was launched on 5 October 1984 and operated from late October 1984 until August 2005 in orbit with 57° inclination at about 600 km altitude [Barkstrom and Smith, 1986]. SAGE II was a Sun photometer with seven silicon photodiods with filters at 386, 448, 452, 525, 600, 935 and 1020 nm wavelengths. During each sunrise and sunset encountered by the satellite, the instrument measured solar irradiance attenuated by the Earth's atmosphere between the sun and the instrument. The measurements were provided from the cloud top to about 60 km with the vertical resolution of about 0.5 km. The sketch of SAGE II measurements is presented in Fig. 2.4. The spacial coverage of the measurements was quite sparse, as there were only one sunrise and one sunset event per orbit. Thus, the instrument registered about 15 sunrises and 15 sunsets daily, separated by 24.5° in longitude and slightly in latitude. That results in maximum 30 profiles per day, unlike SCIAMACHY, OMPS or OSIRIS, which provide over 1400 profiles daily. To cover the area between extreme latitudes, it took from 4 to 5 weeks.

In the thesis, the most recent v7.0 of the SAGE II product was used [Damadeo et al., 2013], and similar to OSIRIS data, SAGE II product was used just for the comparison purposes. The SAGE II retrieval algorithm is slightly different than the ones used for the limb instruments. Thus, in the algorithm the profiles of ozone, nitrogen dioxide, water vapor and Ext profiles at 386, 452, 525 and 1020 nm were retrieved simultaneously. For their retrieval, first, the slant-path transmission profiles were calculated at each wavelength, then, using the spectroscopy data slant-path optical depth profiles were obtained for each of the retrieved species. With an "onion-peeling" technique the optical depth profiles were inverted to obtain Ext or trace gases profiles. Later on, based on the Ext at 525 nm and 1020 nm, r_{eff}, as well as surface area density, were obtained [Thomason et al., 2008] assuming a lognormal unimodal PSD.

[1]Main literature source: McCormick [1987].

3

Radiative transfer[1]

As it was mentioned in Sect. 1.4, stratospheric aerosols scatter and/or absorb the radiation, depending on the wavelength region. Usually, radiative transfer models (RTMs) are used to simulate a change in the solar radiation due to those processes. With the RTMs it is possible to simulate the synthetic spectra, as they would be measured by the instrument for the assumed atmospheric parameters. This makes RTMs to be an important part of the retrieval process. The working principle of all RTMs is to solve in some way the radiative transfer equation, which describes all the processes which the radiation undergoes as a result of interaction with a medium based on the energy conservation law. The radiative transfer equation has following general form

$$\frac{dI}{ds} = -k \cdot (I - J), \tag{3.1}$$

where I is the radiance, which is a flux of energy in a given direction in units of energy per area per time per wavelength per steradian. While ds is an infinitesimal path length in the atmosphere, dI is a change in the intensity of the radiation resulting from passing ds interval. The reduction of the intensity is described by the extinction coefficient k, which is a sum of the absorption and scattering coefficients and takes into account both of these processes. The source function, J, describes the increase in intensity due to emission and/or scattering processes.

For any planetary atmosphere the radiation field I can be represented as

$$I = I_{dir} + I_{dif} + I_{emiss}, \tag{3.2}$$

with I_{dir} denoting the direct solar radiation, which has never been scattered in the atmosphere or reflected from the planetary surface. In turn, the diffuse radiation (I_{dif}) has been scattered or reflected at least once. The emission term (I_{emiss}) is negligible in the UV – visible – NIR spectral range, thus, is not considered here.

Since I_{dir} is defined as the radiation, which has not been increased through emission or scattering, the solution of Eq. (3.2) is given by

$$I_{dir}(\Omega) = I_0 \exp\left(-\int_0^s k(\hat{s})d\hat{s}\right), \tag{3.3}$$

[1]Main literature sources: Rozanov [2001], Liou [2002], Gottwald and Bovensmann [2011].

where I_0 is the incident solar flux and Ω is the angle, defining the radiance propagation direction. In terms of the remote sensing, I_{dir} represents the radiance measured by solar occultation instruments.

The radiances measured by the limb scatter instruments correspond to I_{dif}, for which the source function, J, is determined by single and multiple scattering. Thus, the solution of the Eq. (3.1) can be written as

$$\begin{aligned} I_{dif}(\Omega) = \int_0^{s_{LOS}} \frac{1}{4\pi} \Bigg(\int_\Omega \big(\eta_R p_R(\Omega, \Omega') + \eta_a p_a(\Omega, \Omega')\big) I_{dif}(\Omega') d\Omega' + \\ + \big(\eta_R p_R(\Omega, \Omega_0) + \eta_a p_a(\Omega, \Omega_0)\big) I_0 \exp\Big(- \int_0^{s_{Sun}} k(\hat{s}) d\hat{s}\Big) \Bigg) e^{-\tau(s)} ds. \end{aligned} \tag{3.4}$$

Here, s_{LOS} stands for the full path along the line of sight of the instrument, η_R and p_R for the Rayleigh scattering coefficient and the phase function, η_a and p_a for the scattering coefficient and the phase function of the aerosol, Ω_0 for the solar beam propagation direction, s_{Sun} for the full path along the solar beam and τ for the optical depth along the light-of-sight.

To solve the radiative transfer equation 3.1 numerically some coordinate system defining the travelling direction of the radiation should be specified. According to Jones and Bayazitoglu [1992], the choice of this coordinate system is dependent on the medium curvature, the medium and the radiation field symmetry and other conditions. In the RTM SCIATRAN [Rozanov et al., 2014], which was used for the thesis preparation, the radiation field is described in a spherical shell planetary atmosphere using a spherical coordinate system with a center in the center of the planet.

Part II.

Aerosol extinction coefficient

4

Aerosol extinction coefficient retrieval algorithm

4.1. SCIAMACHY[1]

The first part of the thesis deals with an update of the previous version V1.1 of SCIAMACHY *Ext* algorithm. Since the detailed description of the V1.1 retrieval algorithm has been published by other authors [Ernst et al., 2012, Ernst, 2013, von Savigny et al., 2015], in this section, just the distinctive differences to the previous version are presented. The updated version of *Ext* algorithm is denoted V1.4, while intermediate development versions V1.2 and V1.3 were not publicly released and are not considered here.

In their paper, von Savigny et al. [2015] pointed out that the future versions of SCIAMACHY *Ext* retrieval algorithms will include an effective albedo retrieval. An albedo retrieval has not been implemented in V1.1, because of the remaining issues in the absolute calibration of V7 SCIAMACHY level 1 data used there. For V1.4 the version 8 of level 1 data released in 2015 with the updated absolute calibration is used. Another novelty of the V1.4 algorithm is the drop of the shorter wavelength normalization in order to reduce the uncertainties related to measurement noise. Thus, *Ext* is retrieved at 750 nm, using the radiances averaged in ± 2 nm interval. This particular wavelength was chosen, because at the shorter wavelengths measured limb radiances have very low sensitivity to the aerosol particles, and for the longer wavelengths the sensitivity to the aerosol PSD is quite large (more details are provided in Sec. 7.1). This is because limb radiances depend not only on *Ext* but also on the product of the aerosol phase function (p_a) and aerosol scattering coefficient (η_a) (see Eq. (3.4)), which in turn are dependent on the PSD parameters. In certain illumination conditions close to forward or backscattering, this dependency is crucial for the retrieved *Ext* values (a quantitative assessment of the PSD parameters influence on the retrieved *Ext* is presented in Sec. 5.1.3). While the errors for *Ext* at 750 nm are tolerable for these conditions, for the longer wavelengths they are significantly larger. Therefore, the use of the longer and more sensitive to the aerosol PSD wavelengths introduces additional errors in the retrieved *Ext*.

[1] This section was partially published in Rieger et al. [2018].

Taking into consideration the above mentioned changes, the resulting measurement vector is defined by

$$[\mathbf{y}]_h = \frac{\ln \mathbf{I}_h}{\ln \mathbf{I}_{ref}}, \tag{4.1}$$

where h is the tangent altitude, I_h is the radiance measured by the instrument at the altitude h, and I_{ref} is the radiance measured at the reference tangent altitude. For the retrieval, measurements in the tangent altitude range from around 12 to 35 km (the particular altitudes are dependent on the latitude and season) with a reference tangent altitude of about 38 km are used. In comparison to V1.1, the reference tangent altitude is shifted 3 km upwards. The reason for this change is still significant aerosol loading at the previous reference tangent altitude (35 km) [Kremser et al., 2016]. The subtraction of this signal from each retrieved tangent altitude introduces additional errors. In turn, use of the higher tangent altitude as a reference is disadvantageous because of higher stray-light contamination of the radiances. Unlike the previous version, the V1.4 retrieval is performed at the measurement altitude grid (≈3.3 km step versus 1 km step in V1.1), which was shown to cause less oscillations in case there is a cloud within or below the field of view of the instrument. The values below and above the retrieval altitude range are fixed to the a priori. The effective Lambertian albedo of the underlying surface is concurrently retrieved based on the limb radiances measured at the reference tangent height. The measurement vector component related to the albedo is given by

$$[\mathbf{y}]_{alb} = \frac{\ln \mathbf{I}_{ref}}{\ln \mathbf{I}_{sol}}, \tag{4.2}$$

where $\mathbf{I}_{sol}$ is the solar irradiance spectrum, measured by SCIAMACHY daily. The albedo retrieval is implemented to reduce the influence of clouds below the field of view, although clouds within the field of view still remain an issue. To reduce their impact, aerosol extinction coefficient values greater than 0.001 km^{-1} are considered cloud contaminated and filtered after the retrieval is performed.

To solve the inverse problem an iterative regularized inversion approach similar to that described by Rodgers [2000] is used. As it was done by Ernst et al. [2012], it is assumed that the measurement errors are uncorrelated, and the noise covariance matrix is chosen to be diagonal. The signal-to-noise ratio is set to 200 for all tangent heights. This value is used because this is an estimated signal-to-noise ratio of SCIAMACHY radiances measured at the reference tangent altitude. For the a priori covariance matrix, the non-diagonal elements drop off exponentially with a correlation radius of 3.3 km and the diagonal elements correspond to a relative standard deviation of 1. The iterative process stops when the maximum difference between the components of the solution vector at two subsequent iterative steps does not exceed 1%, the relative change in the root mean square of the fit residuals at two subsequent iterations is less than 0.001 or the limit of 30 iterations is reached.

Forward modelling, as well as the retrieval, is done using the RTM with the retrieval code SCIATRAN-3.7 [Rozanov et al., 2014]. Atmospheric pressure and temperature background profiles from European Centre for Medium-Range Weather Forecasts (ECMWF) operational analysis data for the specific date, time and location of each SCIAMACHY limb measurement are used. The scattering phase functions are calculated using Mie

scattering theory [Mie, 1908], assuming spherical sulfate aerosol particles with a unimodal lognormal size distribution (Eq (1.1)). The refractive indices are calculated using the OPAC database [Hess et al., 1998]. The stratospheric aerosol parameters are defined from 12 to 46 km, where the aerosol is assumed to consist of sulfuric droplets with 0% relative humidity in the surrounding atmosphere.

Another significant update is related to the chosen PSD. As it was mentioned in Sec. 2.3, all known *Ext* retrieval algorithms are designed by assuming some PSD parameters. This is because the radiative transfer equation for the limb radiances (Eq. 3.4) can not be solved only with respect to *Ext*, but also p_a and η_a should be determined or assumed. The previous V1.1 algorithm used a PSD with r_{med}=0.11 μm and σ=1.37, which is consistent with in situ observations by Deshler et al. [2003]. Although there is no evidence to prefer either the PSDs used by the other groups or that assumed in V1.1, the use of different distributions would complicate the comparison of limb-scattering retrievals with the OSIRIS instrument. Therefore, the V1.4 SCIAMACHY product uses the same lognormal assumption as the V5.07 OSIRIS product (r_{med}=0.08 μm, σ=1.6). The N profile, however, is not changed with respect to V1.1 and uses the background N values from the Extinction Coefficient for STRatospheric Aerosol (ECSTRA) climatology [Fussen and Bingen, 1999].

While a full validation of the V1.4 is still ongoing (see Sec. 10.2), initial comparisons with V1.1 show smaller uncertainty of the individual retrievals, reduced profile oscillations and better parameterized upwelling radiation (resulting also in less sensitivity to underlying clouds) due to the retrieval of albedo. Since the comparison of the retrieved profiles with other instruments showed good results (Sec. 5.1.2), the V1.4 product is ready to use. It is not only suitable to analyze the climatologies (Sec. 5.1.1) and individual volcanic eruptions (Secs. 9.2 and 9.1), but also is planned to be used in the next version of NASA's Global Space-based Stratospheric Aerosol Climatology (GloSSAC) [Thomason et al., 2018].

4.2. OMPS[1]

SCIAMACHY stopped its operation in 2012, the year when OMPS started to provide data. Currently, there are not many spaceborne limb viewing missions. Except OMPS, OSIRIS continues its operation; however, the mission is rapidly aging. In February 2017 SAGE III/ISS was launched, but the limb level 1 data hasn't been analyzed or calibrated yet. Generally, SCIAMACHY and OMPS measurement geometries are quite similar, which makes the later instrument a good candidate to be SCIAMACHY successor in terms of the stratospheric *Ext* product. However, the merging of both products will be quite challenging, since the overlap period between the instruments is 2 months, so some transfer function should be found, but this is work for the future (see Sect. 10.2).

Since SCIAMACHY and OMPS have similar technical characteristics, the developed *Ext* algorithm V1.0.9 is basically the same as SCIAMACHY V1.4 algorithm. Nevertheless, as

[1]This section was partially published in Arosio et al. [2018].

the instruments are not entirely identical, the algorithm experienced several changes. In this section, just the differences to the algorithm described in Sec. 4.1 will be presented.

In the retrieval, V2.5 of level 1 OMPS data is used. The data is provided with ancillary pressure and temperature profiles, which were taken from the Global Modelling and Assimilation Office (GMAO) interpolated data set. For each wavelength and tangent height the measured radiances, as well as radiances normalized to the solar spectrum, are provided. Unlike SCIAMACHY, OMPS does not provide regular solar measurements, and thus a single solar measurement from the beginning of the mission is used for all the radiances.

The primary challenge in *Ext* retrieval from OMPS comes from its spectral resolution. OMPS was initially designed to obtain ozone products; therefore, it has a good resolution in the UV part of the spectrum, but not in the visible or NIR part. Since the wavelengths below 500 nm are not sensitive to aerosol, they can not be used for the retrieval. For the wavelengths longer than 500 nm the OMPS spectral resolution grows exponentially from about 7 nm at 500 nm up to about 30 nm at 1000 nm. For that reason, the choice of the measurement wavelengths, which are not affected by any other absorbing species, is quite limited. The wavelength, used in SCIAMACHY and OSIRIS retrieval (750 nm), is not suitable since it is affected by the O_2-A absorption band. The official NASA *Ext* product uses measurements at 675 nm, however the spectral resolution for this wavelength is about 14 nm, which makes it affected by O_3 and O_2-B absorption bands. The retrieval of the aerosol parameters from these wavelengths can be done only if the amount of the absorbers are known very accurately, which is technically hard to arrange for each scan. Thus, for the IUP OMPS *Ext* product, it was decided to take measurements at 869 nm wavelength. The interval from about 830 nm to 900 nm is absorption free, and OMPS spectral resolution for this wavelength is 22 nm, which makes it suitable for *Ext* retrieval. It should also be noted, that for now just the measurements from the central slit are taken into consideration. This is because level 1 data from left and right slits are still experiencing issues with stray-light and pointing. As it was done in the SCIAMACHY V1.4 retrieval algorithm, the effective Lambertian albedo is concurrently retrieved at the measurement wavelength. During the work with SCIAMACHY *Ext* database, it has been noticed, that the cloud filter threshold used in there is too low. For that reason, for OMPS this threshold was increased, and the values higher than 0.002 km^{-1} are considered cloud contaminated.

The changes in the measurement wavelength have resulted in some adjustments of the retrieval settings. Thus, for OMPS the retrieval is done from 10.5 to 33.5 km, with the measurement at 34.5 km being used as the referent spectrum. The reference tangent altitude is lowered in comparison to SCIAMACHY to avoid the stray-light contamination at the higher altitudes. The choice of that particular tangent altitude is a trade-off between the amount of stray-light and aerosol signal in the radiances. The retrieval is done at the regular grid with 1 km step, which is the same as the measurement grid provided in OMPS level 1 data. In accordance, the correlation radius is set to 1 km. Furthermore, the *Ext* at that particular wavelength contains vertical oscillations related to the remaining calibration issues. To smooth spurious oscillations, the first-order Tikhonov regularization was employed with the parameter value of 50. Based on the provided by NASA information, the signal-to-noise ratio for all the tangent altitudes was set to 500.

It should be noted, that OMPS V1.0.9 algorithm is preliminary, some improvements and validation have to be done to make it an accurate product (see Sec. 10.2). However, the retrieved Ext profiles can be used to study the climatologies (Sec. 5.2) and variations related to volcanic eruptions, e.g. Kelut, and biomass burning events, e.g. Canadian Wildfires (Ch. 9). The retrieved Ext is also used in IUP OMPS O_3 retrieval.

5

Aerosol extinction coefficient datasets and their validation

5.1. SCIAMACHY

5.1.1. Global database

The improved *Ext* retrieval algorithm V1.4 was applied to the whole SCIAMACHY dataset. In this section, IUP SCIAMACHY monthly mean stratospheric *Ext* profiles at the regular altitude grid with 3.3 km step on the regular geographical coordinates with 5° in latitude and 15° in longitude steps are taken into consideration. These *Ext* profiles create a global product covering almost a 10 year period from September 2002 until April 2012.

The behavior of *Ext* with time and altitude is depicted in Fig. 5.1 in 20° latitude bins. In each latitude bin major volcanic eruptions, relevant for this region, are shown with the vertical dashed lines. The eruptions which occurred within ±35° latitude from the bin center are considered to be relevant. The data about the strength and exact time of volcanic eruptions is taken from the database of Smithsonian Institution [2017] and Bingen et al. [2017].

For all latitude bins, some general patterns are observed, e.g, significant increase of *Ext* after volcanic eruptions. Usually, for the relevant volcanic eruptions, the perturbation reaches the altitude of 21 km (e.g. Nabro, Kasatochi, Sarychev). A usual perturbation from an eruption lasts about a year, which agrees with the results reported previously for the eruptions of the comparable strength [e.g. Kremser et al., 2016]. However, it is hard to track directly the duration of perturbation periods, because since 2004 the volcanic eruptions with the Volcanic Explosivity Index (VEI) 3-5 occurred regularly, and there is no way to distinguish between the influences of the single eruptions. The eruptions of Ruang and Reventador (VEI 4) are also unrepresentative. During these eruptions only insignificant amounts of SO_2 were released; therefore, the amount of the formed aerosol was not large, and the perturbations did not last long.

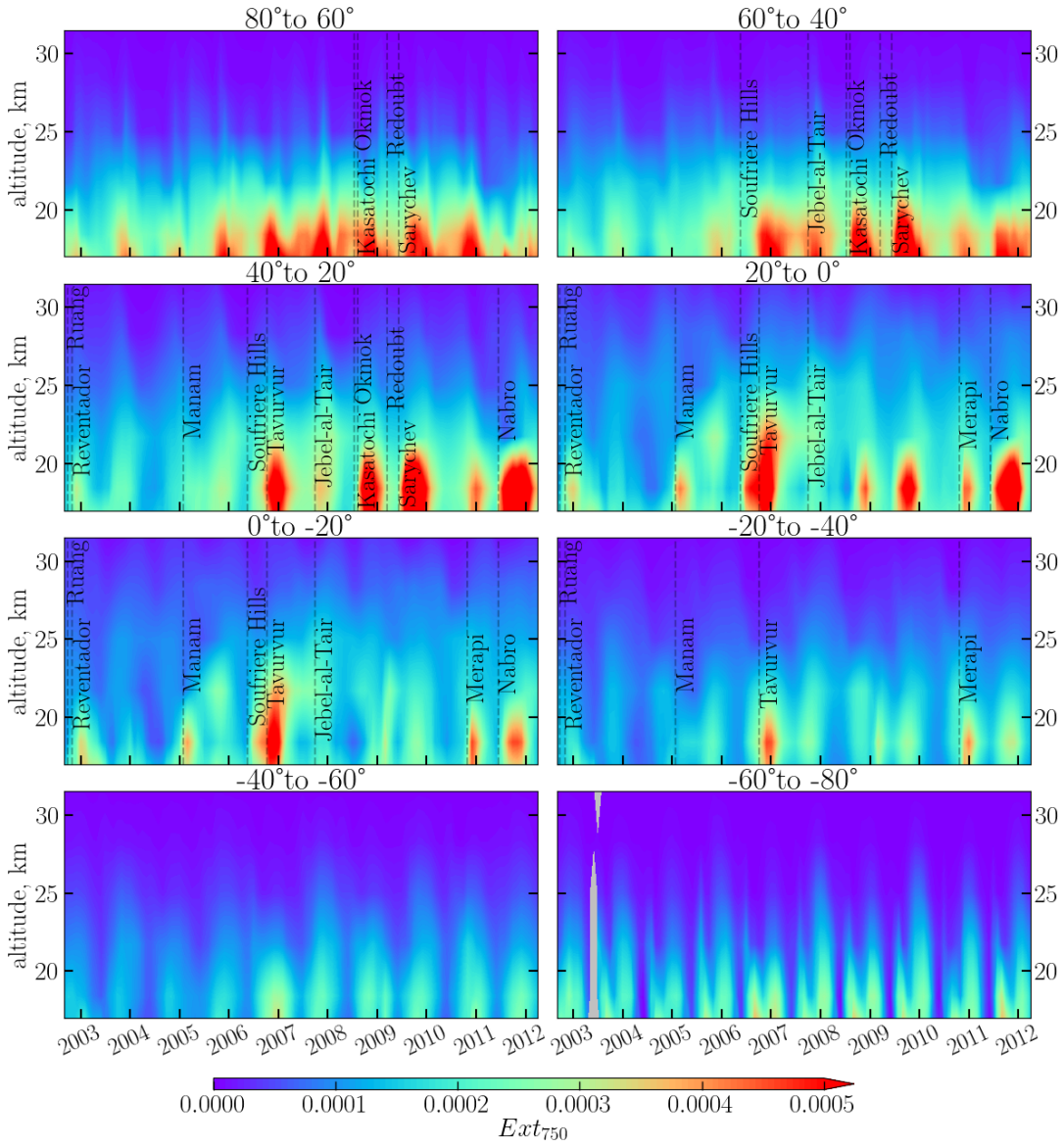

Figure 5.1. Zonal monthly mean Ext_{750} from SCIAMACHY V1.4 data.

Analyzing the V1.1 SCIAMACHY *Ext* data, Brinkhoff et al. [2015] reported the signatures of the QBO at altitudes above 28 km. For the current version these signatures are also noticeable. They are mostly well pronounced in the tropics and mid-latitudes. In the 40° to 20° latitude bin, there is an increase in *Ext* in 2003, 2005, 2007, 2009 and 2011 at the altitudes above 25 km. In the bin from 20° to 0°, the increase is noticeable in the same years at the altitudes above 28 km. For the Southern Hemisphere, the increase is shifted by about a year. This agrees with the results presented in Brinkhoff et al. [2015]. Generally, multiple authors reported QBO signatures in stratospheric aerosol parameters (see Sec. 1.3). It should be also noted, that in the latitude bins above 40° in both hemispheres the seasonal pattern is dominating. Although the seasonality of stratospheric aerosols was reported in e.g. Hitchman et al. [1994], Bingen et al. [2004], for the instruments working in limb viewing geometry the seasonality of *Ext* is also related to the seasonality of SSA and high sensitivity to PSD parameters. The later problem is discussed in the details in

Sec. 5.1.3.

Another important feature is so-called tape-recorder effect, which means that the perturbation from the volcano reached higher altitudes with some time lag. This effect is well pronounced after tropical Manam and Tavurvur eruptions in all latitude bins; however, is not evident after other eruptions (even after the comparably large tropical Nabro eruption). There might be multiple explanations of this distribution. Most likely, it is related to intensive upward motions in the tropics, related to BDC. However, the mispronounced tape-recorder might also be caused by the sub-optimal binning and averaging: the monthly mean values are not the best choice for the volcanic plume studies. Additionally, some outliers might be related to the sub-optimal cloud filtering threshold. To look at the volcanic plumes in details, it was decided to analyze 10-days average profiles for the period of Manam, Tavurvur and Sarychev eruptions. These particular events were chosen to analyze the tropical eruptions with the pronounced tape-recorder (Manam and Tavurvur) and the extra-tropical eruption with one of the highest VEI, but without obvious tape-recorder (Sarychev). These case studies are discussed in Sec. 9.1 and 9.2 respectively.

5.1.2. Comparison with SAGE II and OSIRIS [1]

In order to validate the SCIAMACHY V1.4 *Ext* product, the results were compared to the *Ext* products from other spaceborne instruments, SAGE II and OSIRIS. As mentioned in the previous chapters, SAGE II provided one of the longest continuous records of stratospheric aerosols. As SAGE II is an occultation instrument, its *Ext* retrieval is insensitive to many of the assumptions required in the limb scatter retrievals, making the dataset robust and independent. The comparison of *Ext* with the OSIRIS *Ext* product is beneficial, because both instruments employ limb scattering technique; however, they use different algorithms and RTMs to retrieve the products (Sec. 2.3).

To test agreement between the three instruments the comparison is performed for the triple coincidences, i.e. when all instruments have collocated measurements. Measurements are used when SAGE II and OSIRIS observations are within ±5° latitude, ±20° longitude and ±24 h of the SCIAMACHY tangent point. As all measurements have approximately 200 km path lengths through the atmosphere, and scanning of a vertical profile typically occurs over a few degrees latitude, tightening these criteria does not generally improve agreement. Use of the coincident profiles from SCIAMACHY, OSIRIS and SAGE II simultaneously ensures the comparison between the instruments to be independent from the different amount of collocations for different instruments. The differences are studied in the 20° latitude bins to distinguish better biases related to latitude and solar geometry conditions. Therefore, in case the double coincidences would be considered (separate collocations for SCIAMACHY –SAGE II and SCIAMACHY – OSIRIS), the comparison of the different number of profiles in the same latitude bin for the different instruments would lead to the statistical uncertainties. Although the use of the triple collocation limits the overall number of collocations, it still provides a reasonable and statistically

[1] This section was partially published in Rieger et al. [2018].

significant amount of profiles for each latitude bin. Thus, the chosen collocation criteria result globally in 2272 coincident measurements for each instrument between 2002 and 2005, when all three instruments were operating. In individual latitude bins, the amount of collocated profiles varies from 153 to 570.

While both, OSIRIS and SCIAMACHY, *Ext* products are provided at 750 nm, the SAGE II data were interpolated to this wavelength using the Ångström exponent derived from the 525 and 1020 nm channels. Although this is not a perfect conversion, as the wavelength dependence is not strictly linear in log-wavelength log-extinction space, the error is generally limited to less than 10% for most particle sizes [Rieger et al., 2015]. To minimize the impact of clouds in the analysis, aerosol extinction coefficient values greater than 0.001 km^{-1} are excluded for all three instruments (SCIAMACHY cloud filtering criteria, see Sec. 4.1). Due to the relatively eruption-free period of this comparison, this has minimal effect on the comparisons removing approximately 3% of the values. The results of the comparisons in the form of the median relative differences are shown in Fig. 5.2.

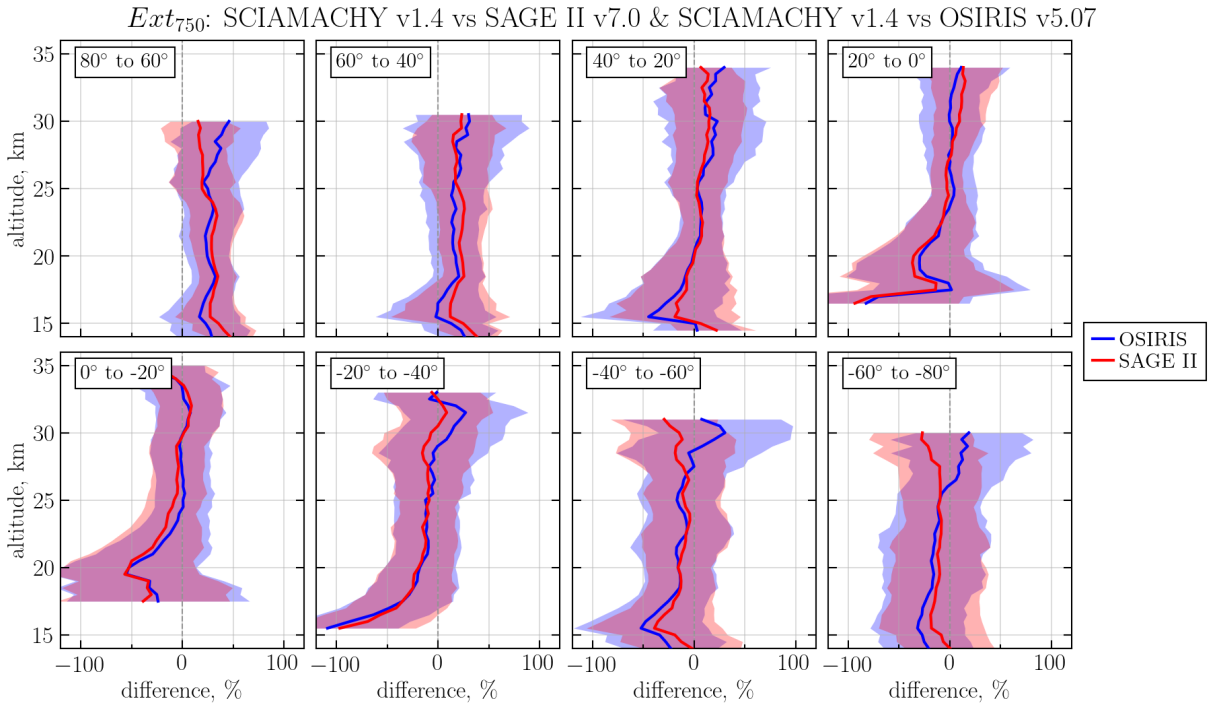

Figure 5.2. Median relative difference in Ext_{750} between SCIAMACHY and SAGE II (red line) and SCIAMACHY and OSIRIS (blue line) (SCIAMACHY-instrument)×200/ (SCIAMACHY+instrument). The shaded area shows ±1 standard deviation.

In general, SCIAMACHY V1.4 *Ext* product agrees with SAGE II and OSIRIS within approximately 20% for most regions. Exceptions to this are at high latitudes in the Northern Hemisphere. In the latitude bin from 80° to 60° SCIAMACHY *Ext* is higher than SAGE II *Ext* by up to 30% at 25 km, the differences to OSIRIS reach 50% at 30 km. In the high latitudes of the Southern Hemisphere (latitude bin -60° to -80°) *Ext* values from SCIAMACHY are lower than the ones from SAGE II by about 30%, while the difference to OSIRIS is about 10%. Although most clouds have been removed, SCIAMACHY and OSIRIS *Ext* profiles are still likely to be cloud contaminated near

and below the tropopause. Therefore the differences and their standard deviations at the lowermost retrieved altitudes up to about 17 km at the latitudes higher than 20° in both hemispheres are larger than at the higher altitudes. In the tropical region (within 20° from the equator), the altitudes up to about 21 km can be cloud contaminated.

Several factors contribute to the differences between the Ext retrieved from SCIAMACHY, OSIRIS and SAGE II. The extensive analysis of these factors was published in Rieger et al. [2018] in the framework of a SCIAMACHY – OSIRIS validation study. Since it was a joint work, here just the conclusions from that study are summarized. Thus, the primary causes of the observed differences are the choice of a priori profiles in both limb instrument retrievals, which influence the high-altitude normalization. A wrong assumption contributes up to 20% error in the retrieved Ext profile. Another important source of errors is an incorrect assumption of the aerosol PSD parameters, which leads to up to 100% errors in the forward and backscattering viewing conditions. This is the dominating factor in the differences with SAGE II in the high latitudes of both hemispheres. The more detailed analysis is presented in Sec. 5.1.3. The differences with OSIRIS have different nature, because the PSD assumption for both instruments is the same. Most of the differences here are coming from the different geometries (SSAs), RTMs, retrieval methods and as mentioned earlier a priori assumptions (also related to N) at the referent tangent height.

5.1.3. Sensitivity of the algorithm to the PSD parameters [1]

Comparing SCIAMACHY Ext V1.4 product to SAGE II and OSIRIS (Sec. 5.1.2), it was noted, that the significant differences at high latitudes are the result of the fixed PSD. Usually, it influences Ext in two ways. First and most important, wrongly assumed PSD leads to the wrong assumption of p_a and η_a in the RTM (see Sec. 4.1 and Ch. 3). Second, the assumed PSD parameters are the part of the wrong assumption of a priori profile at the referent tangent altitude. This is because the a priori profile is parametrized according to Mie theory through r_{med}, σ and N (see Eq. (1.5)).

To illustrate the influence of the different aerosol PSD assumptions, Ext was obtained using the V1.4 algorithm with the changed r_{med} and σ parameters. The Ext was retrieved simultaneously at two wavelengths, λ_1=750 nm and λ_2=1090 nm with three PSD parametrizations. In order to quantify how the different assumptions change the retrieved Ext, the results are compared to the SAGE II instrument. As mentioned before, SAGE II was an occultation instrument, which means that its Ext retrieval is independent from PSD assumption. SAGE II does not provide Ext at 750 nm; therefore it was recalculated using the Ångström exponent, which introduces some error in the resulting Ext_{750}. Additionally, Ext_{1090} was retrieved from SCIAMACHY measurements and then with Ånsgröm exponent, calculated from the assumed PSD, converted to Ext_{1020} provided by SAGE II. In case the PSD is assumed in the right way, this conversion is supposed to be more accurate, because the Ångström exponent obtained from PSD can be calculated for any

[1] This section was partially published in Rieger et al. [2018].

wavelength pair without an assumption of its spectral homogeneity. To make the comparison independent from clouds, as in Sec. 5.1.2 the Ext_{750} values greater than 0.001 km^{-1} and the coincident Ext_{1020} were excluded from the comparison.

As it was noticed above, PSD assumption plays the most important role at high latitudes. Therefore, median relative differences are calculated and analyzed in the latitude bins from 80° to 60° in both hemispheres, and in the tropical region (20° to -20°). The results are presented in Fig. 5.3 for Ext_{750} (upper panels) and for Ext_{1020} (lower panels). The line colors show the different PSD assumptions. The blue line shows the results with the PSD assumption used in V1.4 and OSIRIS algorithms (r_{med}=0.08 μm, σ=1.6), the red line shows the PSD assumption from the V1.1 SCIAMACHY Ext retrieval algorithm (r_{med}=0.11 μm, σ=1.37) and the green line shows the PSD assumption, which was used for OMPS V0.5 retrieval algorithm [DeLand et al., 2016] with r_{med}=0.06 μm and σ=1.8.

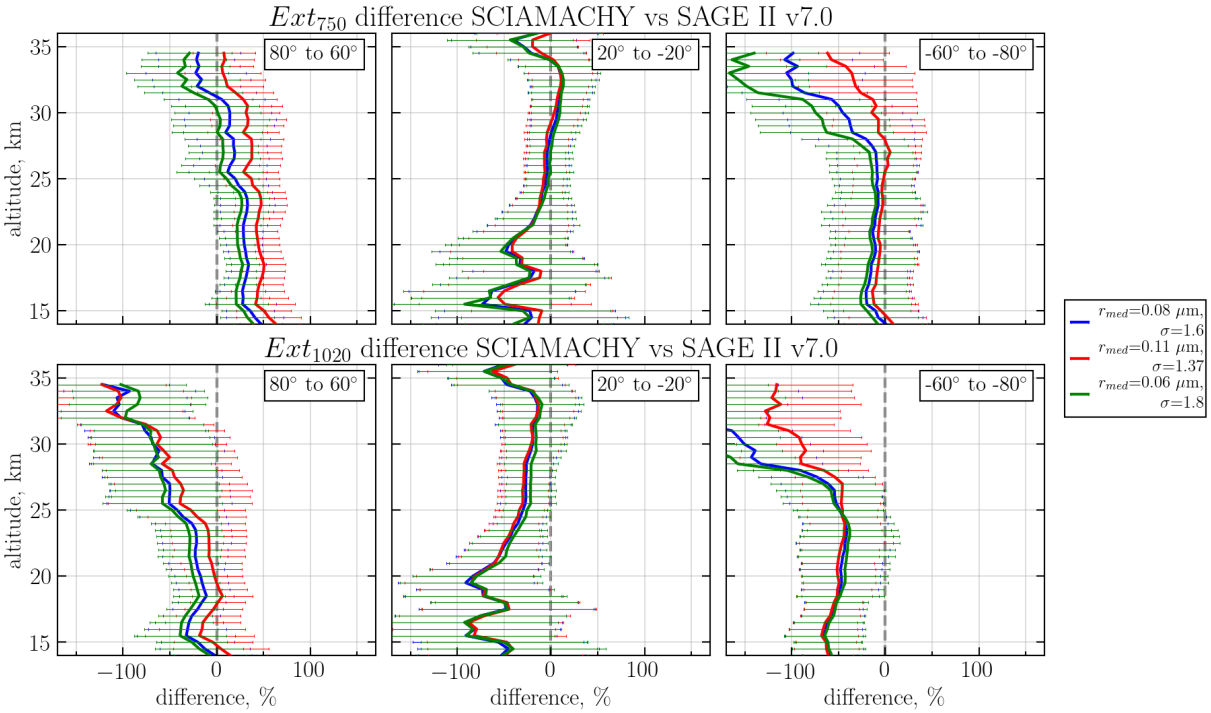

Figure 5.3. Median relative difference in Ext_{750} (upper row) and Ext_{1020} (lower row) between SAGE II and SCIAMACHY (SCIAMACHY-SAGE II)×200/ (SCIAMACHY+SAGE II). SCIAMACHY Ext was retrieved with three different PSD parameters (see legend). The horizontal bars show ±1 standard deviation.

As expected, the most distinctive differences in the retrieved Ext are seen at high latitudes. For Ext_{750} the difference with SAGE II increases in the latitude bin 80° – 60° at 30 km from 0% for the assumption with r_{med}=0.06 μm and σ=1.8 to 35% for SCIAMACHY V1.1 assumption. For the whole altitude range, there is about 35% offset between the relative SCIAMACHY–SAGE II differences for those two assumptions. For the high latitudes of the Southern hemisphere (-60° to -80°) the differences in the retrieved Ext are minor for the altitudes below 25 km. However, they start to increase above, reaching at 34 km differences of -70% for the SCIAMACHY V1.1 PSD assumption and -150% for r_{med}=0.06 μm and σ=1.8. For the tropical region, PSD assumption does not seem to play a significant role, since the retrieved Ext profiles overlap each other.

Qualitatively Ext_{1020} relative differences are quite similar to those from Ext_{750}, but they differ in absolute values. For the tropical region, the changes in PSD do not affect the relative differences to SAGE II. For the high latitudes of the Northern Hemisphere, the differences have an offset of about 25-35% between SCIAMACHY V1.1 and OMPS V0.5 assumptions. The relative differences to SAGE II are around 0% from 14 to 24 km and decrease to -100% at 34 km for SCIAMACHY V1.1 PSD. As for Ext_{750}, for the high latitudes of the Southern Hemisphere (-60° to -80°), the differences are independent from the PSD parameters up to about 24 km. Here, SCIAMACHY Ext is about 50% lower than the one from SAGE II. However, for 34 km the differences increase to 110% for SCIAMACHY V1.1 assumption and to about 200% for the OMPS V0.5 assumption.

The changes in the retrieved Ext resulting from the different PSD assumptions are quite remarkable. Varying the assumption within theoretically possible background values [Deshler, 2008], the retrieved Ext at high latitudes changes by at least 30%. Another noticeable feature is the change of the absolute values of the differences with respect to SAGE II depending on the wavelength, which means that the assumption on the Ångtröm exponent for the conversion is wrong. While conversion of SAGE II Ext profiles with $\alpha_{525/1020}$ to Ext_{750} results in less than 10% error, it still accounts for the natural variability of the Ångsröm exponent. Meanwhile, the differences between SCIAMACHY and SAGE II at the same altitude and for the same PSD assumption are varying from 20 to 70% for Ext_{750} and Ext_{1020}. This means that the bulk of the error comes from SCIAMACHY Ext_{1090} profiles and their further conversion to Ext_{1020}, which is done with the fixed and most likely wrong Ångström exponent. These problems make the retrieval of PSD parameters very desirable. First, the correct PSD parametrization will drastically improve the Ext retrieval at high latitudes, and second, it will make the conversion of the Exts and comparison with the other instruments less uncertain.

5.2. OMPS: global database

As it was mentioned in Sec. 4.2, the current retrieval algorithm still needs improvements and lacks validation; however, the general behavior of Ext still can be analyzed. As for SCIAMACHY V1.4, after cloud filtering, OMPS V1.0.9 profiles were monthly averaged and put onto the regular geographical grid with 2.5° latitude and 5° longitude step. For OMPS the geographical grid is finer, because the instrument spatial resolution is finer than that of SCIAMACHY. The changes of Ext_{869} with time and altitude are presented in Fig. 5.4 in 20° latitude bins. OMPS is still in operation, and the data is processed on a regular basis; though, in the Fig. 5.4 it is presented until July 2018.

In comparison to the SCIAMACHY operational period, all significant volcanic eruptions occurred at the beginning of OMPS working time. Since 2015 there were no larger volcanic eruptions; however, in summer 2017 there was a major biomass burning event in British Columbia, Canada. Since the increase in Ext was registered by multiple instruments even at 21 km, and the influence of the fires was observed even far away from the source [e.g. Khaykin et al., 2018], it was decided to depict that event along with the volcanic eruptions

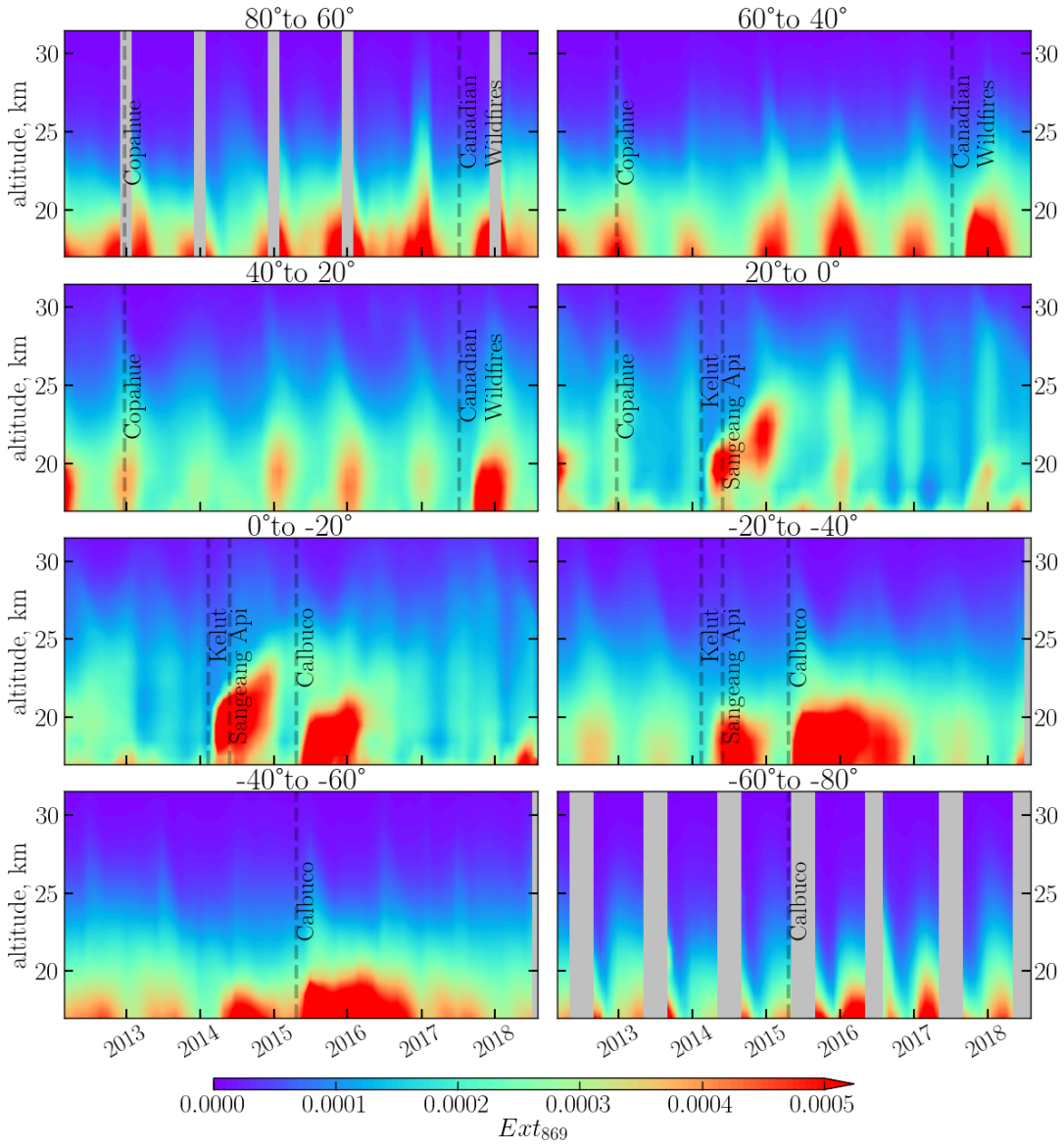

Figure 5.4. Zonal monthly mean Ext_{869} from OMPS V1.0.9 data.

with the dashed lines. In Fig. 5.4 the volcanic eruptions are presented in each latitude bin, in case the eruption happened within ±35° latitude from the center of the bin.

Analyzing Fig. 5.4, it is interesting is to notice an increase of *Ext* right after the start of the instrument operation. Most distinctively this enhancement is seen in the latitude bins between 40° and -40°. This is a tail of the cataclysmic Nabro eruption in the middle of 2011 (see Sec. 5.1.1). In the tropical region (from 20° to -20°) the tape-recorder effect from that eruption is quite obvious. A tape-recorder effect in the tropics is also seen after the Kelut eruption. The Kelut eruption is remarkable, because it caused the aerosol layer perturbation, which reached the altitudes over 25 km. In general, this eruption seems to be similar to the eruption of Tavurvur in 2006. Another important event is the eruption of Calbuco in Chile in 2015. This cataclysmic eruption (VEI 4), is proved to cause a record-size ozone depletion event in October 2015 [Ivy et al., 2017]. The increase

of the *Ext* after this eruption seems to last for about two years in the mid-latitudes of the Southern Hemisphere (see bins from -20° to -40°and from -40° to -60° in Fig. 5.4). The tape-recorder effect after this eruption is well pronounced only in the latitude bin from 0° to -20°.

Similar to SCIAMACHY product, the QBO signatures are visible for the tropical region and mid-latitudes; however, the seasonality of the stratospheric aerosol even at this latitudes plays a significant role. Another important feature is the significant seasonal increase in *Ext* in both hemispheres at the latitudes higher than 40°. This increase is most likely to be a retrieval artifact, related to looser cloud threshold compared to SCIAMACHY. As a consequence, the larger amount of cloud contaminated profiles, profiles with PSCs and profiles with measurement noise influence the monthly means.

It should be noted at that point, that neither SCIAMACHY nor OMPS cloud filtering thresholds are optimal. If SCIAMACHY cloud filtering criterion is applied, some events with the increased *Ext*, e.g. volcanic plumes, are filtered along with the clouds. In case OMPS criterion is applied, the remaining clouds, PSCs and noisy profiles are contaminating the results, mostly the high latitudes (see Fig. 5.4). The intermediate thresholds have the same disadvantages. For stratospheric *Ext* products distinguishing between the clouds and volcanic plumes is crucial; thus, it would be beneficial to use some other mechanism to distinguish between them. Liebing [2016] developed a new cloud filter for SCIAMACHY data, based on the statistical approach. However, this cloud flag was developed after the work on *Ext* products and has not been used to filter clouds from both instruments. Though, it is planned to be done in the future (see Sec. 10.2).

To analyze the behavior of aerosol extinction coefficient from OMPS and to understand if it is different than the one from SCIAMACHY, the volcanic eruption of Kelut, as well as the plume from the Canadian Wildfires of 2017, were considered. To make the analysis consistent with SCIAMACHY, the 10-days averaged profiles are analyzed in Sec. 9.4.

Part III.

Aerosol particle size distribution

6

Aerosol PSD retrieval algorithm[1]

In this section the newly developed aerosol particle size distribution (PSD) retrieval algorithm is presented. As it was noticed in the motivation and Sec. 5.1.3, the information about PSD is highly relevant for limb instruments. The algorithm presented here was developed for SCIAMACHY limb measurements, but it can be potentially used for any other limb viewing instruments with similar technical characteristics.

Unlike the algorithms aimed to retrieve aerosol PSD parameters from the occultation measurements [e.g. Bingen et al., 2004, Thomason et al., 2008], the algorithm described below does not include *Ext* retrieval as an intermediate step. Instead, the measured limb radiances at seven wavelengths are directly employed to obtain the PSD parameters. The wavelengths are chosen outside the intervals near the spectral channel boundaries to avoid artifacts of the optical system. In order to reduce the measurement noise the sun-normalized radiances were averaged in the following intervals λ_1=750±2 nm, λ_2=807±2 nm, λ_3=870±2 nm, λ_4=1090±2 nm, λ_5=1235±20 nm, λ_6=1300±6 nm, λ_7=1530±30 nm. The wavelengths below 750 nm were not considered because of a lower sensitivity to aerosols, and those above 1530 nm were rejected because of an insufficient signal-to-noise ratio. The intervals were chosen to avoid absorption signatures of other atmospheric constituents, minimizing uncertainties caused by incorrect absorber profiles knowledge. Limb radiances are normalized by the measured solar irradiance spectrum ($\mathbf{I}_{sol}$).

To illustrate the selected spectral information, the chosen central wavelengths are depicted in Fig. 6.1 with vertical blue lines and the averaging intervals are shown with blue shaded areas. The difference between the logarithms of the radiance without and with absorption by gaseous species (optical depth) for SCIAMACHY limb measurements at 21.3 km is shown with the red line. The grey shaded area shows the spectral channel boundary region.

Both forward modelling and the retrieval are performed with the software package SCIATRAN-3.8 [Rozanov et al., 2014]. The retrieval approach employs an iterative regularized inversion technique similar to that described by Rodgers [2000] to solve the inverse

[1]This chapter was partially published in Malinina et al. [2018b].

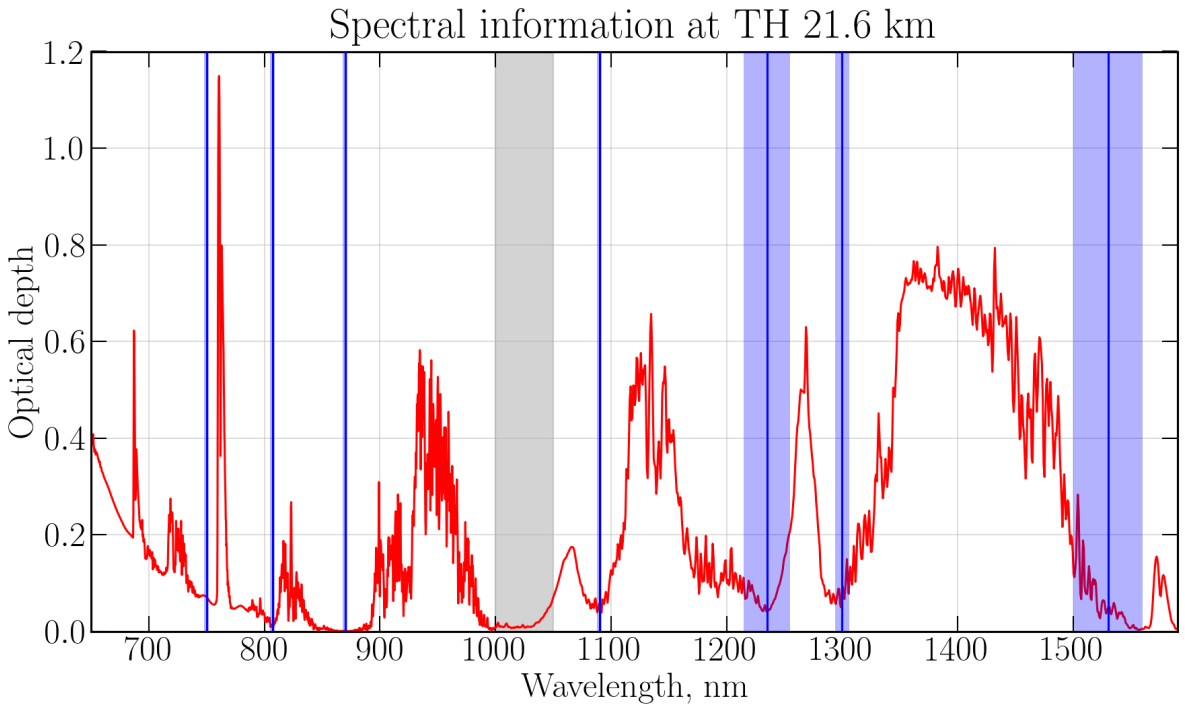

Figure 6.1. Difference between the logarithms of the radiance without and with absorption by gaseous species (optical depth) for SCIAMACHY limb measurements at 21.3 km. Blue shaded areas show selected wavelengths intervals for SCIAMACHY PSD retrieval algorithm, with the solid lines showing the central wavelengths. The grey shaded area shows spectral channel boundaries.

problem. In this approach the inversion of the linearized radiative transfer equation is required, which is formulated as:

$$\mathbf{y} - \mathbf{y_0} = \mathbf{K}\ \hat{\mathbf{x}} + \epsilon, \tag{6.1}$$

where $\mathbf{y}$ is the measurement vector, whose components $[\mathbf{y}]_m = \ln(\frac{\mathbf{I}_{meas}(\lambda_j,h_k)}{\mathbf{I}_{sol}(\lambda_j)})$ are the logarithms of the normalized limb radiances at all selected wavelengths (λ) and tangent heights (h). Here, index m is defined as $m = (k-1)N_\lambda + j$, where N_λ is the total number of wavelengths, k runs over selected h and j runs over selected λ. Components of the vector $\mathbf{y}_0$ are given by $[\mathbf{y}_0]_m = \ln(\frac{\mathbf{I}_{mod}(\lambda_j,h_k)}{\mathbf{I}_{sol}(\lambda_j)})$, where $\mathbf{I}_{mod}(\lambda_j, h_k)$ are modelled limb spectra at wavelength λ_j and tangent height h_k. State vector $\hat{\mathbf{x}}$ contains relative deviations of the retrieved atmospheric parameters, $\mathbf{x}$, from their initial values, $\mathbf{x}_0$, e.g. $[\hat{\mathbf{x}}]_i = \frac{[\mathbf{x}]_i - [\mathbf{x}_0]_i}{[\mathbf{x}_0]_i}$ is the i-th component of the vector $\hat{\mathbf{x}}$. $[\mathbf{K}]_{m,i} = \frac{\partial [\mathbf{y}]_m}{\partial [\mathbf{x}]_i}\Big|_{\mathbf{x}=\mathbf{x}_0}$ defines components of the weighting function matrix (Jacobian matrix). All kinds of errors are denoted by ϵ. The solution of the linear inverse problem given by Eq. (6.1) can be found according to Rodgers [2000] as

$$\hat{\mathbf{x}} = (\mathbf{K}^T {\mathbf{S_y}}^{-1}\mathbf{K} + {\mathbf{S_a}}^{-1})^{-1}\mathbf{K}^T {\mathbf{S_y}}^{-1}(\mathbf{y} - \mathbf{y}_0), \tag{6.2}$$

where, $\mathbf{S_a}$ represents the a priori covariance matrix, and $\mathbf{S_y}$ is the noise covariance matrix.

Taking into consideration the non-linearity of the inverse problem, an iterative approach is implemented. It is decided not to follow the maximum a posteriori probability (MAP) approach suggested by Rodgers [2000]. As the inverse problem is strongly non-linear,

Table 6.1. Example of the signal-to-noise estimation for the measurement on 02.03.2007 at 8.67° N.

wavelength	Tangent altitude					
	18.67 km	21.76 km	25.04 km	28.34 km	31.62 km	34.88 km
750 nm	3600	5000	3130	2600	2200	1000
807 nm	2600	2250	2640	1650	1500	630
870 nm	3560	4050	3100	1870	925	560
1090 nm	660	620	920	600	160	230
1235 nm	1150	1100	800	500	160	100
1300 nm	250	580	580	440	240	130
1530 nm	820	900	640	430	180	140

the use of a reasonable a priori covariance in the MAP approach results in a diverging solution, while the a priori variance which results in a stable solution strongly constrains it to the initial guess. To overcome this issue the weighted regularized inversion with the zeroth-order Tikhonov regularization is used in this study. Thereby, the weight of the a priori information is decreased by replacing the initial state vector $\mathbf{x}_0$ at each iterative step by the state vector obtained at the previous iteration, $\mathbf{x}_n$. The variance of $\mathbf{x}_n$ is set to 1%. This parameter is selected empirically to achieve a trade-off between the retrieval stability and sensitivity. Thus the solution at the (n+1) step is given by

$$\tilde{\mathbf{x}} = (\mathbf{K_n}^T \mathbf{S_y}^{-1} \mathbf{K_n} + \mathbf{S_a}^{-1})^{-1} \mathbf{K_n}^T \mathbf{S_y}^{-1} (\mathbf{y} - \mathbf{y}_n), \tag{6.3}$$

where $[\tilde{\mathbf{x}}]_i = \frac{[\mathbf{x}_{n+1}]_i - [\mathbf{x}_n]_i}{[\mathbf{x}_n]_i}$.

The iterative process stops when the maximum difference between the components of the solution vector at two subsequent iterative steps does not exceed 1%, the relative change in the root mean square of the fit residuals at two subsequent iterations is less than 0.001 or the limit of 100 iterations is reached. Since a strict constraint is put to deviations from the a priori vector, there are typically 20-30 iterations needed for the retrieval process to converge.

The noise covariance matrix is assumed to be diagonal, i.e. the errors are spectrally uncorrelated. Signal-to-noise ratio is estimated for each scan from SCIAMACHY measurements and varies from 65 to 5000 depending on the wavelength and tangent height. An example for one of the measurements is presented in Tab. 6.1. For each of the PSD parameters, the diagonal elements of the a priori covariance matrix are set empirically to 0.01, and the non-diagonal elements drop off exponentially with a correlation radius of 3.3 km, while the elements describing the correlation between different parameters are chosen to be zero.

So far, only the retrieval of R_{mod} and σ is performed, and from these parameters w is calculated using Eq. (1.3). The N profile is selected in accordance with the ECSTRA model climatology for background aerosol loading conditions [Fussen and Bingen, 1999]. N is assumed to decrease exponentially from 15.2 cm^{-3} at 18 km to 0.5 cm^{-3} at 35 km, and remains unchanged during the whole retrieval process. This is justified by a low sensitivity of the retrieval to this parameter (see Sec. 7.1 for details). The initial guess parameter values are arbitrarily chosen as R_{mod}=0.11 μm and σ=1.37. Scattering phase functions

as well as extinction and scattering coefficients per particle are calculated using the Mie scattering theory. Aerosol parameters are defined from 12 to 46 km, where the particles are assumed to be sulfate droplets (75% H_2SO_4 and 25% H_2O) with 0% relative humidity in the surrounding atmosphere. Below 12 km and above 46 km the aerosol number density is set to zero. The refractive indices are taken from the Optical Properties of Aerosols and Clouds (OPAC) database [Hess et al., 1998]. Although the chosen representation of the aerosol composition might be inadequate below the tropopause and/or above 35 km, it enables to avoid jumps and unreasonable values at the lowermost and the uppermost retrieval altitudes and does not affect significantly the results in the retrieval sensitivity region (18-32 km, see Sec. 7.1 for details).

The retrieval is performed for the tropical zone (from 20°S to 20°N) in the altitude range from about 18 km up to about 35 km (the actual altitudes depend on the latitude and season). The choice of the altitude range is justified by lower sensitivity below 18 km [Rieger et al., 2018] and higher biases due to stray light above 35 km. To minimize the need for constraints and to avoid additional errors, e.g. related to altitude interpolation, the measurement altitude grid is used for the retrieval. The exact levels of the measurement grid depend on time and latitude, but usually the grid ranges from about 0 km to 100 km with 3.3 km step. Outside the retrieval range, for the altitudes lower than the minimum retrieval height down to 12 km, the initial guess profile scaled relative to the result at the lowermost retrieved altitude is used; while for the altitudes above the upper limit up to 46 km no additional constrains are set. The focus of the initial study lays in the tropics because the transport mechanisms here are less complicated which makes the interpretation of the obtained results more straightforward. To extend the retrieval to the extra-tropical latitude bands, issues related to the scattering angles close to backward and forward scattering as well as large solar zenith angles need to be dealt with.

To reduce the sensitivity of the retrieval to the reflection properties of the underlying surface, effective spectral Lambertian albedo is concurrently retrieved based on the limb radiances at the same tangent heights where the aerosol particle size retrieval is performed. As it will be shown further, at 35 km aerosol influence on the limb radiances is rather small, thus the information from this tangent altitude contributes mainly to the albedo retrieval, while other tangent altitudes are employed for the stability reason. The initial albedo guess is 0.5 for all wavelengths. As for the particle size parameters, albedo for different wavelengths is uncorrelated with the other parameters and with the albedo at the other wavelengths. Clouds below and within the field of view remain an issue, even with the albedo retrieval. Therefore, only completely cloud free profiles (from 0 km) are used for now. Here, instead of the standard SCODA cloud filtering algorithm [Eichmann et al., 2016], a cloud filtering algorithm based on a statistical approach is used [Liebing, 2016]. The algorithm designed by Liebing [2016] is more preferable for use in aerosol retrievals, because the Eichmann et al. [2016] approach has the disadvantage of flagging the pixels with high aerosol loading (i.e. after the volcanic eruptions) as cloudy.

Atmospheric pressure and temperature background profiles are taken from ECMWF operational analysis data for the specific date, time and location of each SCIAMACHY limb measurement.

7

Sensitivity studies

7.1. SCIAMACHY limb-scatter sensitivity to the PSD parameters [1]

In this section the sensitivity of the limb radiances to the aerosol PSD parameters is analyzed in two ways. The first analysis is done by performing simulations with the RTM SCIATRAN. For this study the model is run for an observational geometry typical for the tropical region in the middle of July (a solar zenith angle of 41°and solar azimuth angle of 141°). The extraterrestrial solar flux measured by SCIAMACHY for the chosen day is used. In the RTM, multiple scattering is taken into account and the albedo is set to 0 (representation of the ocean surface).

To understand the sensitivity of the retrieval to the different PSD parameters, three sets of limb radiance simulations are performed. For each set, one of the PSD parameters is varied, while the other two parameters are fixed. The modelled intensities for these simulation sets are presented in Fig. 7.1 at the tangent height of 25 km. As the results at other tangent heights show similar behaviour, the sensitivity only at this arbitrarily chosen geometry is analyzed. Natural logarithms of the simulated sun-normalized intensities for different values of the selected parameter (this representation corresponds to the way, how intensities are treated by the retrieval algorithm) are shown as lines. The shaded areas represent the amplitude of the intensity variations resulting from variations of the other two parameters. In this study the following simulation sets are performed: the first set employs a fixed σ=1.37 and the same number density profile as used in the retrieval, while the mode radius varies from 0.05 to 0.15 μm (Fig. 7.1 A). Another set of conditions (Fig. 7.1 B) is simulated by changing σ from 1.1 to 2.0 with the fixed R_{mod}=0.08 μm and the same number density as in previous simulation set. This results in the variation of w from 0.008 to 0.13 μm. The last set of simulations (Fig. 7.1 C) is made by scaling the whole number density profile by factors ranging from 1 to 2, with the fixed R_{mod}=0.08 μm and σ=1.37. The parameter set with standard non-scaled particle particle number density (N) profile with R_{mod}=0.08 μm and σ=1.37 is chosen as a reference, as this set of parameters

[1] This section was partially published in Malinina et al. [2018b].

is considered to be typical for a background (free of volcanic perturbations) atmosphere. It should be noted, that this investigation is aimed to analyze a relative sensitivity of the observed limb radiance to the variations in different parameters and, thus, its results are not influenced much by their absolute values. Nevertheless, the considered amplitude of the parameter variations is in qualitative agreement with the reported variations of R_{mod}, σ and N in the stratosphere [Deshler et al., 2003].

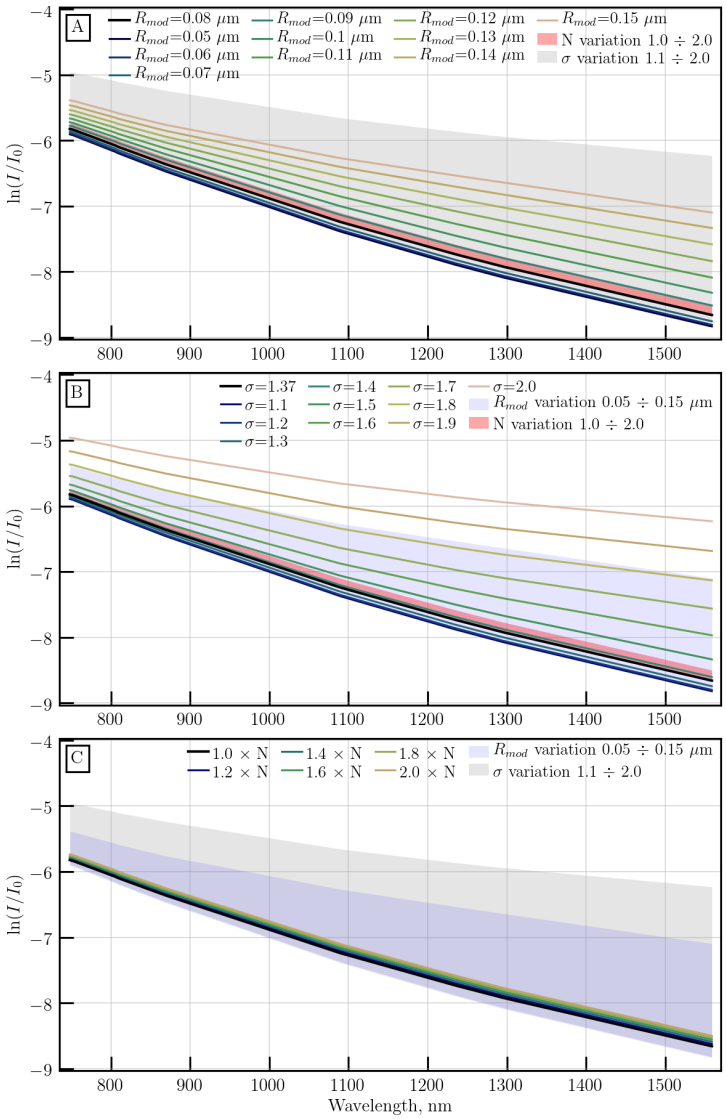

Figure 7.1. Logarithms of sun-normalized intensities spectra at a tangent height of 25 km, modelled with different PSD parameters. Black line represents the "standard" background conditions.

Analyzing Fig. 7.1 it is evident that variations of the limb radiance due to variations of the particle particle number density (N) are remarkably smaller than those due to variations of R_{mod} or σ (or w). The variation of N profile by a factor of 2 (or 200%) results in a similar response in the limb radiance as the variation of R_{mod} by 0.01 μm ($\approx$ 13%) or variation of σ by 0.13 ($\approx$ 10%). This effect can be explained as follows: in a rough approximation the scattered solar radiation observed by a limb-viewing instrument (I_{dif}) is proportional to the product of aerosol phase function (p_a) and aerosol scattering coefficient (η_a). I_{dif} also depends on the aerosol extinction cross-section (β_{aer}) and N (see Ch. 3). Both, the

product of p_a and η_a and β_{aer}, depend on R_{mod} and σ. As the dependency of p_a, η_a and β_{aer} on R_{mod} and σ is highly non-linear, these parameters contribute to the radiance stronger than N. The weaker dependence is also illustrated by much smaller weighting functions for N, than those for R_{mod} or σ. The weighting functions (R_{mod}, σ and N) for each retrieved altitude are shown in Fig. 7.2. As the weighting functions (see Sec. 6) show the variations in the observed signal due to changes in the considered parameter, much smaller weighting functions of N (Fig. 7.2, right panel) mean much smaller contribution due to variations of the parameter in the measured signal. As a consequence, the variations in N are neglected in the retrieval, and the altitudinal behaviour in the N profile is considered to be constant with the time.

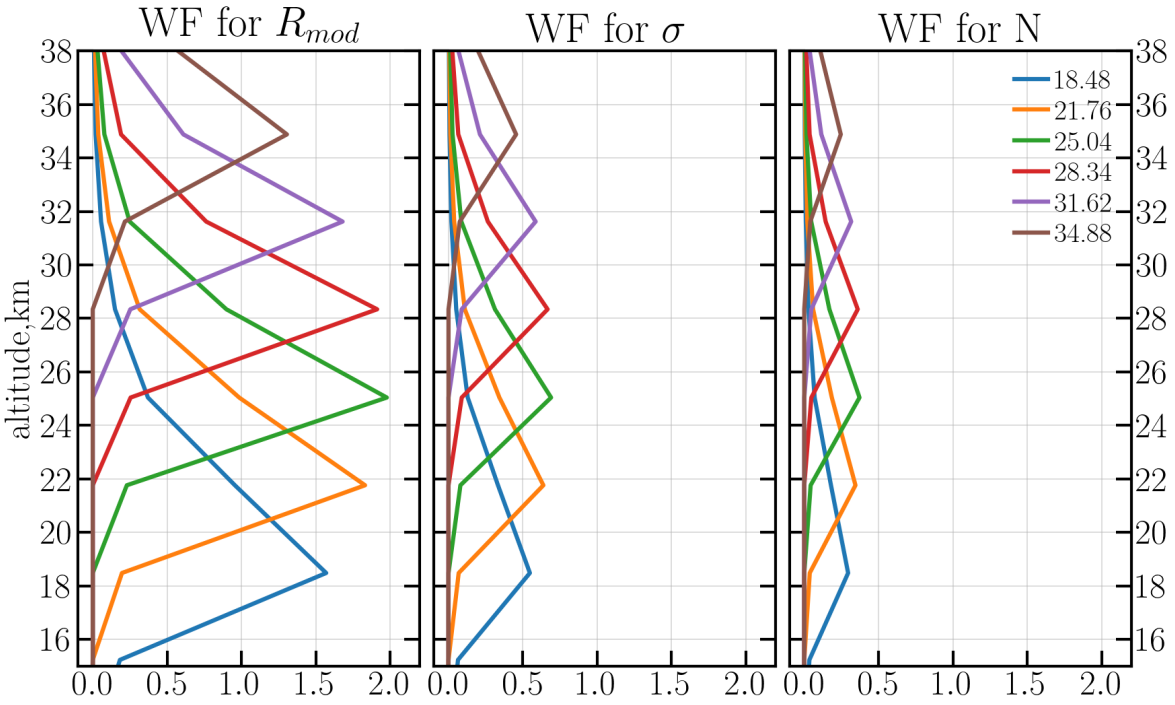

Figure 7.2. Relative logarithmic weighting functions at λ_7=1530 nm in the retrieval height range for R_{mod} (left), σ (middle) and N (right). Color coded are the different tangent heights.

It is worth emphasizing again, that the particle number density profile used in the above described retrieval is derived from the ECSTRA climatology for background aerosol loading conditions (see Ch. 6). Even though the uncertainty for the volcanic active periods increases, for the background period the errors are rather small because the used profile is expected to be close to the reality. The magnitude of the errors in the retrieved R_{mod}, σ and w due to unknown N is discussed in the Secs. 7.3.1 and 7.3.2.

Another analysis is performed through characterization of the retrieval algorithms sensitivity by averaging kernels, which are commonly used for this purpose. In general, this characteristic is specific to the measurement setup, algorithm implementation, and retrieval parameters settings. Averaging kernels for the limb scatter spaceborne instruments in the relevant altitude region are distinctly peaked at the tangent altitudes, where a bulk of information is originating from. Their shape characterizes the vertical sensitivity and resolution of the measurement-retrieval system and provides information on the contribution of the a priori information to the retrieved profiles.

In Fig. 7.3 averaging kernels for both R_{mod} (left panel) and σ (right panel) are presented for typical tropical observation conditions. Since variations in the observational geometry (viewing angle and solar zenith angle) in the tropics are rather small, only one specific example for typical illumination and background conditions is presented here. At all altitudes in the retrieval range (in this case 18.5-34.9 km), except for the uppermost one, averaging kernels for both parameters have pronounced peaks at the measurement tangent altitudes indicating that no significant smearing of the results in the vertical domain has occurred and optimal sensitivity of the retrieval is achieved for each tangent altitude. At the uppermost altitude (34.9 km) averaging kernels are clearly broader and the peak is much less distinct in comparison to the other altitudes. Such shape of the averaging kernels at this altitude is evidence of a strong influence of the neighboring altitude levels and partial loss of sensitivity.

As pointed out above, in the performed retrieval the relative deviations from the solution obtained at the previous iterative step are determined. The state vector variance is set to 1% of the parameter values resulting from the previous iteration. For this reason such widely used characteristics as the averaging kernel peak value, a posteriori covariance and measurement response are meaningful only within one iterative step but not applicable to the full iterative process.

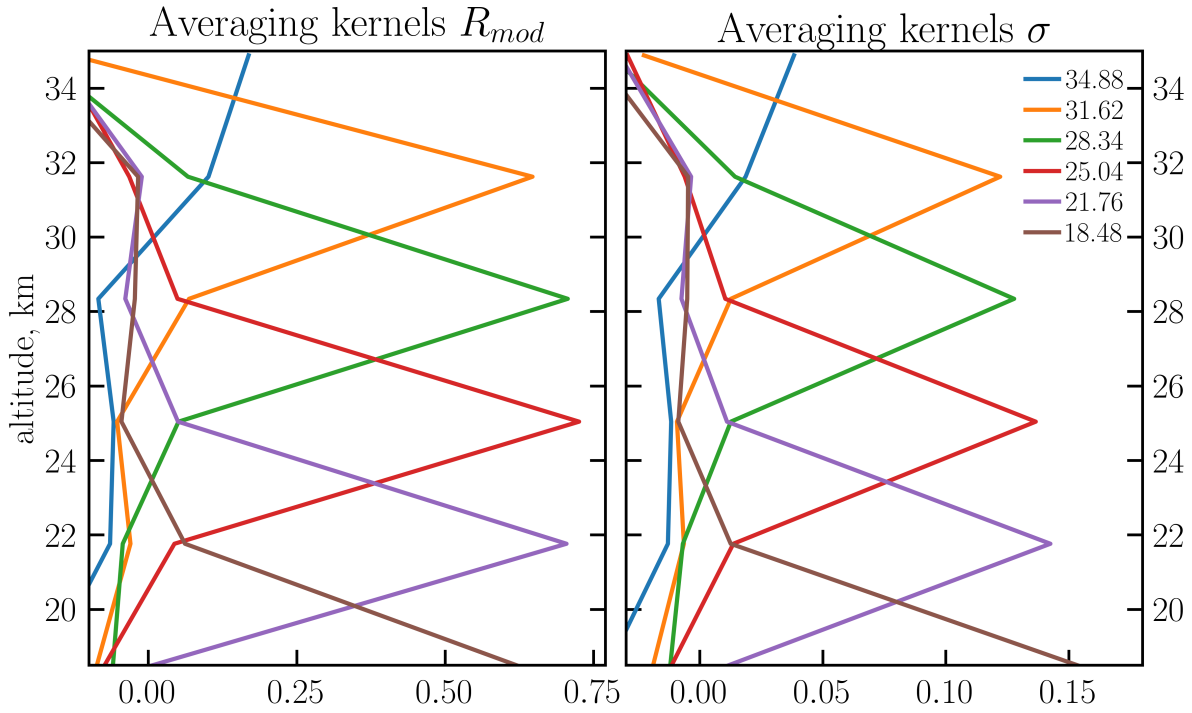

Figure 7.3. Averaging kernels for the aerosol particle size distribution parameters: R_{mod} (left) and σ (right). Results were obtained using the spectra modelled with perturbation of all three parameters. Color coded are the different tangent heights.

7.2. Difference in the sensitivity of the limb-scatter and occultation measurements to the PSD parameters[1]

In the previous section sensitivity of SCIAMACHY limb-scatter measurements to PSD was discussed. The sensitivity of the occultation measurements to the PSD parameters is somewhat different. As mentioned before, occultation and limb scatter instruments employ different measurement approaches, resulting in different sensitivity to the aerosol parameters in general. Here, when discussing occultation measurements, the measurements done by solar occultation instruments are assumed. Such instruments register the solar radiation transmitted through the atmosphere during sunrise and sunset events as seen from the satellite.

Here, the sensitivity to both, PSD parameters and Ext is considered. Comparing Eqs. (3.3) and (3.4) the one can see, that it is quite straightforward to derive k from I_{dir}. In the wavelength intervals without any other absorber features k represents a sum of the aerosol extinction coefficient and Rayleigh scattering coefficient, i.e. $Ext + \eta_R$. In contrast, to obtain I_{dif} using Eq. 3.4 an iterative approach is needed. Furthermore, I_{dif} depends on the product of p_a and η_a. In turn, both, p_a and η_a are determined by the aerosol PSD parameters. Thus, in most of the Ext retrieval algorithms which rely on limb measurements an assumption on the PSD parameters is used, and those are kept fixed during the retrieval process (see Ch. 4). In addition, p_a is a function of the scattering angle. The issue related to the dependency of the limb radiances on the SSA is well known, and was discussed by Ernst [2013], Rieger et al. [2014, 2018], Loughman et al. [2018] and highlighted in Chs. 4 and 5.

To understand how the differences in the measurement techniques influence the instrument sensitivity to aerosols, extended analysis is provided below. In some previous studies [e.g Twomey, 1977, Thomason and Poole, 1993, Rieger et al., 2014] the analysis of the so-called kernels was used to determine the contribution of the particles of different sizes to the observed radiance. According to Twomey [1977] the measured intensity of the scattered light can be presented as:

$$I(\lambda) = \int_0^\infty K(\lambda, r) n(r) dr, \tag{7.1}$$

where r is a radius of the particle and K is a kernel. For the measurements of the transmitted light the following equation is appropriate [Twomey, 1977]:

$$\ln(I(\lambda)/I_0(\lambda)) = \int_0^\infty K(\lambda, r) n(r) dr. \tag{7.2}$$

Whereas for the measurements of scattered solar light K does not have an analytic representation, for the occultation measurements it is given by $r^2 Q_e(r/\lambda)$, where Q_e is the Mie extinction efficiency. Besides, the right sides of the Eqs. (7.1) and (7.2) have the same form, although they refer to different left sides. Indeed, for the scattered light measurements the left side is represented by $I(\lambda)$, while for the transmission the left side is $\ln(I(\lambda)/I_0(\lambda))$, which according to the Eq. (3.3) is $\tau = -\int_0^s k(\hat{s}) d\hat{s}$. Thomason and Poole

[1] This section was partially published in Malinina et al. [2018a].

[1993] derived K for the extinction measurements and showed it for SAGE II. In their research K had units of m^{-1}, since they were assessing it per unit volume of air. For the limb measurements, K was derived for the single-scatter radiance by Rieger et al. [2014], and the resulting K was dimensionless. It should be also noted, that for their study Rieger et al. [2014] preferred to calculate K for OSIRIS numerically, stating, that the derived formula contains too many approximations. Thus, K can be used in the assessment of the sensitivity of instruments employing the same measurement technique but not for the comparisons between the instruments measuring in different geometries. As one objective of this study is the comparison of the sensitivities of the limb and occultation measurements to the particles of the different sizes, it is not reasonable to follow the approach of Twomey [1977]. Instead, the dimensionless sensitivity of the measured radiance, S, to the aerosol particles of a certain size is defined as a relative change in the intensity of the observed radiation with respect to the aerosol free conditions. Thus, S is represented by:

$$S(\lambda, r_i) = \frac{I(\lambda) - I_R(\lambda)}{I_R(\lambda)}. \tag{7.3}$$

Here, $I(\lambda)$ is the radiance including both, Rayleigh and aerosol signal, and I_R is the Rayleigh signal. When S=0, the radiance has no contribution from the aerosol extinction or scattering. With increasing S increases the aerosol contribution to the measured radiance.

A quantitative assessment of S is made by modelling the intensities with the radiative transfer model SCIATRAN for limb measurements (on the example of SCIAMACHY limb geometries) and for occultation measurements. The intensities are modelled for the distributions with R_{mod} varying from 0.04 to 0.30 μm with the step (Δr) of 0.01 μm. For each distribution, σ has been chosen such that w is equal to 0.01 μm (this corresponds to the chosen Δr). N is considered to be the same for all simulations.

For the above described simulations S at λ=750 nm and λ=1530 nm are presented in Fig. 7.4 for occultation (dashed black line) and for limb measurements (colored solid lines). As limb radiances depend on SSA, the simulations are done for three different observational geometries: SSA=60°(blue line), SSA=79°(green line) and for SSA=138°(red line). The angles from 60 to 140° represent the SSA range for SCIAMACHY measurements in the tropical region. The grey shaded area shows $S < 0.01$. This empirical value represents a typical uncertainty of the measurement-retrieval system, caused by the uncertainties in the radiative transfer modelling. A justification for this threshold is provided further in this section.

As it is seen from Fig. 7.4, S for limb radiances at both wavelengths are obviously higher than those for the occultation measurements. Moreover, for all SSAs the limb curves enter the shaded grey area at around 0.06 μm, while the occultation curves enter it at about 0.11 μm at λ=750 nm and at 0.20 μm at λ=1530 nm. These results agree with those presented by Thomason and Poole [1993] for SAGE II measurements, and illustrate the well-known statement that the occultation measurements are insensitive to the particles with the radii smaller than 0.1 μm [see e.g. Thomason et al., 2008, Kremser et al., 2016]. Better sensitivity to the smaller particles observed for the limb measurements is explained by the fact that the aerosol PSD contributes in very different ways into the

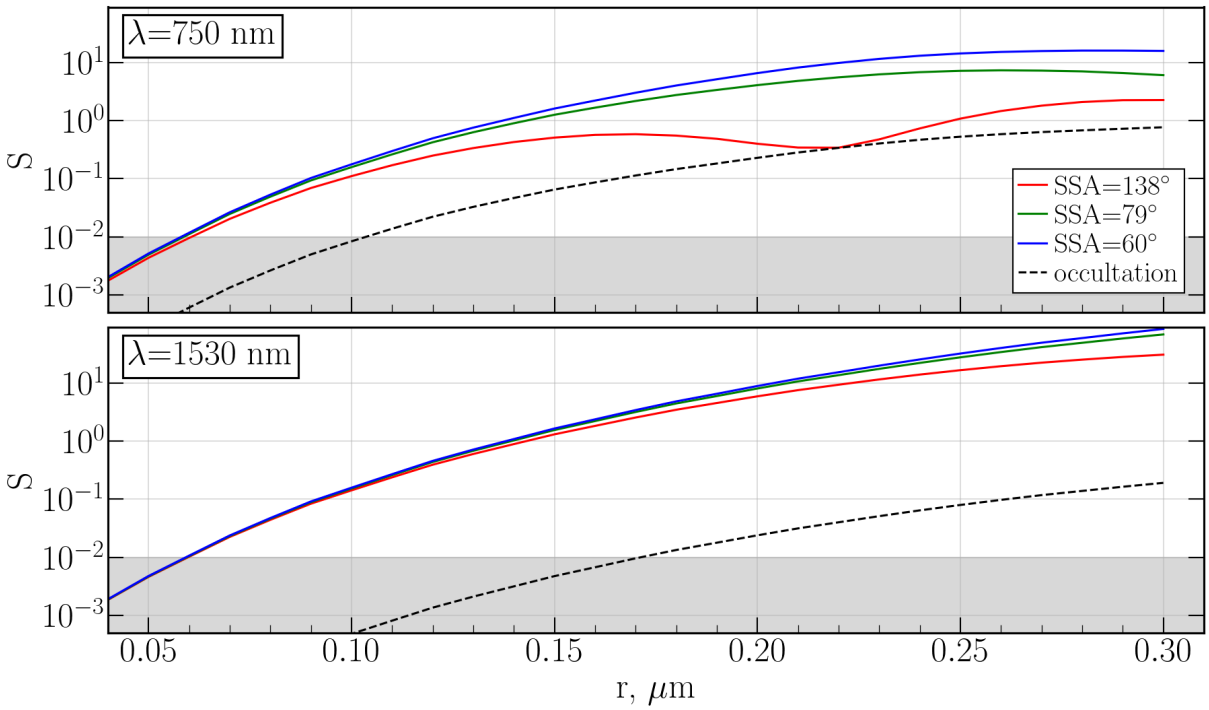

Figure 7.4. Simulated sensitivity, S, at 21.7 km for range of particles with radius r. The simulations were performed for different limb geometries with different solar scattering angles (SSAs) and for one occultation geometry.

observed radiances for limb and occultation measurements. While I_{dir} depends inverse exponentially on k (or Ext), I_{dif} is, to a first order, proportional to the product of p_a and η_a. As both, p_a and η_a, depend on the PSD parameters, limb radiances tend to be more sensitive to aerosol particles of the smaller size, and as a consequence are expected to provide more accurate PSD parameters during the "background" aerosol loading conditions.

To justify the choice of the sensitivity threshold, an example of the relative differences in the the modelled radiance due to changes in different factors for both, limb (SSA=138°) and occultation, geometries assuming randomly picked PSD with R_{mod}=0.08 μm and σ=1.6 is provided. These relative differences at 21.7 km for different wavelengths are presented in Fig. 7.5, with the results for limb geometry depicted in panel A and for occultation geometry in panel B. For each simulation the whole profile of one of the following parameters was increased by 10%: temperature (magenta dots), atmospheric pressure (green dots) and ozone concentration (cyan dots). For simplicity reasons, it was chosen to perturb the whole profile, rather than values at the particular altitudes. Changes in ozone concentration by 10% are reasonable as they reflect the remaining uncertainties in the ozone profiles retrieved from the spaceborne measurements across the relevant altitude range [Tegtmeier et al., 2013]. Additionally, in Fig. 7.5 the blue dots show the changes in the radiances with the assumption that the concentration of the aerosol particles with $r \leq$0.06 μm is equal to zero (cutoff at 0.06 μm) and with the red dots show the cutoff at 0.10 μm (particles with $r \leq$0.10 μm were not considered). Figure 7.5 shows, that for the limb geometry the relative changes in the radiance due to changes in temperature, pressure or ozone concentration are within 0.8% in the considered wavelength interval. For the

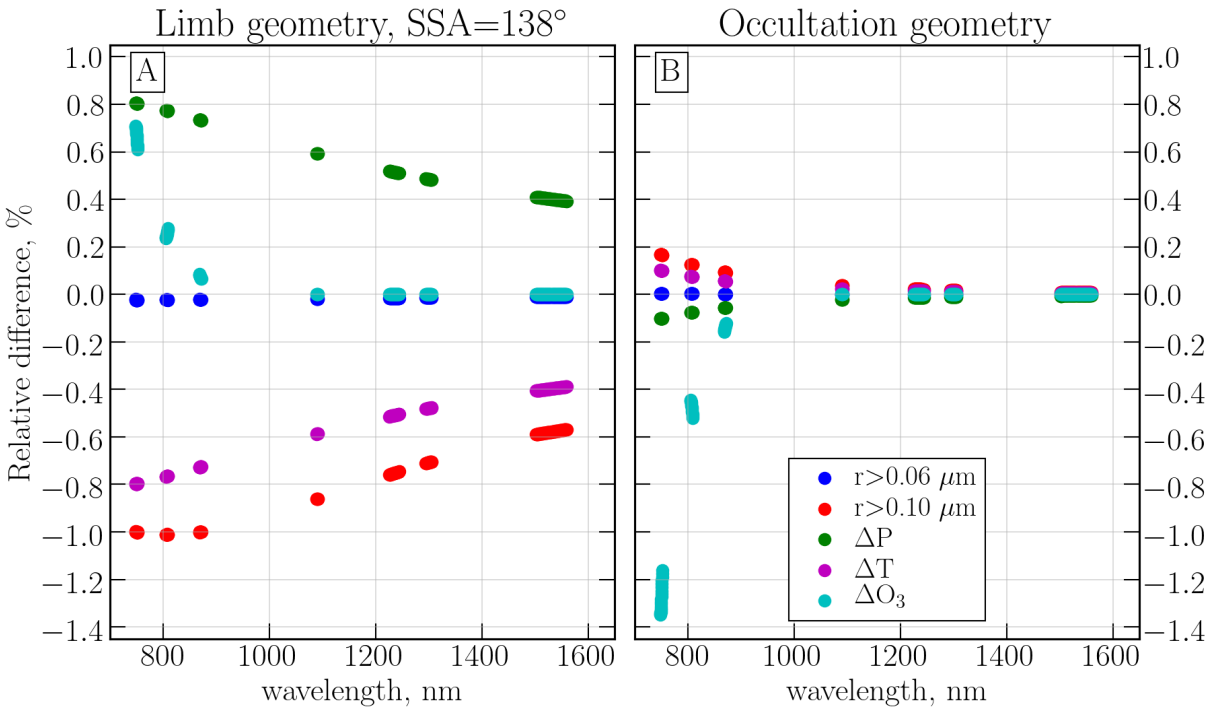

Figure 7.5. Relative changes in the radiance at 21.7 km for limb (panel A) and occultation (panel B) geometry. The responses in radiance due to 10% changes in temperature, atmospheric pressure and ozone concentration are presented by magenta, green and cyan dots, respectively. The cutoff in PSD at 0.06 μm is depicted with blue dots, and the cutoff at 0.10 μm is presented with red dots.

PSD cutoff at 0.06 μm the changes are about 0.03%, however, for the cutoff at 0.10 μm the changes are slightly larger than 1% for the wavelength interval shorter than 1000 nm, reducing to 0.6% at the longer wavelengths. For the occultation geometry the changes are somewhat different. Namely, the changes in pressure or temperature are comparable with the changes in the PSD cutoff, but the changes in ozone concentration contribute up to 1.4% in the radiance at 750 nm. Such behaviour of relative changes in the intensities shows that in the considered wavelength interval 1% provides a realistic estimation of the uncertainties from the radiative transfer modelling for both geometries, even though this uncertainty results from different factors. For limb geometry, the changes due to PSD cutoff at r=0.06 μm are within this threshold, however, with the cutoff at r=0.10 μm the relative difference in the radiances exceeds it, and thus this change is considered as detectable. For the occultation measurements, both PSD cutoffs result in smaller changes than those coming from the radiative transfer modelling uncertainty.

7.3. Error estimation

In this section the errors resulting from fixed particle number density profile in the aerosol PSD retrieval are discussed. The assessment is done for both, the retrieved parameters (R_{mod} and σ) and the parameters which are recalculated from them (w, Ext and Ångström exponent).

The assessment of the retrieval performance presented here is done by simulating the limb radiance using perturbed values for the retrieved parameters and then performing the retrieval using synthetic data. For all retrieval runs the same settings as in the nominal retrieval process are used. Ideally, the retrieved values are expected to be the same as those used to simulate the radiances. To test the retrieval under different conditions, five scenarios were used. All scenarios are simulated for one observation geometry (viewing and solar zenith angles) typical for SCIAMACHY limb measurements in the tropical region. A detailed information on the selected scenarios is presented in the Tab. 7.1. Generally, the scenarios can be divided into three types depending on the perturbation of the particle size parameters. The first type includes "small", "background" and "volcanic" scenarios. The intensities for these scenarios are modelled using R_{mod} and σ as listed in Tab. 7.1 with the same N, as assumed in the retrieval algorithm, i.e. only R_{mod} and σ are perturbed. The second type is represented by "volcanic (2N)" scenario, which is modelled with the same R_{mod} and σ as the "volcanic scenario", but the N profile is multiplied by a factor of 2 between 12 and 23 km. The perturbation in the N profile is performed only in the lower layers because significant changes in the aerosol loading due to volcanic eruptions during the SCIAMACHY life time were shown to reach maximum altitude of about 23 km (see von Savigny et al. [2015] and Sec. 5.1.1). The third type is represented by the "unperturbed" scenario. For this scenario intensities are simulated with R_{mod}=0.11 μm, σ=1.37 and the N profile assumed in the retrieval, i.e. with the same parameter values as used to initialize the retrieval algorithm. All these values with slight adjustments are taken from [Deshler, 2008] and are expected to be close to the reality. As there is no reliable information on the altitudinal behaviour of R_{mod} and σ, the values for these parameters are kept constant with the height. In all the scenarios modelled surface albedo is assumed to be 0.15 at all wavelengths. Gaussian noise is added to all simulated limb radiances based on the signal-to-noise ratios estimated from SCIAMACHY measurements. To ensure a reliable statistics 100 independent noise sequences are generated.

7.3.1. Retrieved parameters [1]

It is most important to evaluate, how the fixed N influences the retrieved parameters. Therefore, the retrieved profiles of R_{mod} (panel A) and their relative errors (panel B) for the above discussed scenarios are presented in Fig. 7.6. For σ, retrieved profiles and relative errors are plotted in Fig. 7.7. Solid lines in the panels A of Figs. 7.6 and 7.7 refer to the median retrieved profiles for the scenario, and dashed lines represent true modelled conditions. In the panels B of Figs. 7.6 and 7.7 solid lines show relative median errors of the retrieved profiles with respect to the true value. In both figures, shaded areas show ± 1 standard deviation from the median value.

Analysis of Figs. 7.6 and 7.7 shows, that the retrieval results using "unperturbed" profiles (brown lines) of R_{mod} and σ as well as the results for profiles with the perturbed R_{mod} and σ (cyan, blue and green lines) are very close to the true values. The relative error is within 20% for R_{mod} and within 5% for σ. Maximum absolute ($\epsilon = |retrieved - true|$) and relative errors for all scenarios and parameters are summarized in Tab. 7.1. It is worth

[1] This section was partially published in Malinina et al. [2018b].

mentioning that the maximum deviation for the scenarios with unperturbed N is about ± 0.01 μm for R_{mod}. For σ, the absolute error varies, but does not exceed 0.07. For the volcanic scenario with a perturbed N profile it is obvious that a wrong particle number density assumption influences the retrieved profile, although this influence is rather small. The relative error in that case is less than 20% for R_{mod} and less than 10% for σ, maximum absolute errors for R_{mod} and σ are 0.04 μm and 0.1, respectively. The retrieval scenario with "unperturbed" PSD parameters results in the profiles which differ less than 2% from the true values. This characterizes the retrieval error resulting from the measurement noise. The retrieved albedo varies from 0.11 to 0.23 depending on the scenario and the wavelength.

Table 7.1. Selected scenarios and associated maximum of absolute (relative) errors in R_{mod}, σ and w.

Name	True				Color	Perturbation	Max.		
	R_{mod}, μm	r_g, μm	σ	w, μm			$\epsilon_{R_{mod}}$, μm	ϵ_σ	ϵ_w, μm
small	0.06	0.08	1.7	0.052	cian	R_{mod}, σ	0.01 (19%)	0.07 (5%)	0.001 (2%)
background	0.08	0.10	1.6	0.055	blue	R_{mod}, σ	0.01 (9%)	0.04 (2%)	$5{\cdot}10^4$ (1%)
unperturbed	0.11	0.12	1.37	0.041	brown	unpert.	0.002 (2%)	0.009 (1%)	$3{\cdot}10^4$ (1%)
volcanic	0.20	0.21	1.2	0.039	green	R_{mod}, σ	0.01 (5%)	0.04 (3%)	0.005 (13%)
volcanic (2N)	0.20	0.21	1.2	0.039	red	R_{mod}, σ, N	0.04 (19%)	0.1 (8%)	0.015 (40%)

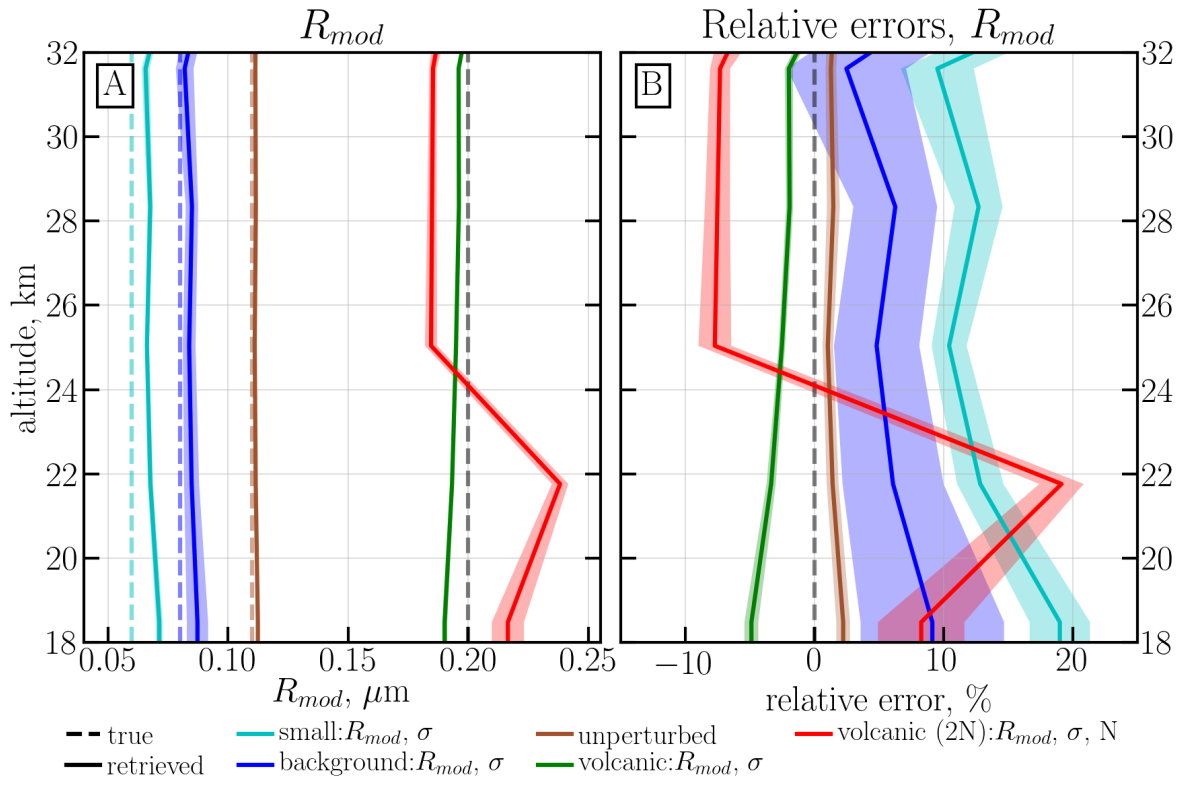

Figure 7.6. R_{mod} profiles (solid lines, panel A) and their relative errors (solid lines, panel B) for a typical tropical observation geometry. Synthetic retrievals for unperturbed parameters (brown lines), for small particles (cyan lines) and background case (blue lines) with perturbed R_{mod} and σ, as well as volcanic case with perturbed mode radius R_{mod} and σ (green lines), and with perturbed R_{mod}, σ and N in a layer (12-23 km) (red lines) with 100 different noise sequences were performed. True values are shown by dashed lines, shaded areas represent one standard deviation.

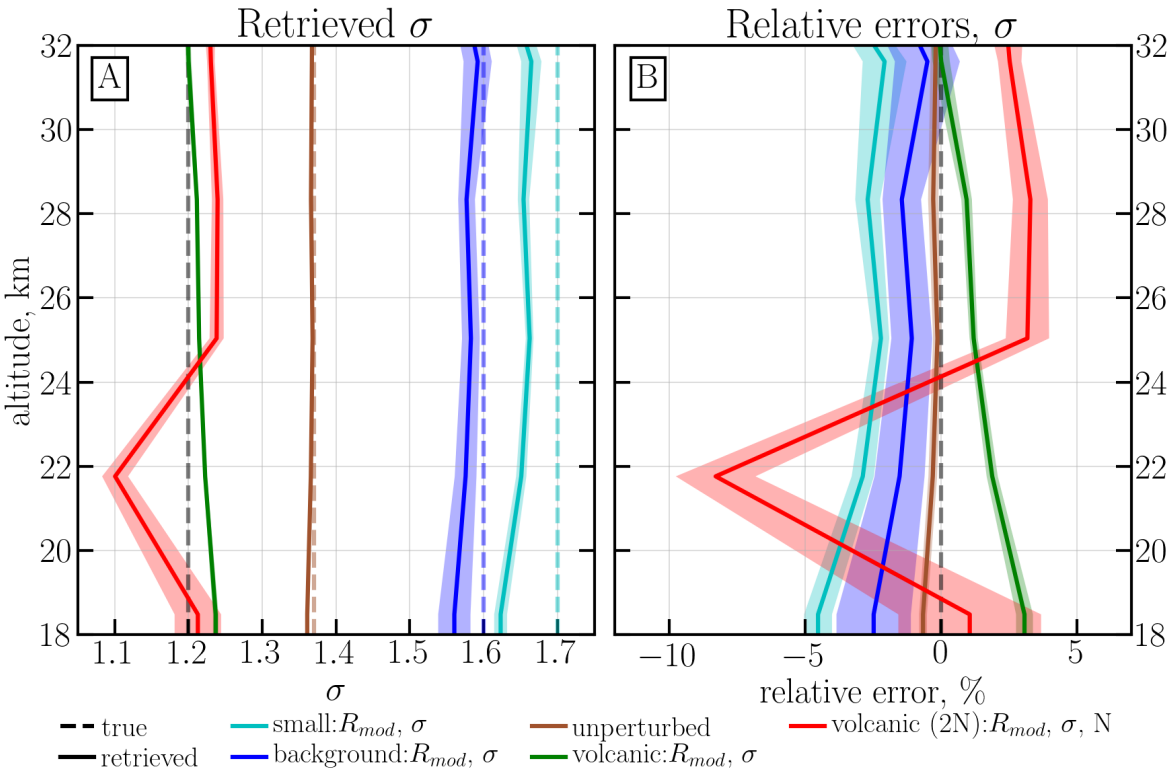

Figure 7.7. σ profiles (solid lines, panel A) and their relative errors (solid lines, panel B) for a typical tropical observation geometry. Synthetic retrievals for unperturbed parameters (brown lines), for small particles (cyan lines) and background case (blue lines) with perturbed R_{mod} and σ, as well as volcanic case with perturbed mode radius R_{mod} and σ (green lines), and with perturbed R_{mod}, σ and N in a layer (12-23 km) (red lines) with 100 different noise sequences were performed. True values are shown by dashed lines, shaded areas represent one standard deviation.

7.3.2. Absolute distribution width[1]

Referring to Sec. 1.5 it is important to remember that in the thesis when discussing the retrieval results w as given by Eq. (1.3) is analyzed rather than σ. Even though σ as a parameter is widely used in the retrievals and in the climate models, it doesn't provide visually interpretable information about the width of the particle size distribution, because it is defined relative to r_{med}. For this reason σ is used as a retrieval parameter, while w is used in the interpretation and discussion of the retrieval results. Therefore, it is important to asses retrieval uncertainties for w either.

In the panel A of Fig. 7.8, profiles of the w (solid lines), derived from the retrieved R_{mod} and σ, for each scenario are depicted. Similarly to Figs. 7.6 and 7.7, the dashed lines depict the true values. In the panel B of Fig. 7.8 relative errors are plotted by solid lines. Shaded areas in both panels of Fig. 7.8 show the standard deviation. Looking at Fig. 7.8, it is obvious, that the retrieval errors for w for small (cyan lines), background (blue lines) and unperturbed (brown lines) scenarios are rather small: absolute errors (Tab. 7.1) are less than 0.001 μm, and relative errors are below 2%. In the volcanic case

[1]This section was partially published in Malinina et al. [2018b].

with unperturbed N (green lines) differences are within 0.005 μm, which corresponds to 14%. On the contrary for the volcanic scenario with perturbed N (red lines), the derived w deviates from the true value by up to 40% (0.015 μm).

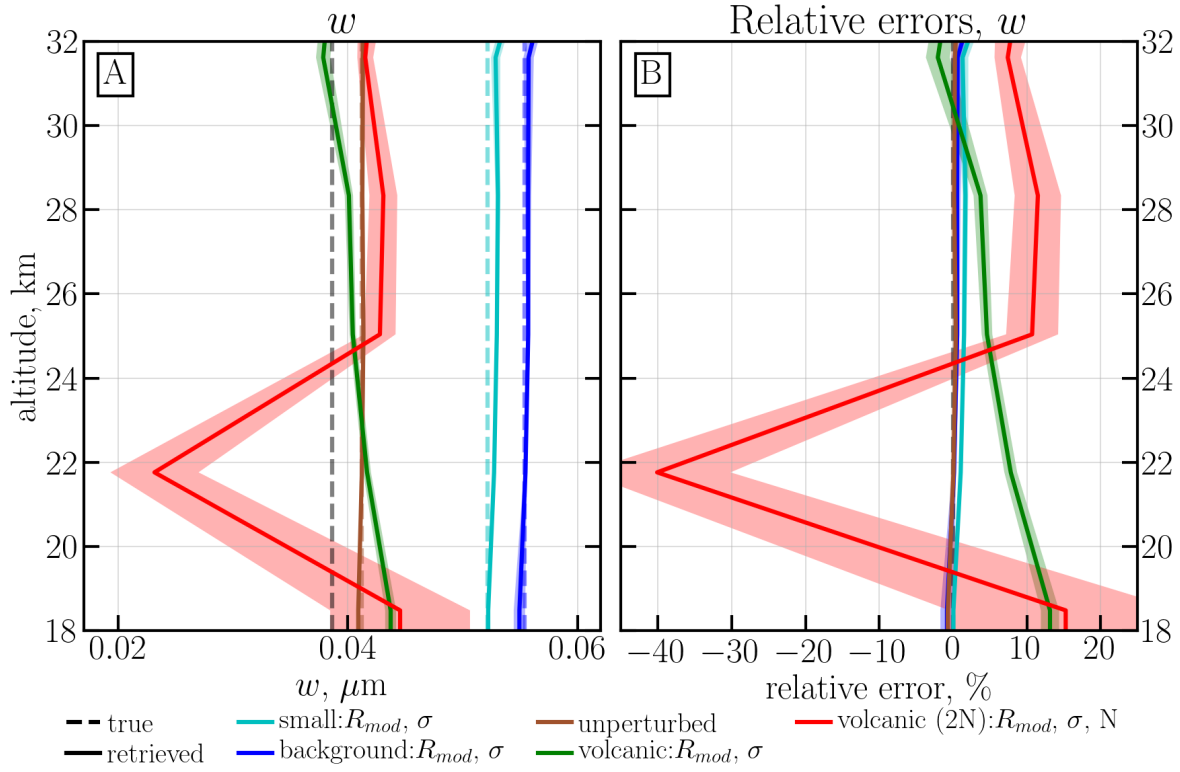

Figure 7.8. Absolute distribution width (w) profiles (solid lines, panel A) and their relative errors (solid lines, panel B) for a typical tropical observation geometry. Synthetic retrievals for unperturbed parameters (brown lines), for small particles (cyan lines) and background case (blue lines) with perturbed R_{mod} and σ, as well as volcanic case with perturbed R_{mod} and σ (green lines), and with perturbed R_{mod}, σ and N in a layer (12-23 km) (red lines) with 100 different noise sequences were performed. True values are shown by dashed lines, shaded areas represent one standard deviation.

Although the differences for R_{mod} and σ are comparably small, it is important to mention, that from all the modelled scenarios w for the volcanic scenarios is generally the smallest, and larger relative errors are often associated with the division by a small true value. To test this hypothesis another volcanic scenario with larger w ("wide") is simulated (R_{mod}=0.20 μm, σ=1.27, N profile is perturbed by the factor of 2 in a layer between 12 and 23 km) and run through the synthetic retrieval. The retrieved profiles of R_{mod}, σ and w are shown in Fig. 7.9, where solid lines show the retrieved profiles and dashed lines represent true values. In red, the standard "narrow" volcanic scenario with perturbed N is presented, whereas the magenta color depicts the "wide" scenario (see Tab. 7.2). Relative errors for these scenarios and parameters are presented in Fig. 7.10. From Figs. 7.9 and 7.10 it is clearly seen that even though the behaviour of R_{mod} and σ did not change significantly, and the absolute/relative errors are very similar for all three parameters, the maximum relative error for w decreased to 23%.

Table 7.2. Selected scenarios and associated maximum of absolute (relative) errors.

Name	True				Color	Perturbation	Max.		
	R_{mod}, μm	r_g, μm	σ	w, μm			$\epsilon_{R_{mod}}$, μm	ϵ_σ	ϵ_w, μm
narrow	0.20	0.21	1.2	0.039	red	R_{mod}, σ, N	0.04 (19%)	0.1 (8%)	0.015 (40%)
wide	0.20	0.21	1.27	0.053	magenta	R_{mod}, σ, N	0.05 (24%)	0.1 (8%)	0.012 (23%)

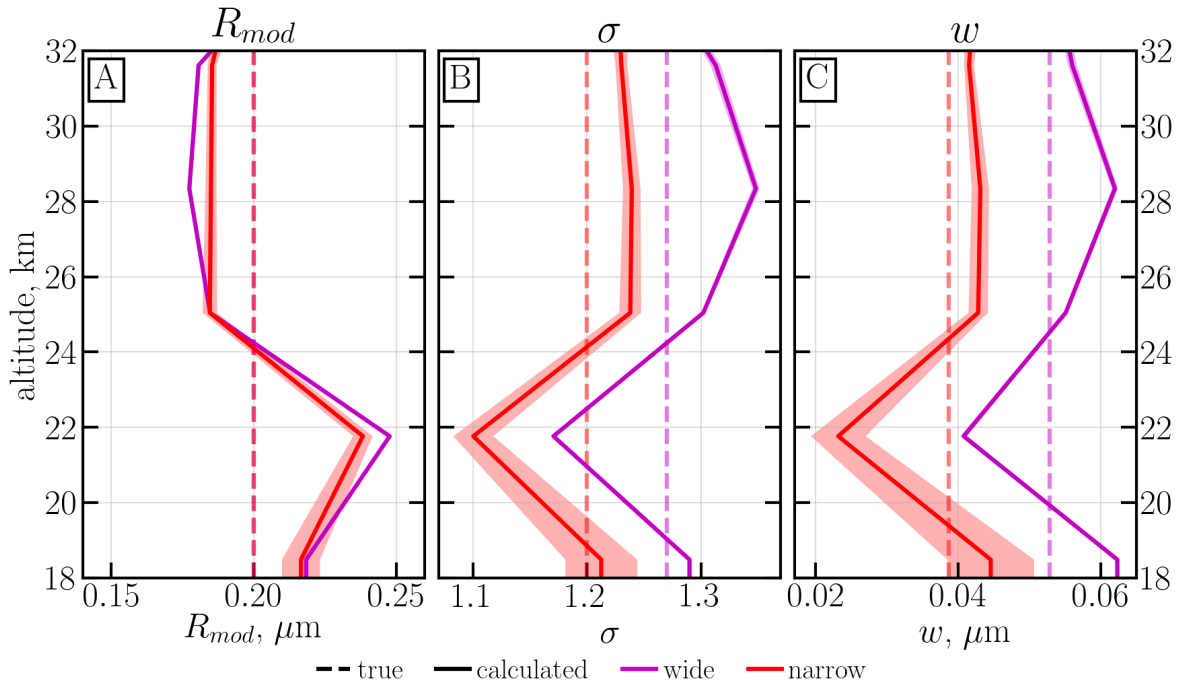

Figure 7.9. Retrieved profiles (solid lines) of R_{mod}, σ and derived values of w for the volcanic scenarios with perturbed R_{mod}, σ, N. Scenarios with smaller ("narrow", red lines) and larger ("wide", magenta lines) distribution width and 100 different noise sequences were considered. True values are shown by dashed lines, shaded areas represent one standard deviation.

7.3.3. Aerosol extinction coefficient [1]

As discussed in Sec. 1.6, *Ext* databases are widely used. In order to make SCIAMACHY aerosol PSD product comparable with the products from other satellite instruments, *Ext* at four wavelengths were calculated and then used to derive the Ångström exponents at two wavelength pairs.

For this study *Ext* is calculated employing Mie theory and Eq. (1.5) at 525, 750, 1020 and 1530 nm using the retrieved PSD information and the N profile assumed in the retrieval (exponentially decreasing from 15.2 cm^{-3} at 18 km to 0.5 cm^{-3} at 35 km). In addition, Ext_{750} is retrieved from the simulated radiances using an algorithm similar to SCIAMACHY v1.4 (see Sec. 4.1), but with the normalization to the solar spectrum and using a corrected phase function at each altitude, which is calculated from the retrieved R_{mod} and σ. For this retrieval the albedo value is set to the value resulting from the PSD parameters retrieval. To distinguish the two approaches to calculate extinctions,

[1] This section was partially published in Malinina et al. [2018a].

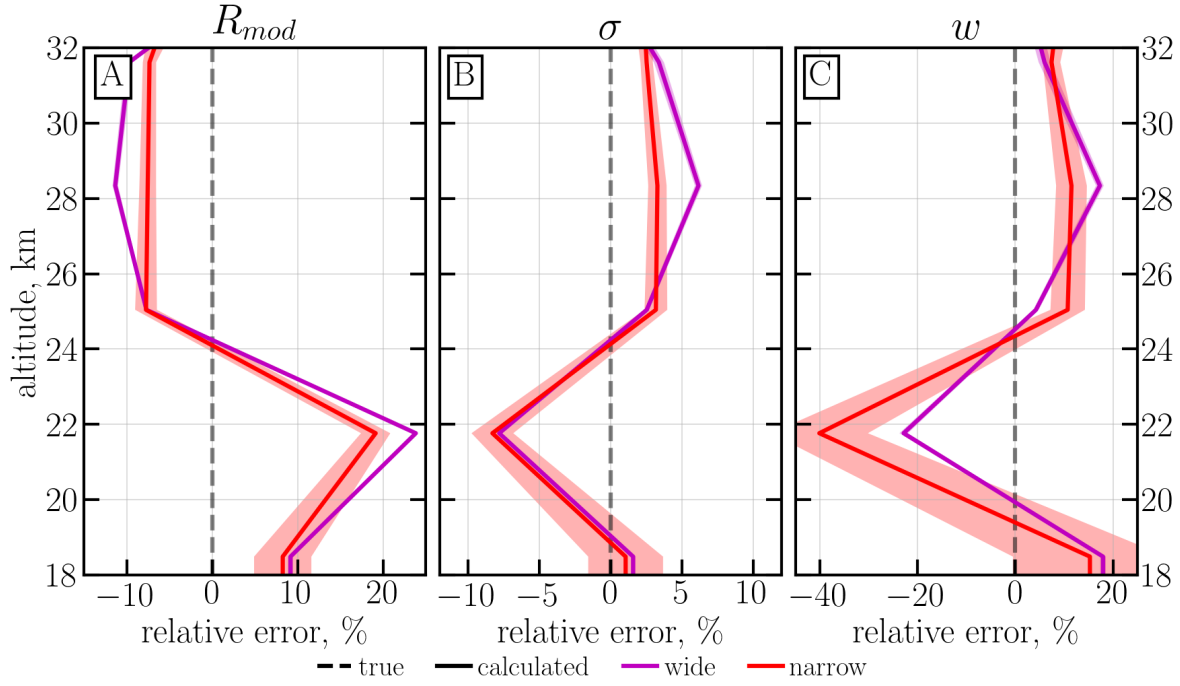

Figure 7.10. Relative errors for R_{mod}, σ and derived values of w for the volcanic scenarios with perturbed R_{mod}, σ, N. Scenarios with smaller ("narrow", red lines) and larger ("wide", magenta lines) distribution width and 100 different noise sequences were considered. Shaded areas represent one standard deviation.

Ext obtained with with Eq. (1.5) is denominated as "calculated" and Ext retrieved with the corrected PSD is called "retrieved".

Panel A of Fig. 7.11 shows the median calculated Ext_{750} profiles with solid lines and median retrieved Ext_{750} profiles with dashed lines. The "true" values are shown by the dotted lines. The colors corresponding to each scenario are listed in Tab. 7.3. Panel B shows the median relative errors for both calculated and retrieved Ext_{750}. Solid shaded areas show ± 1 standard deviation for the calculated profiles, while the striped ones denote ± 1 standard deviation for the retrieved profiles. The maximum relative errors for the calculated aerosol extinction coefficients at other wavelengths are presented in Tab 7.3. As the altitudinal behaviour of the extinction coefficients at the other wavelengths is the same as for the Ext_{750} profiles, the results are shown only for one wavelength.

Table 7.3. Selected scenarios and associated maximum of the relative errors in the aerosol extinction coefficients.

Name	True		Color	Perturbation	Max.			
	R_{mod}	σ			$\epsilon_{Ext_{525}}$	$\epsilon_{Ext_{750}}$	$\epsilon_{Ext_{1020}}$	$\epsilon_{Ext_{1530}}$
Small	0.06 μm	1.7	cian	R_{mod}, σ	20%	17%	15%	12%
Background	0.08 μm	1.6	blue	R_{mod}, σ	10%	9%	8%	7%
Unperturbed	0.11 μm	1.37	brown	unpert.	4%	4%	4%	4%
Volcanic	0.20 μm	1.2	green	R_{mod}, σ	7%	9%	10%	11%
Volcanic (2N)	0.20 μm	1.2	red	R_{mod}, σ, N	31%	26%	22%	19%

As it follows from Tab. 7.3, the relative errors for the scenarios with unperturbed N do

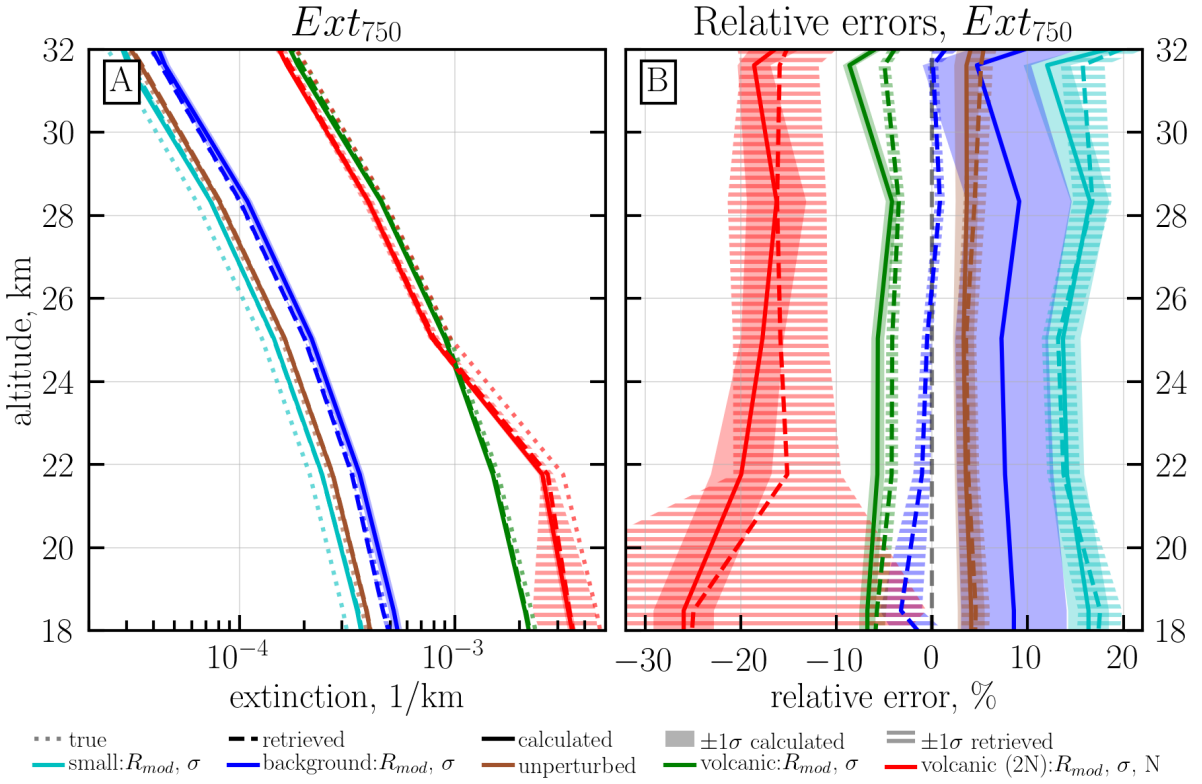

Figure 7.11. Profiles of Ext_{750} (panel A) and their relative errors (panel B) for a typical tropical observation geometry. The solid lines show the profiles calculated from PSD product, dashed lines depict the directly retrieved profiles, while the dotted lines represent the true values. The shaded areas stand for ± 1 standard deviation. The scenarios used for the simulations are listed in Table 7.3.

not exceed 20%. As expected, for the "volcanic (2N)" scenario, the errors are slightly higher and vary depending on the wavelength from 19% to 31%. For all scenarios the largest errors are observed for Ext_{525}. This is most likely because for the retrieval of PSD parameters only the wavelengths longer than 750 nm are taken into consideration, while the information from the visible and UV parts of the spectrum does not contribute to the process.

Analyzing Fig. 7.11 it is important to mention that retrieved Ext_{750} barely differs from the calculated ones. For "small", "unperturbed" and "volcanic" scenarios the solid and dashed lines are very close to each other, and the median relative errors of the retrieved profiles lay mostly inside the standard deviation of calculated profiles. For the "background" conditions the retrieved and the calculated profiles have the same shape, but the retrieved profiles are about 8% more accurate. As it was suggested that the difference between calculated and retrieved profiles of Ext might possibly be used to correct N for the PSD retrieval, it is most important to analyze the Ext profiles for the scenario with the perturbed N profile ("volcanic (2N)"). As it can be seen from the Fig. 7.11 A the retrieved Ext_{750} shows similar altitudunal behaviour as the calculated profile, although the retrieved profile has larger standard deviation at the lowermost altitude. Similarly to the calculated profile, the retrieved profile is about 25-30% lower than the "true" one. This leads to the conclusion, that an additional retrieval of Ext with the corrected PSD or fixing Ext during the retrieval does not provide any additional information about the

aerosol PSD, and some other independent data or constraint are needed to retrieve all three parameters. Possible solutions are discussed in Sec. 10.2.

7.3.4. Ångström exponent [1]

Combining Eqs. (1.5) and (1.6), the Ångström exponent can be obtained as

$$\alpha_{\lambda_1/\lambda_2} = -\frac{\ln(\beta_{aer}(\lambda_1, r_{med}, \sigma)/\beta_{aer}(\lambda_2, r_{med}, \sigma))}{\ln(\lambda_1/\lambda_2)}. \tag{7.4}$$

Equation (7.4) shows, that the Ångström exponent is not directly dependent on N, thus only the errors from R_{mod} and σ influence the derived $\alpha_{\lambda_1/\lambda_2}$. To assess this influence, the Ångström exponents are calculated using Eq. (7.4) and the calculated Ext from the synthetic retrievals discussed in Sec. 7.3.3. While from SCIAMACHY PSD product the Ångström exponents can be calculated at any wavelength pair, for considered comparison with OSIRIS and SAGE II (see Sec.8.4 and 8.3) the analysis is limited to $\alpha_{525/1020}$ and $\alpha_{750/1530}$. The "true" Ångström exponent values, the scenario summaries as well as the maximum absolute and relative errors for $\alpha_{525/1020}$ and $\alpha_{750/1530}$ are presented in Tab. 7.4. As for Ext analysis, the altitudinal behavior only for one wavelength pair ($\alpha_{750/1530}$) is shown, the results for the second one are very similar. In panel A of Fig. 7.12 the median derived Ångström exponents are presented with solid lines, and the "true" values are shown by dashed lines; in the panel B median relative errors for the chosen scenarios are depicted. For both panels shaded areas show ± 1 standard deviation.

Analysis of Tab. 7.4 and Fig. 7.12 leads to the conclusion that the relative error in the Ångström exponent for all scenarios is below 10% for $\alpha_{525/1020}$, and less than 5% for $\alpha_{750/1530}$. As expected, the largest errors are seen for the "volcanic (2N)" scenario, where the N profile is perturbed and the errors in R_{mod}, σ and Ext are the largest. For all scenarios the largest errors are observed at the lowermost retrieved altitude, e.g. for $\alpha_{750/1530}$ the errors above 21.3 km do not exceed 2.5%. The absolute error for $\alpha_{525/1020}$ is less than 0.12 for the scenarios with unperturbed N and about 0.2 for the scenario with N perturbed by a factor of 2. For $\alpha_{750/1530}$ the absolute errors are even smaller, in particular, for the scenarios with the same N as used for the retrieval the errors are smaller than 0.1, and for the "volcanic (2N)" scenario the difference between the true and derived Ångström exponent is 0.15.

[1] This section was partially published in Malinina et al. [2018a].

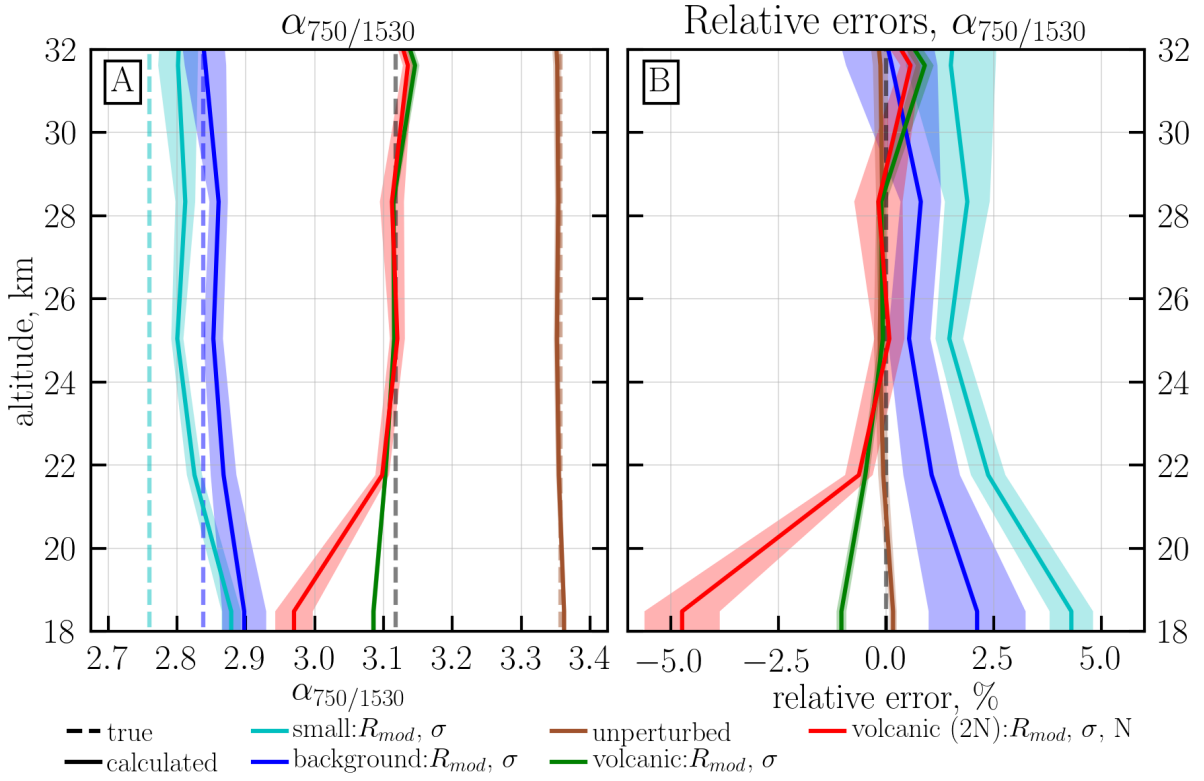

Figure 7.12. Ångström exponent profiles ($\alpha_{750/1530}$) (a) and their relative errors (b) for a typical tropical observation geometry. The solid lines show the derived from PSD product profiles, while the dashed lines represent the true values. The shaded areas stand for ± 1 standard deviation. The scenarios used for the simulations are listed in Table 7.4.

Table 7.4. Selected scenarios and associated maximum of absolute (relative) errors in Ångström exponents.

Name	True				Color	Perturbation	Max.	
	R_{mod}	σ	$\alpha_{525/1020}$	$\alpha_{750/1530}$			$\epsilon_{\alpha_{525/1020}}$	$\epsilon_{\alpha_{750/1530}}$
Small	0.06 μm	1.7	2.18	2.76	cian	R_{mod}, σ	0.12 (4.8%)	0.10 (4.3%)
Background	0.08 μm	1.6	2.22	2.84	blue	R_{mod}, σ	0.05 (2.4%)	0.06 (2.1%)
Unperturbed	0.11 μm	1.37	2.76	3.36	brown	unpert.	0.01 (0.3%)	0.01 (0.2%)
Volcanic	0.20 μm	1.2	2.41	3.12	green	R_{mod}, σ	0.04 (1.6%)	0.03 (1.0%)
Volcanic (2N)	0.20 μm	1.2	2.41	3.12	red	R_{mod}, σ, N	0.20 (8.3%)	0.15 (4.7%)

8

Aerosol particle size dataset and its validation

8.1. Tropical PSD parameters database [1]

Here, the results of the retrieval of the aerosol PSD parameters from SCIAMACHY limb observations are presented. As it was mentioned above (Sec. 6), the retrieval algorithm was applied to data for the tropical region and completely cloud free (from 0 km) scenes, resulting in 9727 profiles for the entire SCIAMACHY observation period. The cloud filtering algorithm by Liebing [2016] used in this study employs a probability approach, which means that there is still a 10% chance of cloud or its fraction to influence the profile. Thus, to reject possible unreasonable results, post-retrieval filtering criteria were applied as follows: values with R_{mod}<0.03 μm were rejected, as they are lying outside the sensitivity range of the instrument. The value is somewhat lower than the one presented in Sec. 7.2. This is because for the study, presented in Sec. 7.2 the distributions with w=0.01μm were taken into consideration, but in reality such distributions are highly improbable for the small particles. According to retrieved data for the distributions with R_{mod}=0.06 μm mean w value is around 0.05 μm. However, the sensitivity threshold (S >0.01) is already reached for the distributions with R_{mod}=0.03 μm and w=0.02 μm. For that reason the real filtering threshold is lowered. Additionally, Ext at 750 nm calculated using the retrieved PSD parameters is not allowed to exceed 0.0015 km^{-1}. A similar approach to filter the Ext was used to reject cloudy scenes in SCIAMACHY V1.4 and OMPS V1.0.9 Ext product (see Ch. 4). The implemented filters result in rejecting about 2% of the values. Non-converged retrievals with 100 iterations (4.6% of the whole amount of retrieved profiles) are also excluded. No additional filtering criteria are implemented. The maximum mode radius in the retrieved data set reaches the value R_{mod}=0.21 μm, and σ varies from 1.02 to 2.9. All the values are considered to be realistic within the reported errors.

As the temporal sampling of the current product is not sufficient to analyze the volcanic plumes, monthly zonal (20°N-20°S) means are used to evaluate the overall state of the stratosphere during the SCIAMACHY observation period. These monthly averaged values

[1] This section was partially published in Malinina et al. [2018b].

of R_{mod} and w are presented in Figs. 8.1 and 8.2, respectively. Here, some obvious patterns such as the increase of the values after most of the volcanic eruptions (dashed lines) can be readily identified. In addition, there is a pronounced seasonality in both R_{mod} and w. As the seasonal cycle of stratospheric aerosols has already been discussed by several authors [Hitchman et al., 1994, Bingen et al., 2004] and in Chs. 1 and 5, this study focuses on the analysis of the anomalies of the PSD parameters. Anomalies or deseasonalized values for R_{mod} and w, as shown in Figs. 8.3 and 8.4, respectively, are obtained by subtracting from each monthly mean value an average over all corresponding months in the whole observation period (e.g. the average value for all the Januaries of the 10 year period is subtracted from each January monthly mean value in the observation period).

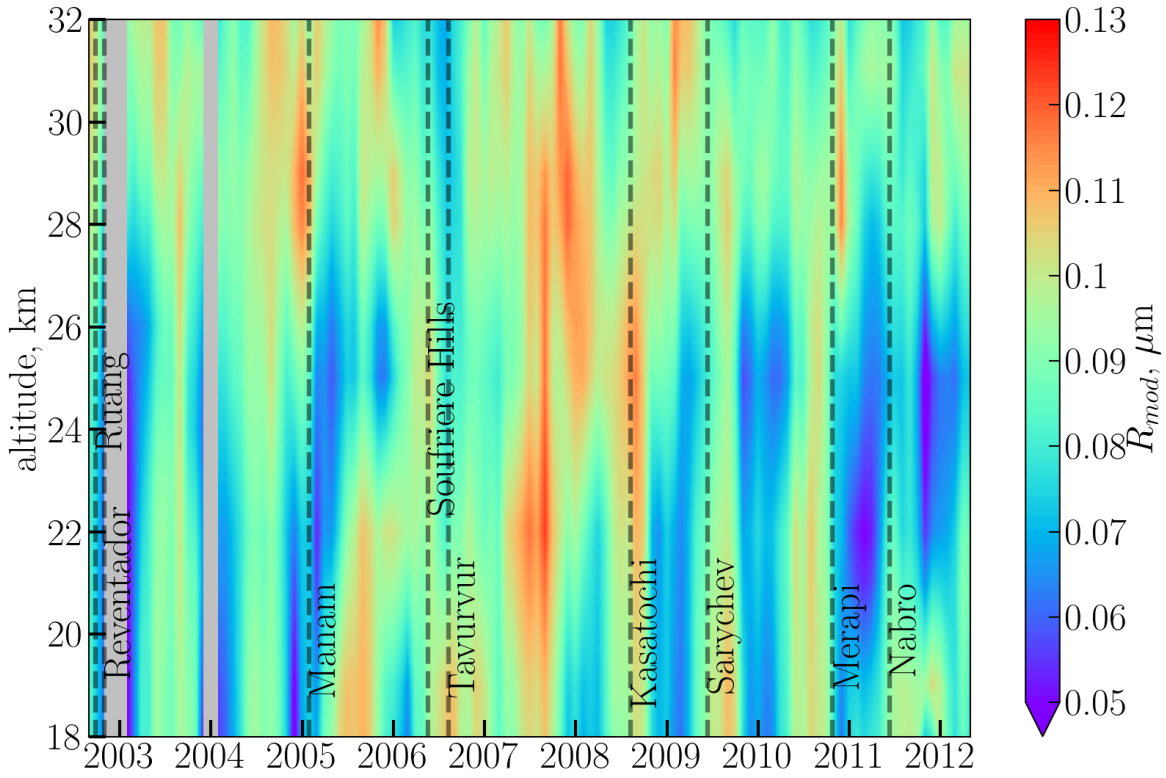

Figure 8.1. Monthly zonal mean values of R_{mod} retrieved from SCIAMACHY limb data in the tropics (20°N - 20°S).

Analyzing the anomalies for R_{mod} presented in Fig. 8.3 it can be noticed, that there is a distinct increase of R_{mod} in the lower altitudes after most of the volcanic eruptions, except for the eruptions of Ruang and Reventador in late 2002 and Merapi in late 2010. For these tropical eruptions only a slight increase in R_{mod} is observed. This may be related to a smaller amount of SO_2 (less than 100 kt) released during these eruptions (see database of the Smithsonian Institution [2017] or Bingen et al. [2017]). Another important feature is a periodic variation of R_{mod} in the 28-32 km range, related to the QBO. A similar QBO signature in the *Ext* retrieved from SCIAMACHY limb measurement at altitudes around 30 km was reported by Brinkhoff et al. [2015] and in Sec. 5.1.1. Those signatures were explained by the influence of the secondary meridional circulation. The QBO pattern is also seen in the anomalies of w (Fig. 8.4). Volcanic eruptions influence aerosol w in different ways. As for R_{mod} there is an increase of w after Tavurvur, Kasatochi, Sarychev

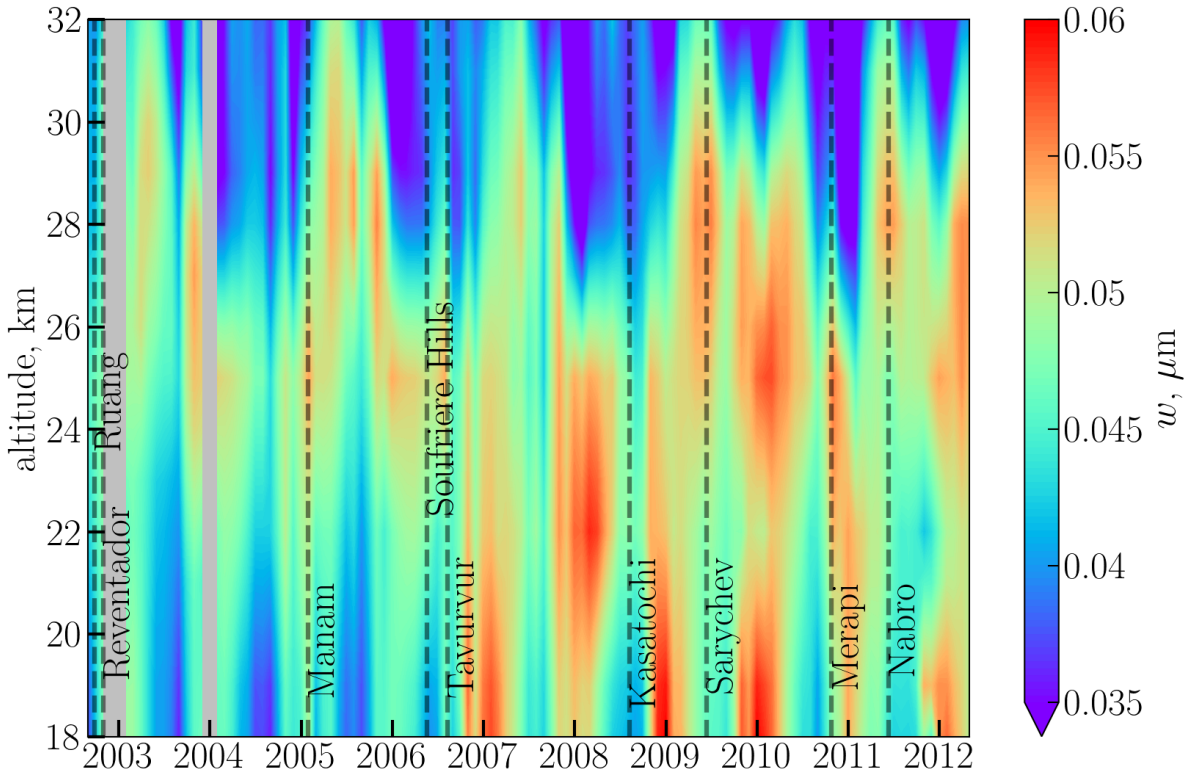

Figure 8.2. Monthly zonal mean values of w as defined by Eq. (1.3) retrieved from SCIAMACHY limb data in the tropics (20°N - 20°S).

and Merapi eruptions, while a slight decrease of w at some altitudes after Nabro eruption and no change in w at all altitudes after the Manam eruption is observed.

Following the strong tropical eruptions (Manam, Tavurvur, Nabro) there is a well-defined increase in R_{mod} shortly after the eruptions in the 18 – 21 km altitudes, while at higher altitudes (22–26 km) the volcanic perturbation is observed with a specific time lag. This is the so called tape recorder effect, which is associated with the vertical transport of air masses in the tropical stratosphere. After strong mid-latitude eruptions (Sarychev, Kasatochi) the increase in R_{mod} is less pronounced as compared to the tropical volcanoes, though there is a definite increase in w. There are two possible explanations of this effect. First, the initial growth in particles is a result of the oxidation of SO_2 to H_2SO_4, and the chemical rate of this reaction depends on the ambient physical conditions. Second, during the transport of the air masses from the mid-latitudes to the tropics the aerosol PSD is modified as a result of sedimentation of heavier particles with large radii. Unfortunately the justification for these hypotheses can be provided only after implementing the current algorithm for the extra-tropical latitudes and modelling the eruptions accounting for the aerosol microphysics, which is planned for the future (see Sec. 10.2).

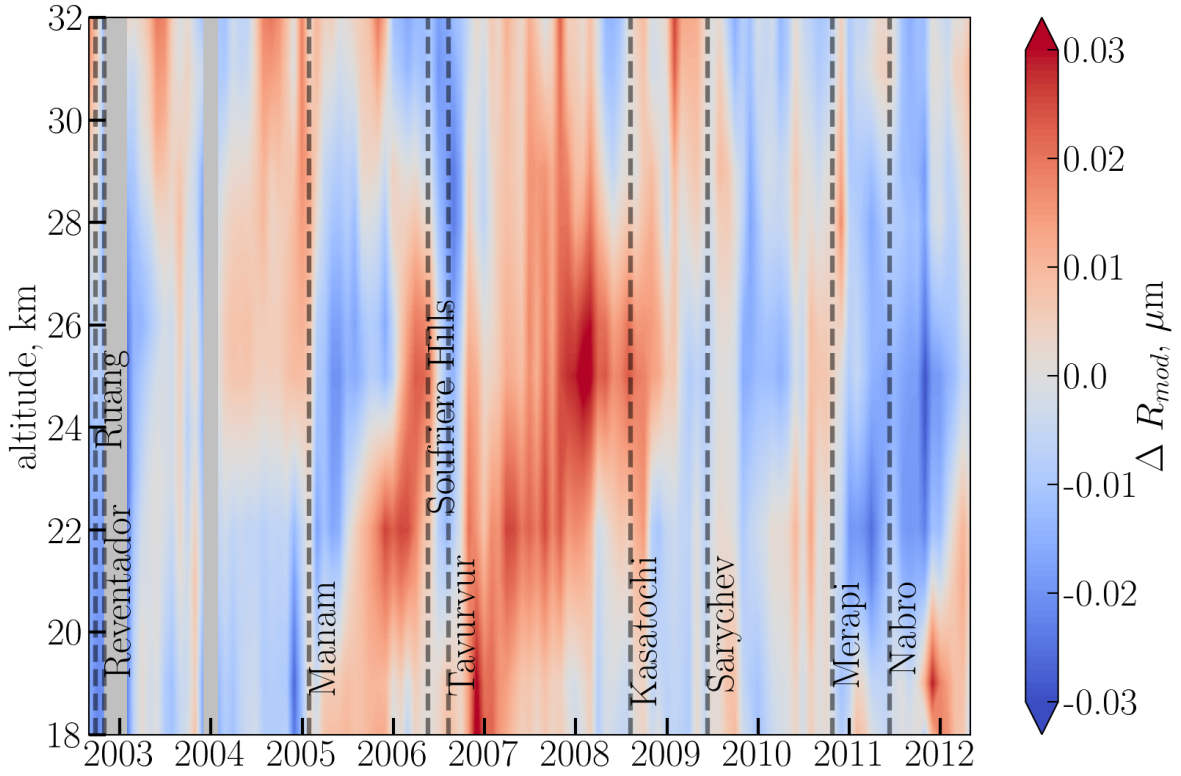

Figure 8.3. Deseasonalized time series (anomalies) of R_{mod} retrieved from SCIAMACHY limb data in the tropics (20°N - 20°S).

8.2. Tropical Ångström exponent database [1]

In this section the SCIAMACHY data set is analyzed in order to investigate the behavior of the Ångström exponent with the time and to understand its dependency on the PSD parameters. As it was mentioned in Sec. 8.1, due to rejection of cloud contaminated profiles temporal sampling of the obtained product is too sparse to analyze volcanic plumes. For this reason the monthly zonal mean (20° S-20° N) $\alpha_{750/1530}$ as shown in Fig. 8.5 are considered. With exception of the upper altitudes (26-32 km), where the QBO pattern is obvious, the seasonal variation of the $\alpha_{750/1530}$ represents the dominating pattern seen in Fig. 8.5. To illustrate the Ångström exponent behaviour after the volcanic eruptions more clearly, $\alpha_{750/1530}$ is deseasonalized using the same approach as discussed in Sec. 8.1. The deseasonalized $\alpha_{750/1530}$ time series are presented in Fig. 8.6. It should be noted, that in Fig. 8.6 the increased Ångström exponent values are shown in blue, and decreased in red, as the increased $\alpha_{750/1530}$ is often considered as a decrease of the aerosol particle size, and vice versa.

Looking at Fig. 8.6, it becomes more evident that the QBO pattern is well pronounced at altitudes above 26 km. This agrees with earlier results (see Sec. 5.1.1 and 8.1). The deseasonalized $\alpha_{750/1530}$ time series also demonstrate the influence of multiple volcanic eruptions. The slight decrease of $\alpha_{750/1530}$ is noticed after the Tavurvur eruption, and more significant after the extra-tropical Kasatochi and Sarychev eruptions. Almost no

[1] This section was partially published in Malinina et al. [2018a].

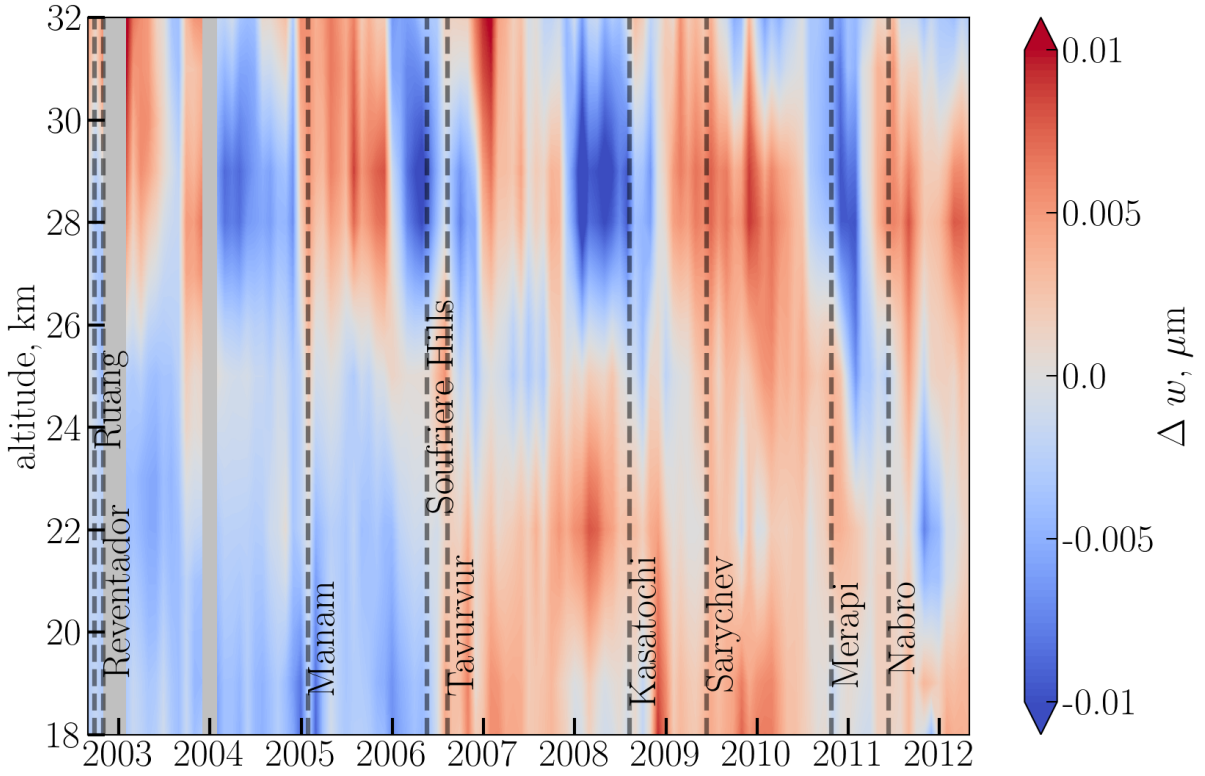

Figure 8.4. Deseasonalized time series (anomalies) of w as defined by Eq. (1.3) retrieved from SCIAMACHY limb data in the tropics (20°N - 20°S).

change in $\alpha_{750/1530}$ is observed after Ruang, Reventador and Manam eruptions. After the Nabro eruption $\alpha_{750/1530}$ increases at the 18-23 km altitude. As for R_{mod} and w, the changes in $\alpha_{750/1530}$ reach higher altitudes with a certain time lag (tape-recorder effect). Interestingly, the general behaviour of $\alpha_{750/1530}$ looks very similar to that of w (see Fig. 8.4). To evaluate it in more detail the dependency of $\alpha_{750/1530}$ on R_{mod} and w is analyzed.

It is well known, that $\alpha_{750/1530}$ is dependent on both, r_{med} and σ, but as R_{mod} and w are derived from these parameters, their impact on $\alpha_{750/1530}$ is not obvious. To investigate these relationships, the results from individual measurements in the tropical region over the whole observation period of SCIAMACHY are presented in Fig. 8.7. In the left panel, $\alpha_{750/1530}$ at all altitudes is presented as a function of R_{mod} and w, while in the right panel the dependency of $\alpha_{750/1530}$ on r_{med} and σ is shown. The colors in Fig 8.7 depict the magnitude of $\alpha_{750/1530}$. From Fig. 8.7, it is clear that any particular value of $\alpha_{750/1530}$ can result from an infinite number of combinations of R_{mod} and w (or r_{med} and σ). However, it should be noted that retrieving a pair of R_{mod}/r_{med} and w/σ is not the only way to obtain the Ångström exponent. As was discussed in Sec. 7.1, in the spectral interval from 750 to 1530 nm the radiance can be fitted by two out of three PSD parameters, for SCIAMACHY the pair R_{mod} and σ is chosen as the limb radiances sensitivity to these parameters is higher than to N. However, it is possible to obtain a correct Ångström exponent also by retrieving, e.g., r_{med} and N [Rieger et al., 2014], although the accuracy of the obtained PSD parameters may be not as high as for R_{mod} and σ.

Comparing left and right panels it can be seen, that $\alpha_{750/1530} = f(R_{mod}, w)$ is a non-

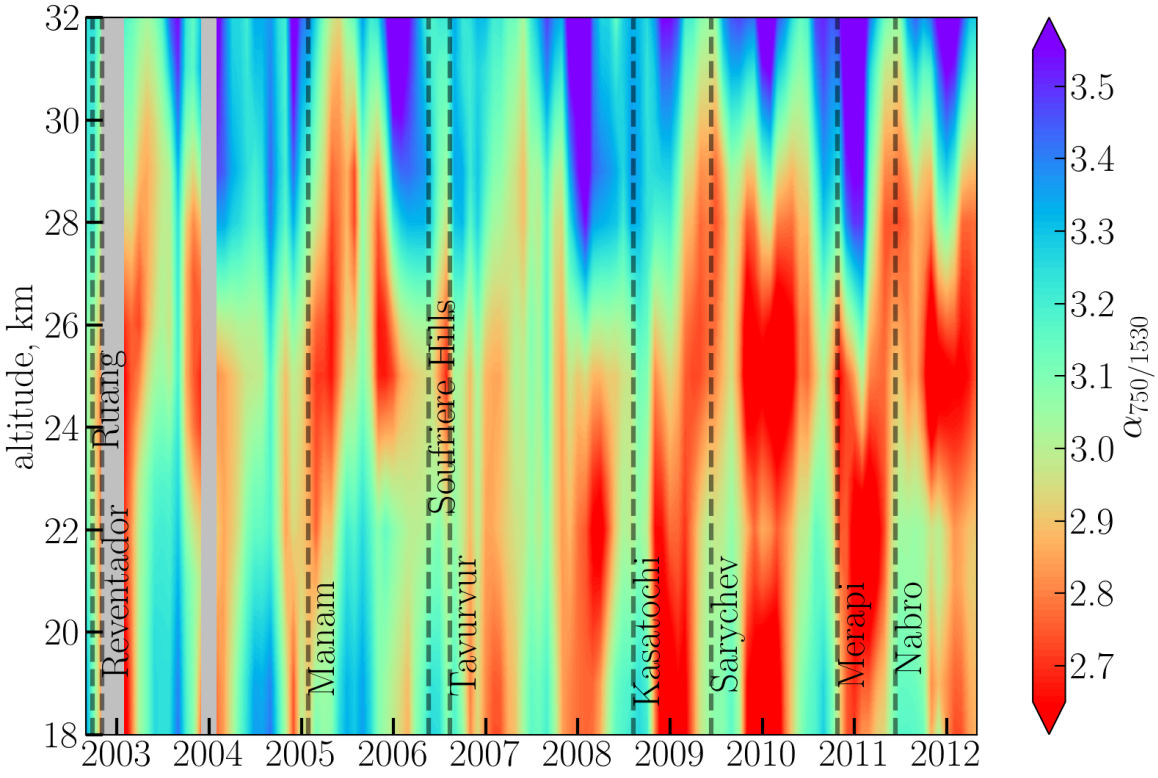

Figure 8.5. Monthly zonal mean values of the Ångström exponents ($\alpha_{750/1530}$) derived from SCIAMACHY limb data in the tropics (20° N - 20° S).

monotonic function, i.e. up to a turn-around point the same value of $\alpha_{750/1530}$ is obtained by increasing both, R_{mod} and w, and then the same $\alpha_{750/1530}$ is a result of increasing R_{mod} and decreasing w. The function $\alpha_{750/1530} = f(r_{med}, \sigma)$ is monotonic with respect to both, r_{med} and σ, and there is the general rule: the larger is r_{med} or σ, the smaller is $\alpha_{750/1530}$. The same value of $\alpha_{750/1530}$ can be reached by increasing r_{med} and decreasing σ or vice versa. It is important to highlight, that completely different distributions might result in the same value of $\alpha_{750/1530}$. To illustrate this fact, three pairs of PSD parameters with $\alpha_{750/1530}$=3.17 are chosen, and their PSD functions dn/dr are depicted in Fig. 8.8. The values of R_{mod}, σ and w used for the figure are listed in the legend. This figure disproves a widely spread belief, that smaller Ångström exponents are associated with the prevalence of larger particles and vice versa. As it can be seen, distributions with R_{mod}=0.07 μm and w=0.045 μm (green line) and R_{mod}=0.16 μm and w=0.044 μm (red line) have completely different amounts of large particles, but result in the same Ångström exponent. As it was already noted by Ångström [1929], α has only an "approximate coincidence with the average diameter directly measured". Thus, it can be concluded, that, firstly, there is no possibility to obtain a unique pair of PSD parameters from the known value of $\alpha_{750/1530}$, and secondly, to provide a relevant information on the change in the particle size, $\alpha_{750/1530}$ should be given with one of the PSD parameter. Here, it should be noted, that these conclusions are valid for the Ångström exponent at one wavelength pair. In case Ångström exponents at multiple independent wavelength pairs are provided, more information on PSD can be derived. However, for all known spaceborne instruments providing aerosol information in the stratosphere only one value of Ångström exponent is reported in peer-reviewed publications, which makes our conclusions applicable to all of

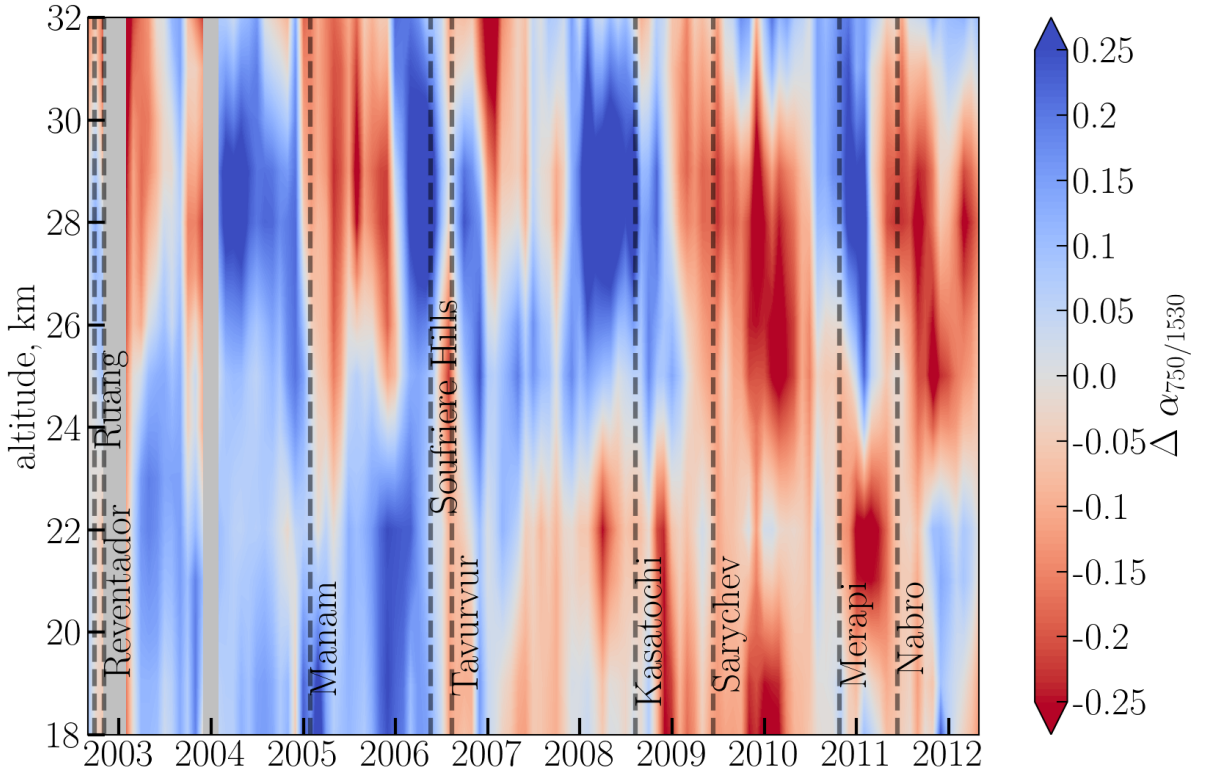

Figure 8.6. Deseasonalized time series (anomalies) of the Ångström exponents ($\alpha_{750/1530}$) derived from SCIAMACHY limb data in the tropics (20° N - 20° S).

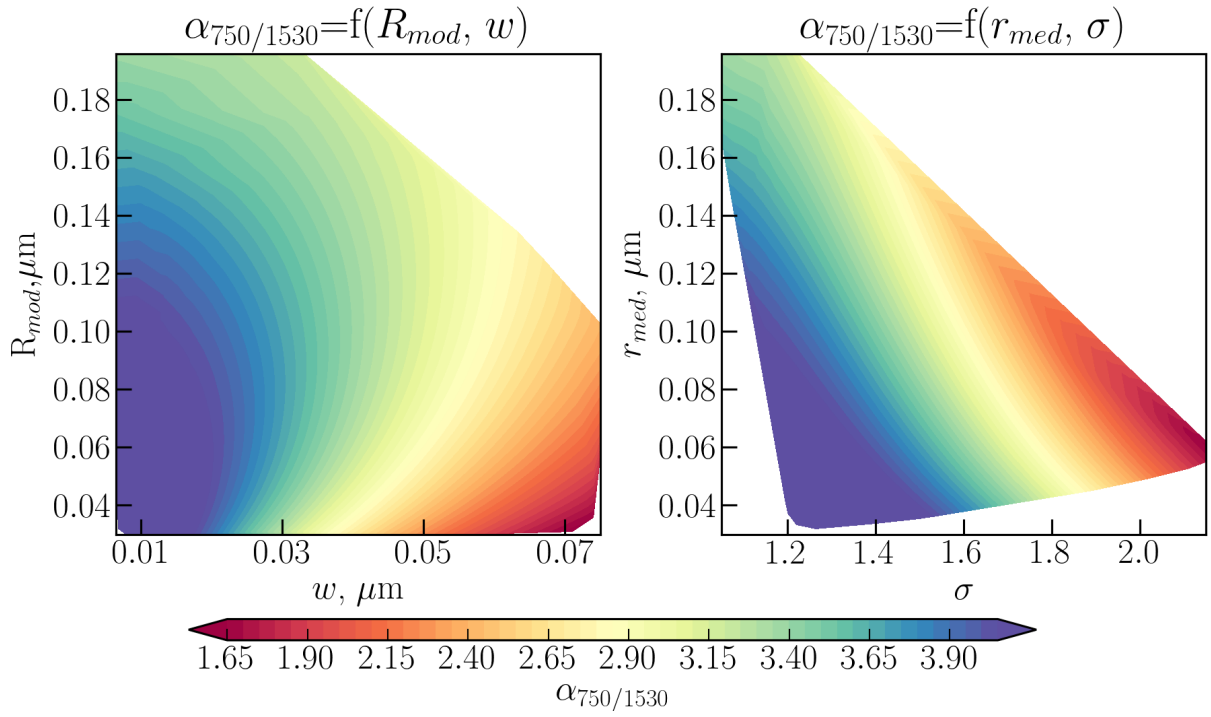

Figure 8.7. Dependence of the Ångström exponent ($\alpha_{750/1530}$) on R_{mod} and w (left panel). In right panel $\alpha_{750/1530}$ as a function of r_{med}, and σ is presented. Plot is based on the SCIAMACHY limb data in the tropics (20° N - 20° S).

them.

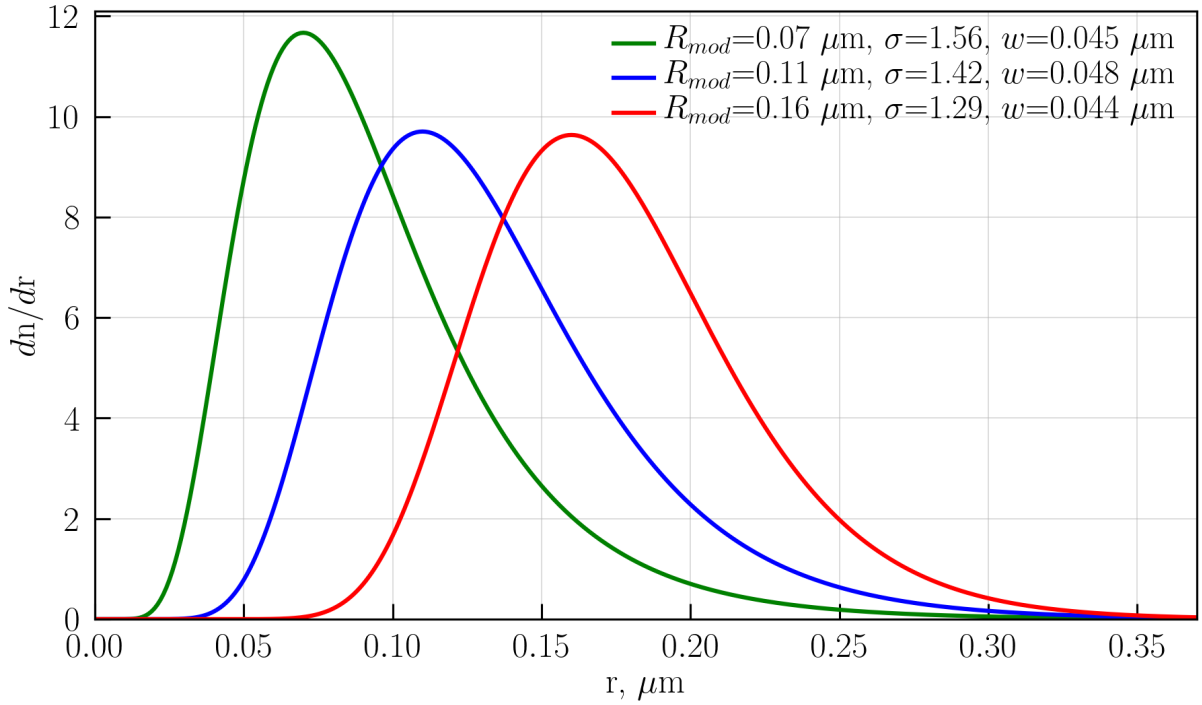

Figure 8.8. Example of aerosol particle size distributions with $\alpha_{750/1530}$=3.17. For convenience, N=1 cm^{-3}.

8.3. Comparisons with SAGE II [1]

As mentioned in Sec. 2.4, SAGE II was one of the key instruments providing stratospheric aerosol information. Operating from 1984 till 2005 SAGE II had a 3 years overlap with SCIAMACHY, enabling to use it as a comparison instrument in the assessment of SCIAMACHY aerosol PSD product. This comparison, however, is associated with some challenges. The first one is related to the number of collocated profiles. Unlike the comparison of the *Ext* in Sect. 5.1.2, the comparison of the aerosol particle size products suffers from the difference in SCIAMACHY and SAGE II spacial sampling. As a solar occultation instrument, SAGE II provides about 30 profiles per day, while the SCIAMACHY sampling is reduced due to limitation of the PSD retrieval algorithm to completely cloud free profiles in the tropical zone (20° S-20° N). Thus, applying quite loose collocation criteria of ±5° latitude, ±20° longitude and ±24 hours just 57 coincident profiles were found. This amount of profiles is not enough for an in-depth investigation, however a rough estimate of the instruments agreement can be provided. Another issue is related to the differences in the measurement techniques and, thus, a different sensitivity to aerosol properties. As it was shown in Sec. 7.2, employing an occultation measurement technique, SAGE II is less sensitive to the smaller particles, while its *Ext* retrieval is associated with smaller

[1] This section was published in parts in Malinina et al. [2018a,b].

uncertainties. The limb measurements from SCIAMACHY, in turn, are more sensitive to the particles with r <0.10 μm, although the direct retrieval of Ext is associated with some issues (see Secs. 5.1 and 7.2 for details). Thus, it is essential to provide comparisons not only for r_{eff}, reported by SAGE II, but also for Ext and Ångström exponents obtained from SCIAMACHY PSD product.

As a first step r_{eff} is considered. As mentioned in Sect. 8.2, r_{eff} can not be uniquely transferred to the aerosol PSD parameters, however, similarly to the Ångström exponent, it provides some limited information on the size of the particles. In the used version of the SAGE II product, r_{eff} is provided, while for SCIAMACHY it is possible to recalculate this parameter using Eq. (1.4). As SCIAMACHY vertical sampling is coarser than that of SAGE II, and SCIAMACHY retrievals are performed on a coarser altitude grid (3.3 km compared to 0.5 km by SAGE II), SAGE II data is first smoothed to the SCIAMACHY vertical resolution and afterwards interpolated onto the SCIAMACHY vertical grid.

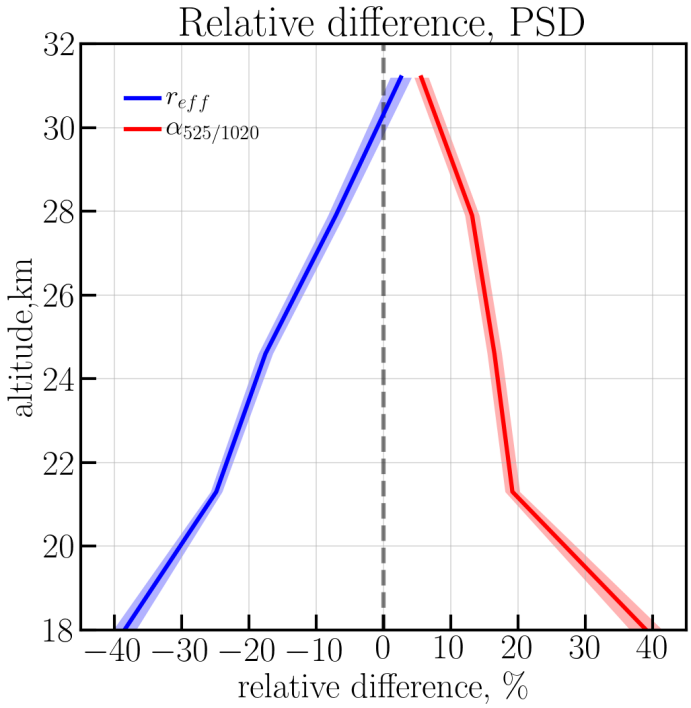

Figure 8.9. Mean relative difference (200×(SCIAMACHY-SAGE II)/ (SCIAMACHY+SAGE II)) between effective radii (blue line) and Ångström exponent (red line) from collocated SCIAMACHY and SAGE II measurements. The shaded areas show standard error of the mean.

Mean relative difference between the r_{eff} of the both instruments is presented in Fig. 8.9 with the blue line, the shaded area shows the standard error of the mean. Here and further in the thesis it is preferred to depict the standard error of the mean instead of the standard deviation to make the figures less busy. The relative difference in r_{eff} is about 40% in the lower altitudes decreasing with increasing height to less than 15% at 26 km and around 0% at 30 km. As it can be seen in Fig. 8.10, where both collocated data sets are plotted versus time, the offset between SCIAMACHY (blue dots) and SAGE II (red dots) r_{eff} is constant with the time with SCIAMACHY being systematically lower at 18 and 21.3 km. The reason of the observed differences is the lower sensitivity of SAGE II to the particles with radius smaller than 0.1 μm [Thomason et al., 2008]. As

it was shown earlier in Sec. 7.2, for limb measurements the sensitivity drops for particles smaller than 0.06 μm, while for solar occultation instruments this threshold is somewhat higher. As the period from 2002 to 2005 was considered to be volcanically quiescent, smaller particles were dominating at the time, increasing the possible biases, and thus, the observed differences are expected. However, for a more detailed evaluation of this aspect, larger amount of collocations needs to be analyzed. It can as well provide possible reasons for the observed lopsided differences.

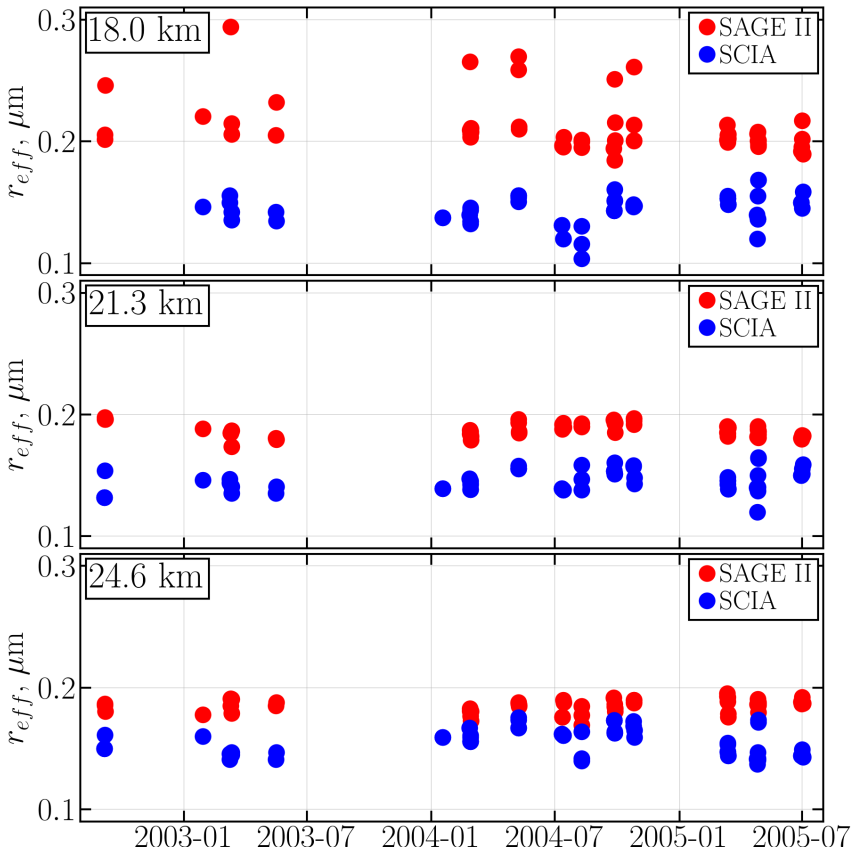

Figure 8.10. Effective radii from collocated SCIAMACHY and SAGE II measurements at 18, 21.3, 24.6 km altitude.

Due to the differences in the measurement techniques and in the sensitivity to the different aerosol parameters, it was decided to compare *Ext* retrieved from SAGE II and that calculated from SCIAMACHY PSD product, because it is supposed to be more reliable than r_{eff} comparison.

To perform the comparison, SCIAMACHY *Ext* at 525, 750 and 1020 nm are calculated with Eq. (1.5), using the same N profile as in the PSD retrieval. As SAGE II did not have a 750 nm channel, Ext_{750} for this instrument is calculated with Eq. (1.6) from Ext_{525} and Ext_{1020} using $\alpha_{525/1020}$. To assess a possible uncertainty associated with the usage of the Ångström exponent when calculating Ext_{750} from SAGE II data, SCIAMACHY Ext_{750} is additionally calculated using the same approach. To distinguish between two different methods of Ext_{750} calculation, $Ext_{750}(PSD)$ is used for the one derived from PSD product with Eq. (1.5), and $Ext_{750}(\alpha_{525/1020})$ for that calculated using the Ångström exponent. As for r_{eff} comparison, SAGE II data is smoothed to SCIAMACHY vertical resolution

and then interpolated onto the SCIAMACHY vertical grid. The mean relative differences between SCIAMACHY and SAGE II for Ext_{525} (blue line), Ext_{1020} (green line), $Ext_{750}(PSD)$ (red line) and $Ext_{750}(\alpha_{525/1020})$ (magenta line) are presented in Fig.8.11. The shaded areas show the standard error of the mean.

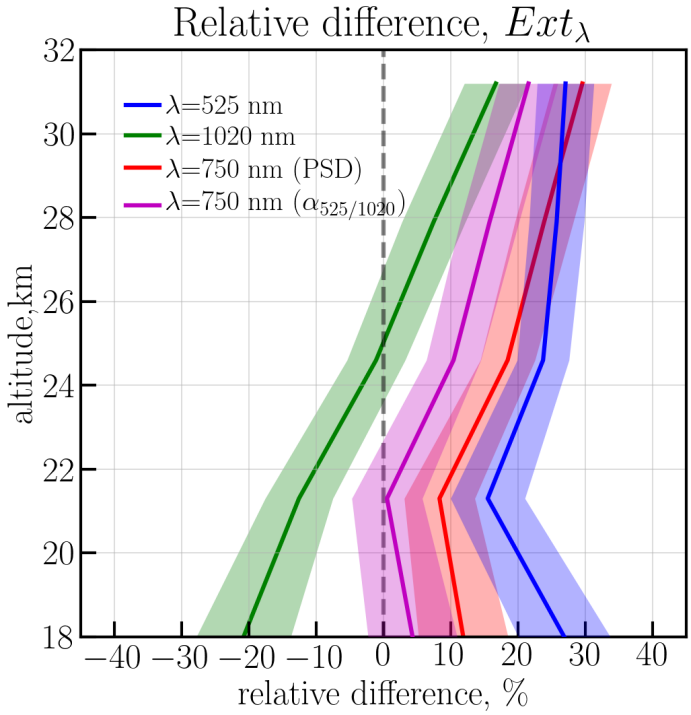

Figure 8.11. Mean relative difference (200×(SCIAMACHY-SAGE II)/ (SCIAMACHY+SAGE II)) between extinction coefficients at 525 nm (blue line), 1020 nm (green line), 750 nm obtained directly from PSD (red line) and 750 nm converted with $\alpha_{525/1020}$ (magenta line) from collocated SCIAMACHY and SAGE II measurements. Shaded ares show standard error of the mean.

As it can be seen from Fig. 8.11, for all wavelengths the errors for the derived Ext are below ±25%, which is within the reported uncertainty of the Ext from SCIAMACHY. For Ext_{1020} the shape of the relative difference follows the one for r_{eff}, but with slightly different values (-20 to 10% for Ext_{1020} versus -40 to 0% for r_{eff}). Such behaviour is expected, because r_{eff} from SAGE II is obtained using the Ext_{1020} and Ext_{525} (see Sect. 2.4). The differences in the Ext_{525}, $Ext_{750}(PSD)$ and $Ext_{750}(\alpha_{525/1020})$ are rather constant with height, and vary from 15 to 25% for Ext_{525}, from 10 to 25% for $Ext_{750}(PSD)$ and from 0 to 15% for $Ext_{750}(\alpha_{525/1020})$. The discrepancy between two different ways of computing Ext_{750} derivation is quite remarkable, as with the consistent methods more consistent results are obtained. Though it should be highlighted once again, that for SAGE II 750 nm is not a measurement wavelength, and 525 nm is not considered in the SCIAMACHY retrieval. To explain the uncertainties coming from the different approaches to derive the Ext_{750}, in Fig. 8.12 the mean relative differences between $Ext_{750}(\alpha_{525/1020})$ and $Ext_{750}(PSD)$ for the whole SCIAMACHY dataset are depicted with a solid line, and ±1 the standard deviation is shown as the shaded area. From Fig. 8.12 it is clear that the calculation of the extinction coefficient with Ångström exponent results in about 8% negative bias. This result is consistent with the result presented in the supplements to Rieger et al. [2015]. Thus, it is important to consider this uncertainty when comparing the aerosol extinction coefficients from different instruments measuring at different

wavelengths.

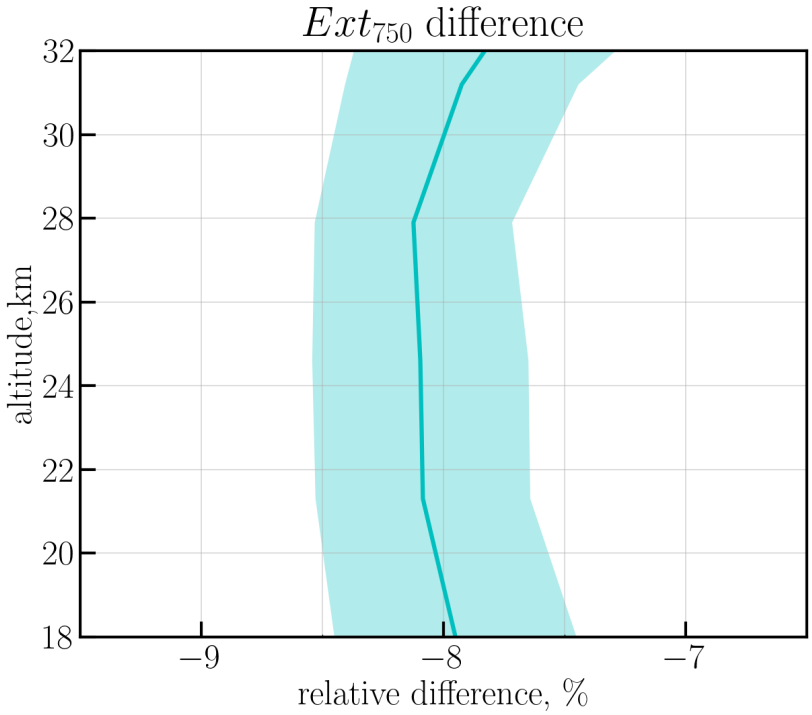

Figure 8.12. Mean relative difference between $Ext_{750}(PSD)$ obtained from PSD product with Eq. (1.5) and $Ext_{750}(\alpha_{525/1020})$ calculated using the Ångström exponent $((Ext_{750}(\alpha_{525/1020})\text{-}Ext_{750}(PSD))/Ext_{750}(PSD))$ from all available SCIAMACHY measurements. Shaded areas show ±1 standard deviation.

To extend the comparison to the data from SAGE II, $\alpha_{525/1020}$ ware calculated from its aerosol extinctions, and compared to the ones derived from SCIAMACHY PSD product. The mean relative differences between SCIAMACHY and SAGE II Ångström exponents are presented in Fig. 8.9 with the solid red line. The standard error of the mean is shown with the shaded area.

The relative difference between the Ångström exponents is altitude dependent, showing slightly different shape than Ext_{1020}. SCIAMACHY $\alpha_{525/1020}$ is about 40% higher than SAGE II at 18 km, about 20% higher between 21 and 28 km, and the difference at 31 km is around 10%. In the absolute values the difference varies from 0.8 at the lowermost altitude to 0.2 at the uppermost one. The bias in this comparison is expected. As it was discussed above, the differences between SCIAMACHY and SAGE II for Ext_{1020} and Ext_{525} are about 20%, but with the opposite sign. Thus, during $\alpha_{525/1020}$ recalculation they superpose resulting in larger differences. As for the r_{eff} and Ext_{1020} the reason, why the difference is altitude dependent is still under investigation.

8.4. Comparison with OSIRIS[1]

Although comparison of SCIAMACHY with SAGE II provides some information on the agreement of the products, this comparison is not sufficient to draw any robust conclusions. Additional information can be gained from the comparison with OSIRIS, which was operating at the same time as SCIAMACHY and also provides particle size information. Generally, comparison between SCIAMACHY and OSIRIS is more robust than with SAGE II, as both instruments employ the same measurement technique, use information at the same wavelengths (750 nm and 1530 nm), and provide a similar amount of measurements per orbit. Applying the same collocation criteria as for SAGE II, 4603 coincident profiles were found, which is about a half of the available SCIAMACHY profiles. The obtained amount of collocations is sufficient to ensure a reliable comparison. It is important to highlight once again that all the comparisons are done for the tropical region (20° N-20° S).

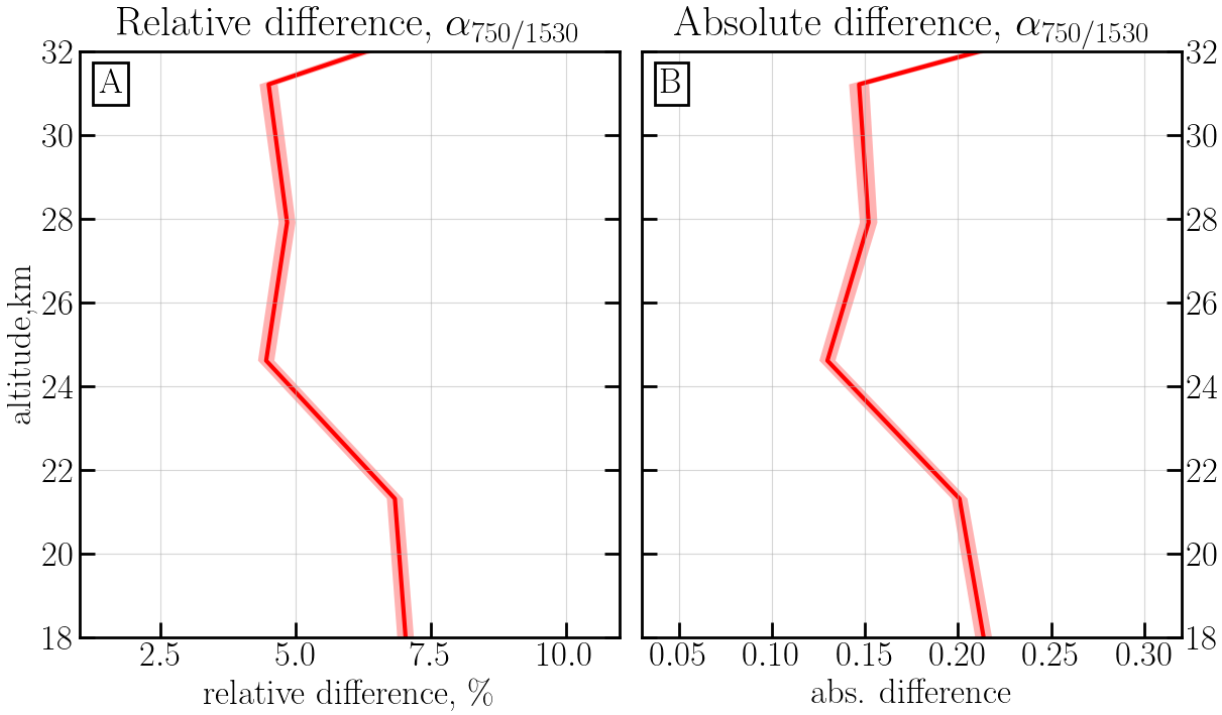

Figure 8.13. Mean relative (200×(SCIAMACHY-OSIRIS)/(SCIAMACHY+OSIRIS)) (panel A) and absolute (panel B) differences between Ångström exponents ($\alpha_{750/1530}$) from collocated SCIAMACHY and OSIRIS measurements. Shaded areas show standard error of the mean.

Differences between SCIAMACHY and OSIRIS $\alpha_{750/1530}$ are presented in Fig. 8.13. OSIRIS $\alpha_{750/1530}$ is interpolated onto the SCIAMACHY vertical grid. The difference in vertical resolution is not accounted for since SCIAMACHY and OSIRIS have similar specifications. In panel A of Fig. 8.13 the mean relative differences are plotted with a solid line, while in panel B the mean absolute differences are depicted. The standard error of the mean is shown by the shaded area. As follows from Fig. 8.13, the relative difference between SCIAMACHY and OSIRIS is about 7% for the lower altitudes and about 4% for

[1]This section was partially published in Malinina et al. [2018a].

the altitudes above 25 km. In absolute values the difference is about 0.2 below 25 km, and less than 0.15 at the higher altitudes. Taking into consideration the errors, estimated in Sec. 7.3.4, for the $\alpha_{750/1530}$ calculation from SCIAMACHY measurements (5%) and the errors reported by Rieger et al. [2014] for OSIRIS Ångström exponents (10%), it can be concluded, that the Ångström exponents obtained from both instruments agree well with difference being smaller than the reported errors.

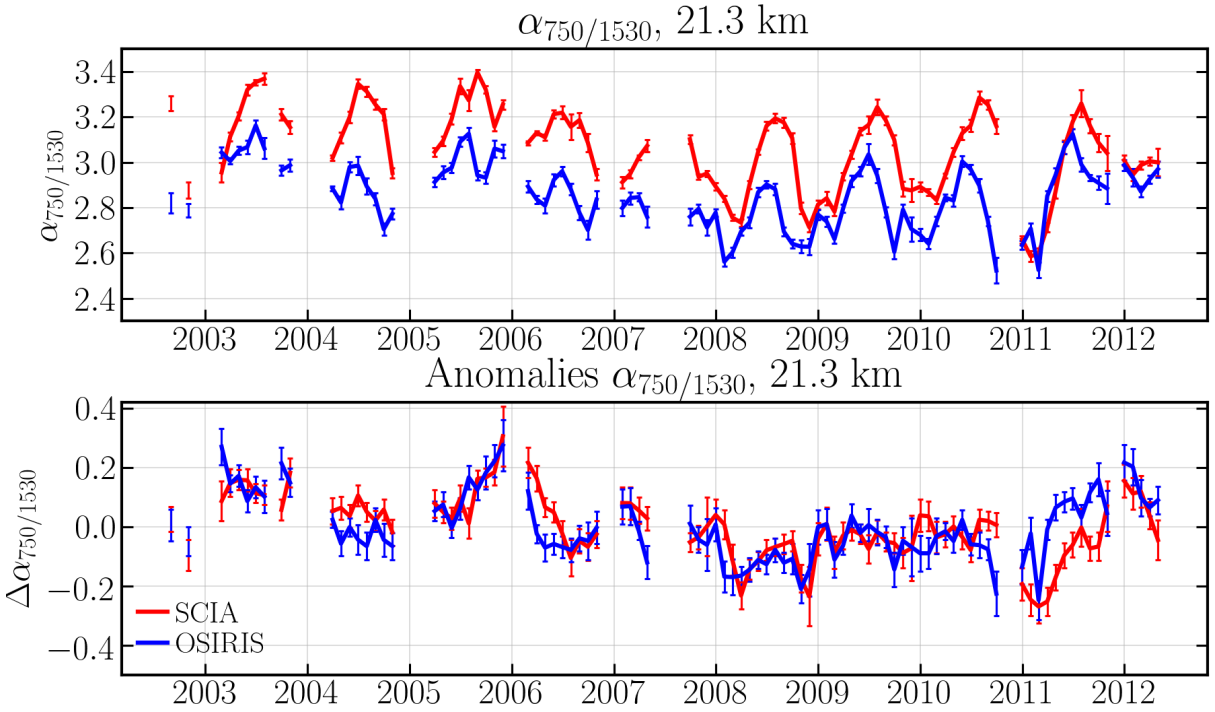

Figure 8.14. Zonal monthly mean (upper panel) and deseasonalized (lower panel) Ångström exponents ($\alpha_{750/1530}$) from collocated SCIAMACHY and OSIRIS measurements. Vertical bars show standard error of the mean.

To evaluate the temporal behaviour of the differences between SCIAMACHY and OSIRIS results the monthly zonal means of $\alpha_{750/1530}$ and its deseasonalized values (anomalies) at 21.3 km are plotted respectively in the upper and lower panels of Fig. 8.14. The deseasonalized values for each instrument are calculated individually using approach from Sec. 8.1. Months with less than 10 collocations are excluded from the comparison. SCIAMACHY data is presented in red and OSIRIS in blue, the vertical bars show the standard error of the monthly mean value.

As seen in the upper panel of Fig. 8.14, the Ångström exponents retrieved from both instruments show very similar behavior, although the absolute values of $\alpha_{750/1530}$ from SCIAMACHY are systematically higher than those from OSIRIS. A high degree of consistency is found between the results from both instruments in the comparison of the deseasonalized time series (see lower panel of Fig 8.14). Generally, the blue and red lines overlap or lie within the error bars following the same pattern, except at the beginning of 2006, when SCIAMACHY values are slightly higher, and 2011, when OSIRIS is slightly higher. However, even in those periods the differences are rather small (about 0.05–0.08). As the differences between Ångtröm exponents from both instruments are fairly constant with the time, and do not show signatures of any remarkable events (e.g. volcanic

eruptions), it can be concluded, that they originate most probably from the technical specifications of the instruments and differences in the retrieval algorithms.

8.5. Comparison with OPCs

As it was noticed in Sec. 1.6, balloon-borne OPCs provide aerosol PSD parameters in the period from 1971 until the time of writing, and it is planned to launch them in the future. Apart from occasional campaigns, most of the launches are made in Laramie, Wyoming (41.3° N, 103.6° W). Since SCIAMACHY PSD product was obtained for tropical region (20° N-20° S), there are no collocations between the products, and there is no possibility to compare the PSD profiles directly and provide quantitative assessments as it was done for SAGE II or OSIRIS. Another complication in comparison between SCIAMACHY and OPCs measurements is the difference in the assumptions on the shape of aerosol PSD. Thus, for SCIAMACHY retrievals the dn/dr function is considered to be unimodal in all cases, while in OPCs retrievals bimodal or unimodal distributions are fitted depending on the amount of independent concentration measurements [Deshler et al., 2003]. However, due to the BDC, it usually assumed that the stratospheric aerosol layer is generally well mixed around the globe, and PSDs even in the mid-latitudes regions do not change drastically from the tropical ones. For that reason it is possible to give a rough estimate on qualitative agreement between SCIAMACHY and OPCs.

To provide this comparison it was decided to look at the general relationship between σ and R_{mod} from both datasets. For SCIAMACHY all retrieved couples of parameters for the whole period (2002-2012) are considered at 21.3 km, for OPCs the parameters at 21.5 km are analyzed for the period from 1971 to 2015, including the measurements after major volcanic eruptions of Mount St. Helens in 1980 and Mount Pinatubo in 1991. The periods after those eruptions are not excluded from the comparison, because the launches of the OPCs are quite rare (from few a year til few a month) in comparison to the satellite measurements, and elimination of these periods significantly reduces the sampling. Additionally, just the fine mode of the bimodal PSD is taken into consideration, in case the bimodal distribution is fitted. That is justified by the fact, that usually, the coarse mode has much smaller N in comparison to the fine mode, even after Pinatubo eruption of 1991 [Deshler, 2008].

The relationship between σ and R_{mod} is presented in Fig. 8.15. In panel A SCIAMACHY data is depicted, in panel B the measurements from OPCs are shown, and in the panel C the datasets are presented together with SCIAMACHY data being slightly transparent. Color coded is Ext at 750 nm, calculated for SCIAMACHY with the method described in 7.3.3, and for OPCs Ext_{750} is calculated considering the PSD being unimodal and using provided in the dataset fine mode N.

In Fig. 8.15 it is clearly seen, that both SCIAMACHY and OPCs datasets have similar relationship between R_{mod} and σ, and Ext_{750} is generally distributed over the parameter grid in a similar way. The OPCs point cloud is scattered wider than the SCIAMACHY one, which is a result of the different time periods and the number of modes. Nevertheless

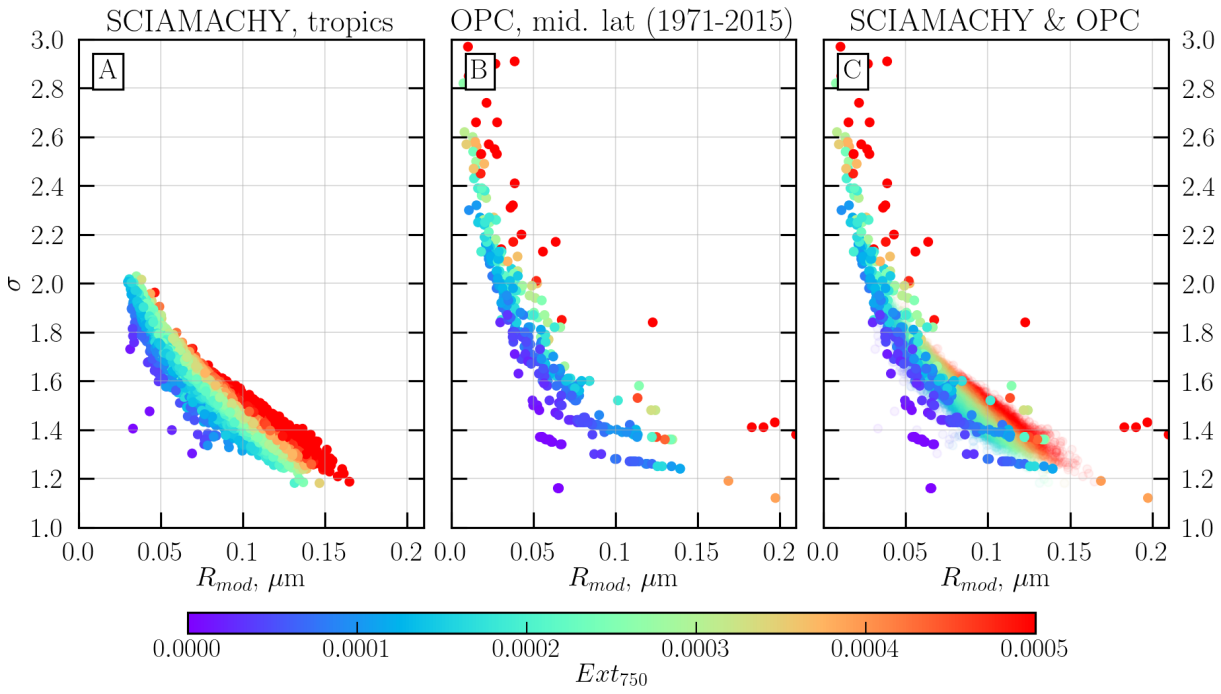

Figure 8.15. Relation between σ and R_{mod} from SCIAMACHY (panel A), OPCs (panel B) and from both of them (panel C) at 21.5 km.

the curvatures of the presented point clouds are roughly the same, which is even more distinct after looking at the datasets depicted at the same plot (panel C). It is obvious, that both data clouds, even having slightly different scattering, compliment each other creating one homogeneous cloud. However, it should be noted, that the relationship between the R_{mod} and σ could not be used as a constraint in SCIAMACHY retrieval to obtain the third parameter of the PSD. This is because the thickness of the cloud is reaching up to 0.5 of σ, which corresponds to up to 0.06 μm difference in terms of w, which is comparable to the span of this parameter after a big volcanic eruption. Thus, inclusion of the correlation of R_{mod} and σ into the retrieval algorithm will result in more significant errors in the PSD parameters than those coming from the fixed N profile.

Summarizing Sect. 8.5 it should noted, that qualitatively both SCIAMACHY and OPCs aerosol PSD datasets agree well, however, to provide a more reliable comparison of the data, SCIAMACHY retrieval should be extended to the other latitude bins. More details on the possible future studies are provided in Sect. 10.2.

Part IV.

Case studies

9 Case studies

In this chapter, the volcanic eruptions, as well as an exceptional biomass burning event (Canadian Wildfires of 2017), are discussed. The events are arranged chronologically, starting with Manam and Tavurvur eruptions, for which both, *Ext* and PSD, datasets are available (Sec. 9.1). In the following sections (9.2–9.4) only *Ext* was analyzed.

9.1. Manam and Tavurvur eruptions

In order to compare the eruptions of Manam and Tavurvur, they are analyzed in this section together, even though they occurred with over a year time lag. As both eruptions occurred during the SCIAMACHY lifetime in the tropical region, there is a possibility to analyze not only the changes in *Ext*, but also in PSD parameters.

First, on 28 January 2005, Manam, located in Papua New Guinea (4.1° S, 145.0° E), erupted. The event was classified with VEI 4; however, the information on the amount and altitude of the released SO_2 differs between the different sources. Smithsonian Institution [2017] considers 140 kt of SO_2 to be released to 24 km altitude, while Bingen et al. [2017] report 144 kt of SO_2 at 18 km. At this point, it should be noted, that volcanic eruption databases are quite contradicting for certain events. That is because the information about the eruptions is coming from the different estimates, which are based on the data from different instruments employing different techniques and retrievals. For example, Bingen et al. [2017] database uses data from GOMOS and MIPAS, using the information on SO_2 from the later one (algorithm description is presented in Höpfner et al. [2015]). The Smithsonian Institution [2017] uses data from nadir observations of Ozone Monitoring Instrument (OMI) and OMPS, which is known to be not very precise [Li et al., 2017]. In the particular situation of Manam eruption, the values presented by Bingen et al. [2017] seem to be more reasonable.

Tavurvur (in some sources Rabaul) eruption occurred on 7 October 2006 in Papua New Guinea (4.3° S, 152.2° E) and released 300 kt of SO_2 to 18 km altitude according to Smithsonian Institution [2017]. A VEIindex of 4 was attributed to this eruption. Some

months before, the stratovolcano Soufriere Hills in West Indian territories of United Kingdom (16.7° N, 62.2° W) erupted. This event dated 20 May 2006 received VEI 3. The Smithsonian Institution [2017] reports 200 kt of SO_2 reaching the altitude of 20 km.

9.1.1. Aerosol extinction coefficient

In order to provide a deeper analysis, not only monthly mean values but also 10-days averaged Ext have been analyzed. The monthly mean values of Ext_{750} within a year after the Manam eruption are presented in Fig. 9.1 and within 12 months around eruptions of Soufriere Hills and Tavurvur in Fig. 9.4. The 10-day averaged Ext_{750} for the period from January 2005 until late 2006 are shown in Fig. 9.3 at 18.4, 21.7 and 25 km altitudes.

First, the monthly mean Ext, presented in Fig. 9.1, is analyzed. As several years before Manam eruption were volcanically quiescent, the Ext state in January 2005 is clearly background. However, already in February 2005 a notable increase in Ext near the equator is observed at the altitudes below 21 km. In March the area of increased Ext becomes larger. As in the previous month, it is located in the tropics at the altitudes below 21 km. In April 2005 the tropical plume weakens and moves higher up. At the same, time the Ext values in the Northern Hemisphere slightly increase. In May and June 2005 the absolute values of the Ext are smaller than in the previous months, but in the tropics, the volcanically perturbed region is extended in the altitude. In the mid and polar latitudes, Ext is somewhat higher in the Northern Hemisphere. In July, August and September 2005 tropical plume is isolated at about 22 km, and it starts to expand along the latitudes. In the extra-tropical regions of the Northern Hemisphere, the Ext values are again larger. The increase in Ext at the lowermost altitudes of the polar region of the Southern Hemisphere is most likely an artifact, related to the presence of PSCs. In October the enhanced region expands slightly along the latitudes, and at the lower altitudes, there is an increase of Ext in the mid-latitudes of the Northern Hemisphere. In the last two months of 2005, the increase in Ext reaches 25 km altitude, weakening in the strength in the lower altitudes and moving slightly towards the Northern Hemisphere, the increase in the latitudes to the North from 30° N is more pronounced.

The transport of the stratospheric aerosol can be demonstrated through the age of air analysis. According to Engel et al. [2009], the mean age of air is the average time needed to transport an air parcel from its entry point in the stratosphere, the tropical tropopause, to a given location in the stratosphere. It is often used as an indicator of the strength of the residual circulation. The general rule is, the younger mean age of air is in a certain location, more active circulation is at this location. In Fig. 9.2 monthly mean age of air from TOMCAT/SLIMCAT model [Chipperfield, 2006] is presented for each month of 2005 for the same altitudes and latitudes as in Fig. 9.1. In January 2005 the age of air is distributed more or less symmetrical with respect to the equator. Central rod is slightly shifted to the Northern Hemisphere. At the altitudes above 20 km, the air is somewhat younger in the Northern Hemisphere. In February the pattern remains similar, while the central rod shifts towards the equator in the lower altitudes. In March and April, the tilt of the central rod is more distinctive, and the air in the Northern Hemisphere is younger, which is a sign of more active circulation there. This is a reason why in April Ext is slightly

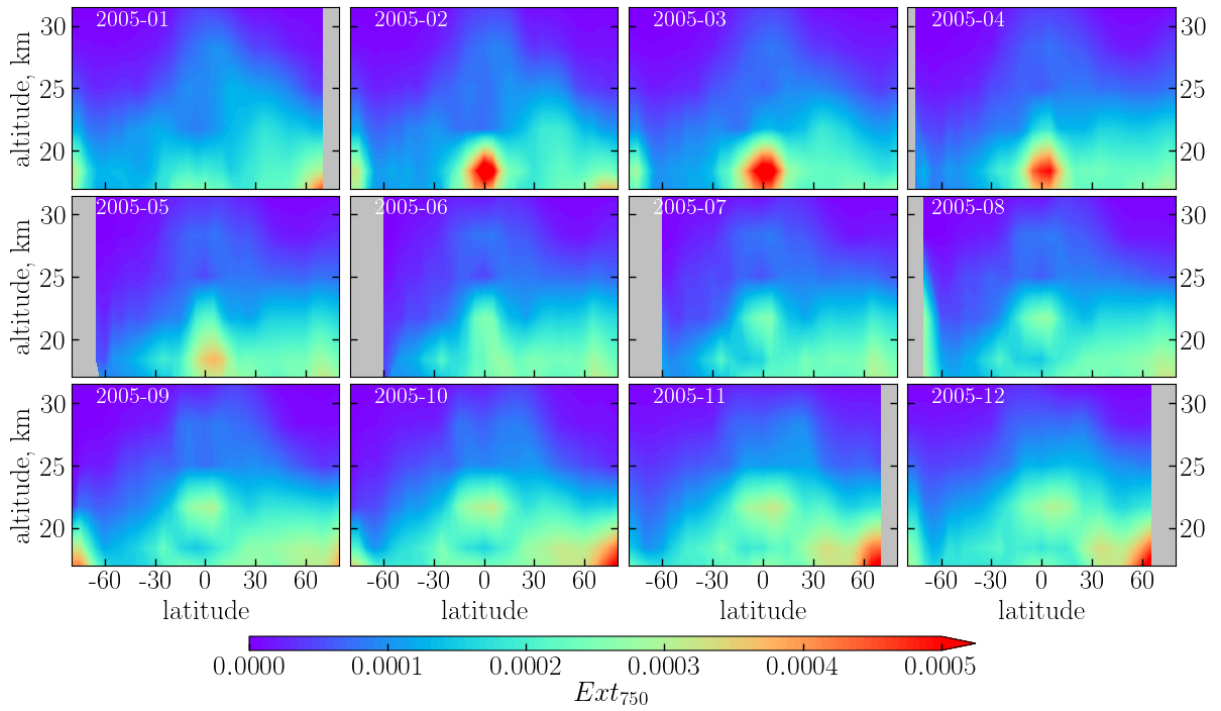

Figure 9.1. Evolution of the Ext_{750} with the time within a year after Manam eruption, based on the monthly mean V1.4 SCIAMACHY *Ext* data.

higher in the Northern Hemisphere, than in the Southern. From May until August the general pattern of the age of air remains almost the same with slightly broadened central rod and active circulation in the Northern Hemisphere. This circulation is responsible for the uplift of the aerosol plume and slightly increased Ext_{750} in the North. In September the pattern starts to get more symmetrical with respect to the equator. There is older air in the high altitudes of the Northern Hemisphere with the central rod being tilted. In the last three month of 2005, the pattern gets more symmetrical: the central rod is broad and slightly shifted towards the Northern Hemisphere with air at the lower altitudes being slightly younger than in the South. This defines the aerosol plume in those months: it becomes more spread along the latitudes with *Ext* being distinctively higher in the Northern Hemisphere.

Looking at the altitudinal distributions, presented in Fig. 9.3, it seems that the aerosol from Manam reaches 18.4 km 20 days after the eruption. This is in a good agreement with the eruption altitude provided by Bingen et al. [2017]. The data for the first 20 days after the eruption are missing, so it is impossible to estimate the behavior of *Ext* there. The enhanced *Ext* remains in the intratropical region in this altitude until the beginning of summer 2005. Interestingly, the *Ext* in the Northern Hemisphere is somewhat higher than that in the Southern Hemisphere during the whole time since the beginning of 2005. There is an additional increase in late 2005 – early 2006 in the mid-latitudes, which is a result of the volcanic aerosol transport with the BDC. At 21.7 km the *Ext* increases by March 2005 in the tropics and remains increased until early 2006. The plume starts to move towards the higher latitudes of Northern Hemisphere in November 2005. Volcanic perturbation reaches 25 km in late 2005, stays in the tropical region and is eventually superposed with the perturbation from eruptions of Soufriere Hills and Tavurvur, occurred in 2006. For

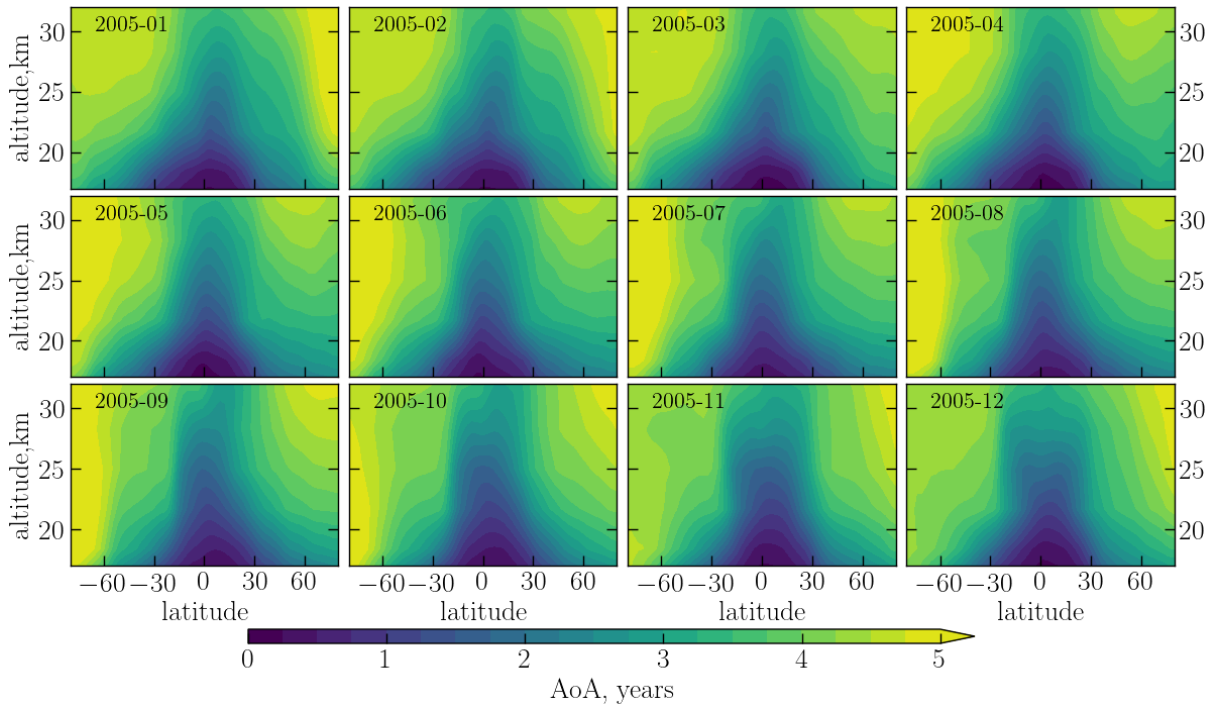

Figure 9.2. Evolution of the age of air with the time within a year after Manam eruption, based on the monthly mean TOMCAT/SLIMCAT data

that reason, the *Ext* remains increased at this altitude until the end of 2007.

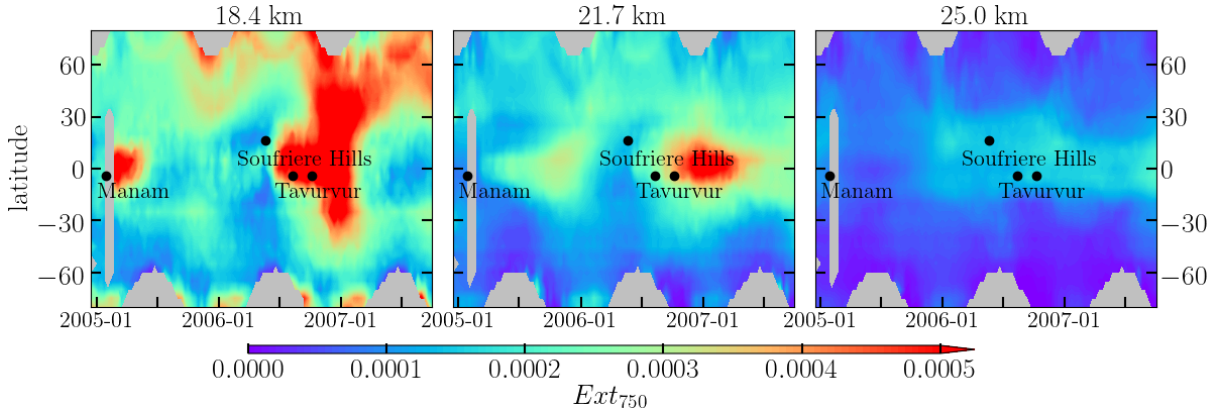

Figure 9.3. Evolution of the Ext_{750} at different altitudes during Manam and Tavurvur eruptions, based on the 10-day averaged V1.4 SCIAMACHY *Ext* data.

After Soufriere Hills and Tavurvur eruptions, the evolution of *Ext* was different. Based on the monthly mean distributions, depicted in Fig. 9.4, it can be stated that in May 2005, when Soufriere Hills erupted, the stratosphere was not in a completely background state, as it was for Manam. The remaining small enhancements in *Ext* from Manam eruption are seen at the altitudes about 25 km as well as in the lowest altitudes in the polar region of Northern Hemisphere. In June 2006, after the eruption of Soufriere Hills, there is a small increase in *Ext* around the equator in the altitude region from 18 to 21 km. The increase in the polar region is weaker than in the previous month. In July and August 2006 the volcanic plume grows around the equator. In September 2006 tropical

area of increased Ext area extends further. There is also a slight increase in the Northern Hemisphere extending along the latitude. The area of the enhanced Ext in the polar region of Southern Hemisphere is related to PSCs. In October 2006, the month of Tavurvur eruption, tropical plume continues to grow. At the same time, the Ext increases even more in the Northern Hemisphere at around 18 km. In November the aerosol expands further, reaching its maximal propagation in December 2006. In the tropical region the plume is located at the altitudes below 25 km, and Ext is increased in the lowermost altitudes of the Northern Hemisphere. In the Southern Hemisphere the plume propagates up to 40° S. In January 2007 Ext starts to decrease, and in February the lowermost altitudes have much less aerosol than a month before. This month the plume is located at around 21 km at the equator. In the Southern Hemisphere, there is a slight increase in Ext at 18 km at the latitudes below 40° S, while in the Northern Hemisphere there is a substantial amount of aerosol in the mid and polar latitudes. Later, in March 2007 Ext decreases everywhere, reaching its minimal state in April.

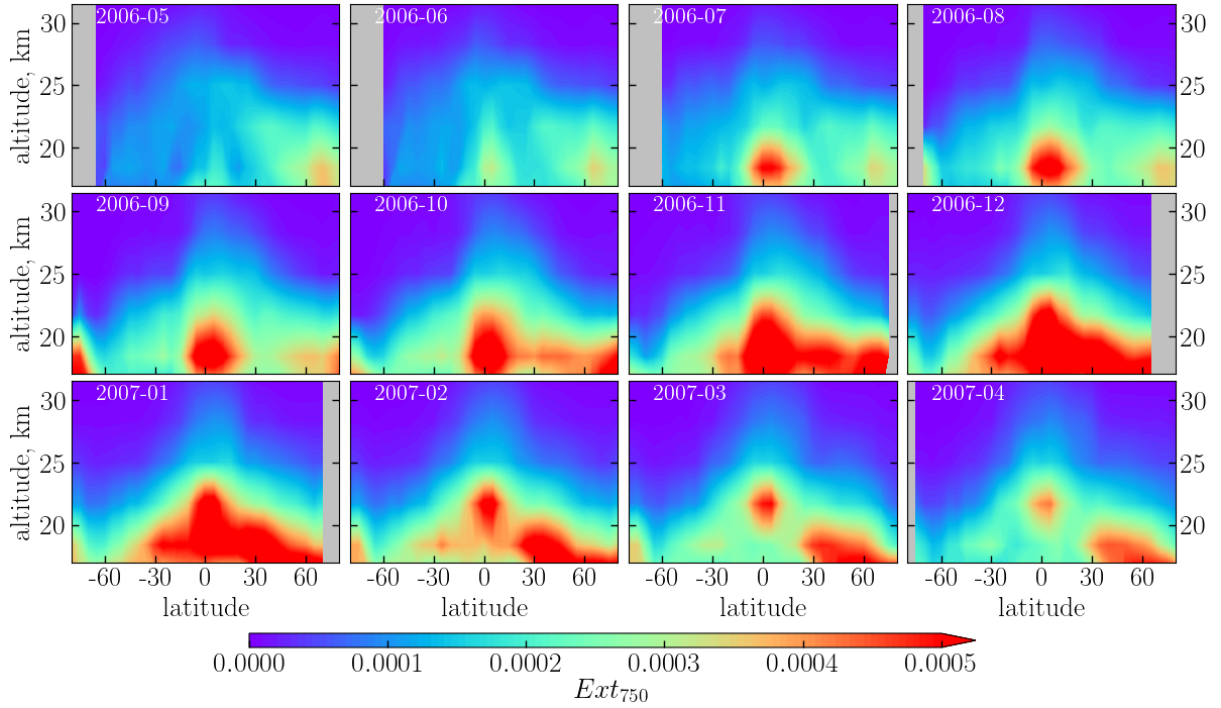

Figure 9.4. Evolution of the Ext_{750} with the time within a year after Soufriere Hills and Tavurvur eruptions, based on the monthly mean V1.4 SCIAMACHY Ext data.

As for Manam, the age of air pattern was analyzed in order to determine aerosol transport. The monthly mean age of air from TOMCAT/SLIMCAT model is shown in Fig. 9.5 for the same time, latitudes and altitudes as in Fig. 9.4. In May 2006, the age of air is distinctively younger in the Northern Hemisphere; moreover, there are two central rods in the tropical region: one of them is located in the Northern Hemisphere and is tilted towards the South at the upper altitudes. The secondary rod is centered in the tropics of the Southern Hemisphere but reaches only the altitudes of about 23 km. This pattern defines the longer lifetime of the Manam plume in the Northern polar regions. In June 2006 the secondary central rod starts to disappear, and the main rod gets wider, being still tilted. The circulation in the Northern Hemisphere is remarkably strong, which results in lower values

of the age of air. In July, August and September 2006 the age of air has similar patterns with the central rod being broad and air in the Northern Hemisphere to be younger. This circulation pattern is the reason, why the aerosol from Soufriere Hills eruption is located in the tropics, gets broader with the time and moves primarily to the North. In October 2006 the age of air pattern becomes more symmetrical. However, the northbound circulation is still more active. That is why the aerosol from Soufriere Hills and newly formed aerosol from Tavurvur eruption propagate towards the North. In November and December 2006 the central rod gets narrower, is straight and is located slightly to the North from the equator. The circulation starts changing, and the air at the lower altitudes of the Southern Hemisphere gets younger. More active circulation is responsible for the aerosol movement towards the mid-latitudes of the Southern Hemisphere. In the first three months of 2007 the circulation is active in the Southern Hemisphere at the lower altitudes, and in April it gets more symmetrical. However, at the time the plumes start to disappear.

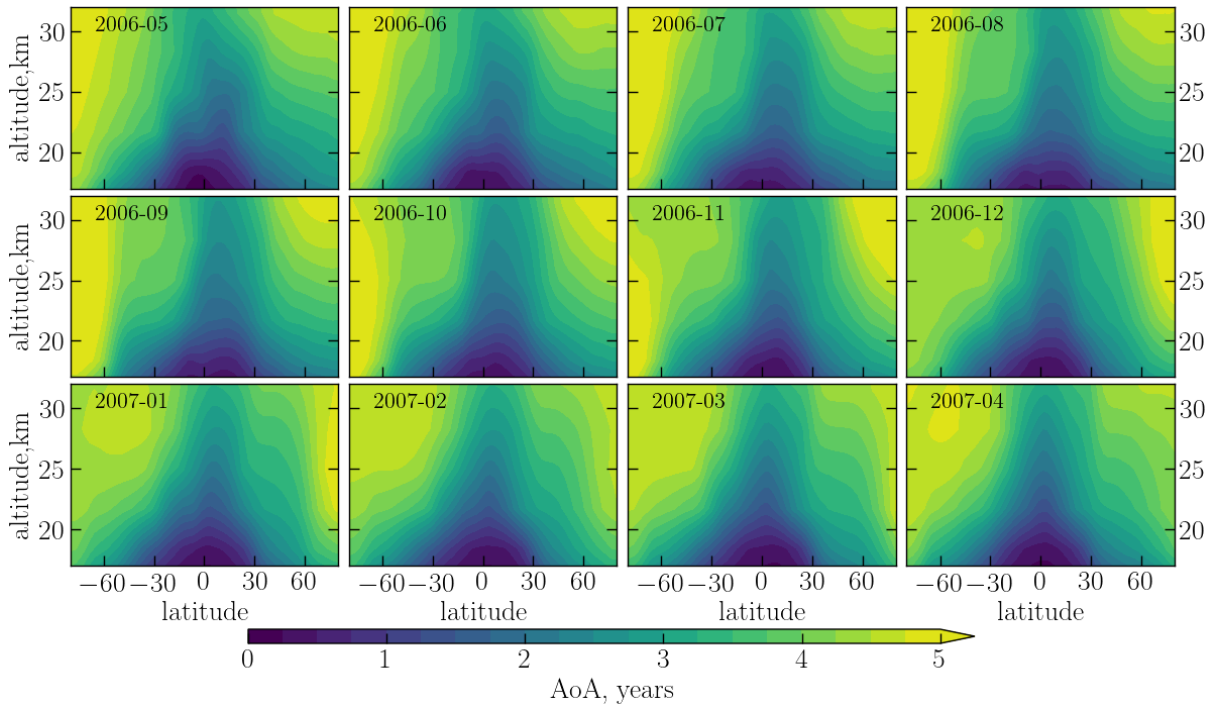

Figure 9.5. Evolution of the age of air within a year during Soufriere Hills and Tavurvur eruptions, based on the monthly mean TOMCAT/SLIMCAT data.

The analysis of the *Ext* evolution with time and latitude, presented in Fig. 9.3, shows that the increase in *Ext* after Soufriere Hills reached the 18.4 km altitude in the first weeks after the eruption. The plume has a tendency to move towards south, staying however within the tropical region. After the eruption of Tavurvur, the plume continues to propagate towards both, north and south. In the Northern Hemisphere volcanic plume tends to live longer, until late 2007 in the latitudes above 40° N. In the Southern Hemisphere it does not seem to move above 40° S, and the volcanic aerosol remains there until early 2007. At 21.7 km the *Ext* increase right after Soufriere Hills eruption is rather small, the perturbation reaches this altitude by the time of Tavurvur eruption. It is hard to distinguish which plume, from Tavurvur or the transported with convection plume from

Soufriere Hills caused the observed increase. Anyway, Ext is increased in the tropics until the late 2007, not moving to other latitude regions. At 25 km it is even more complicated to track which volcano was responsible for the increase in Ext. That is because in the tropics the increase initially caused by Manam was superposed with perturbations from Soufriere Hills and Tavurvur eruptions.

9.1.2. PSD

In this section, the temporal evolution of the aerosol PSD at 18, 22 and 25 km altitudes after the Manam and Tavurvur eruptions is considered in more detail. The analysis was done using the profiles retrieved from the individual measurements. The resulting distributions are presented in Fig. 9.6. The distributions in the Manam series are plotted in the left column and for Tavurvur in the right column. As in Eq. (1.1), N is a multiplicative factor of $\frac{dn}{dr}$, N=1 cm^{-3} was used for each altitude to make Fig. 9.6 more descriptive. In each panel of Fig. 9.6 four distributions corresponding to different time lags before and after the eruptions obtained at similar latitudes ($\pm 2^{\circ}$) are presented. There are four time slots chosen: before the eruption (green lines), in the first months after the eruption (red lines), in about half a year (blue lines) and a year after the eruption (cyan lines). The exact dates corresponding to the curves are presented in the legend below the panels.

As mentioned above, the Manam eruption was characterized by an increase of R_{mod}, but almost no change of w after the eruption in comparison to the background conditions. This can be easily seen from the depicted distributions. At 18 km (upper left panel in Fig. 9.6) in the first months after the eruption (red line) the peak of the distribution shifts to the larger radii in comparison to the distribution before the eruption (green line). After around seven months after the eruption (blue line) distribution shifts back to smaller values, but its peak is still located at a distinctively larger radius value than that for the background distribution. At the end of March 2006, 14 months after the eruption (cyan line), the atmosphere at this altitude is "relaxed" and returns to a state close to that before the eruption, albeit with a slightly larger R_{mod}. This can be related to a weaker eruption of Manam at the end of February - beginning of March 2006 (see the database of Smithsonian Institution [2017] or Bingen et al. [2017]). It is interesting to mention that w after the eruption (red, blue and cyan lines) does not seem to change much in comparison to that of background conditions (green line), but it is obvious that the distribution before the eruption (green line) has a distinctively stronger relative contribution of larger particles than the one after the eruption. The distributions at 22 km (middle left panel in Fig. 9.6) before and shortly after the eruption look similar, with the perturbation to the PSD shape being observed 7 and 14 months after the eruption (blue and cyan lines). These time delays are attributed to the vertical transport velocity. For the same reason, the 25 km altitude (lower left panel in Fig. 9.6) distributions before the eruption, as well as two and seven months after the eruption are similar to each other, but the one 14 months after the eruption is shifted to larger radii. For all distributions, there is no noticeable change observed for w.

The temporal evolution of the aerosol PSD after the Tavurvur eruption showed a different behavior than that after Manam. At the lowermost retrieved altitude (18 km, upper right

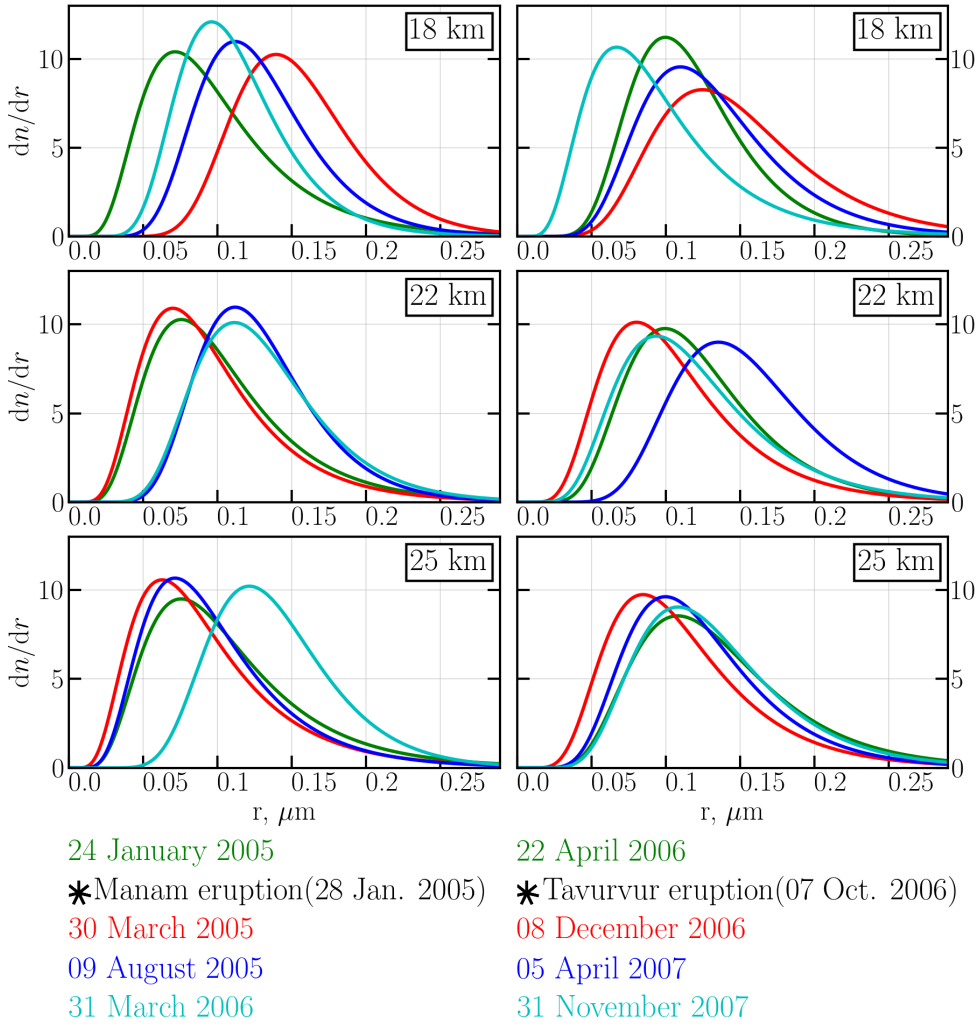

Figure 9.6. Evolution of the aerosol particle size distribution at different altitudes (18, 22, 25 km) after the Manam (left panels) and Tavuvur (right panels) eruptions.

panel) aerosol PSD shifts to the larger R_{mod} and gets remarkably wider shortly after the eruption (red line). It appears that the stratospheric aerosol formed after the Tavurvur eruption superposed with the one after the weaker Soufriere Hills eruption, which occurred several months before. Although the Soufriere Hills eruption might have influenced the observed distributions, it is not possible to distinguish between these two eruptions due to worse sampling in comparison to the V1.4 *Ext* product, and therefore in this section, they are considered as one event. About six months after the event, the distribution shifts to the smaller R_{mod} and gets narrower. Similar to the evolution after the Manam eruption, after about a year (cyan line) the distribution returns almost to the same shape as before the eruption (green line). The shape of the PSD is similar to one before the Manam, indicating, that stratosphere returned to the background state. At 22 km (middle right panel of Fig. 9.6) the distribution responds as expected with the time lag of around half a year, and at 25 km the changes are most likely dominated by other processes and not significant in general.

In a qualitative level, the changes in the PSD after both eruptions agree very well with

the Ext changes presented in Sec. 9.1.1. The increase in PSD parameters leads to the increase in Ext, the response is not linear, but is unambiguous in comparison to Ångtsröm exponent changes (see Sec. 8.2). Thus, after Manam eruption, when only R_{mod} increases, Ext increases weaker than after Tavurvur eruption, which results in the increase of both PSD parameters. For the future, when a better constraint of N parameter will be implemented (see Sec. 10.2), there will be a possibility to compare the SCIAMACHY V1.4 Ext and PSD products and evaluate the agreement quantitatively.

9.2. Sarychev Peak eruption

Sarychev Peak (or Sarychev) is an active volcano, located in Kuril Islands (48.1° N, 153.2° E). Even though Sarychev erupts continuously, the eruption on 15 June 2009 is important for the stratospheric aerosol community. This is because with this eruption the largest amount of SO_2 over the period from 2002 to 2012 was emitted [Smithsonian Institution, 2017, Bingen et al., 2017]. According to Smithsonian Institution [2017], 1200 kt of SO_2 were released directly in the stratosphere, at 17 km altitude. Bingen et al. [2017] report almost three times smaller amount of SO_2 to reach the stratosphere (480 kt at 16 km), but the scale of the eruption is still more substantial than the others over the SCIAMACHY operation period. To analyze the Ext behavior after the Sarychev eruption, two types of data were considered. First, the monthly mean Ext_{750} from SCIAMACHY V1.4 is presented for each month from June 2009 until May 2010 as a function of latitude and altitude in Fig. 9.7. Second, the 10-day averaged Ext_{750} is presented at 18.4, 21.7 and 25.0 km altitudes as a function of time and latitude in Fig. 9.8.

As it follows from Fig. 9.7, only a slight increase of Ext in the high latitudes of Northern Hemisphere (north to 60°) at around 17–20 km is seen in June 2009. This enhancement, however, is most likely associated with Redoubt eruption occurred earlier that year (see Fig. 5.1). As the SO_2 is converted to H_2SO_4 with an e-folding time of 1 month, the observed increase in the aerosol extinction coefficient cannot be attributed to the Sarychev eruption. A month later (July) a slight increase in Ext at the Northern mid-latitudes (from 20 to 60° N) below 20 km is identified. In July and August 2009 this increase becomes much stronger, reaches the altitude of 21 km and spreads all over Northern hemisphere. In October 2009 the volcanic plume reaches it maximal extension over latitude and altitude, and then it starts to decrease from November 2009. In the tropics, the area of the increased Ext starts to move up, with a maximum being located at around 18-19 km. In April 2010 aerosol extinction coefficient reaches the conditions close to initial.

Looking at the 10-day average Ext at different altitudes in Fig. 9.8, the propagation of the volcanic plume can be analyzed more precisely. At 18.4 km Ext increases within about 30 days after the eruption next to the volcano, and from there the aerosol spreads towards the equator and poles. The enhancement in the aerosols lasts at that altitude relatively long, up to the first half of 2010. Interestingly, at 21.7 km the increase after the eruption appears at the same time as at 18.4 km; however, aerosol seems to be transported with the time only towards the equator. The 25 km altitude is affected the least from the

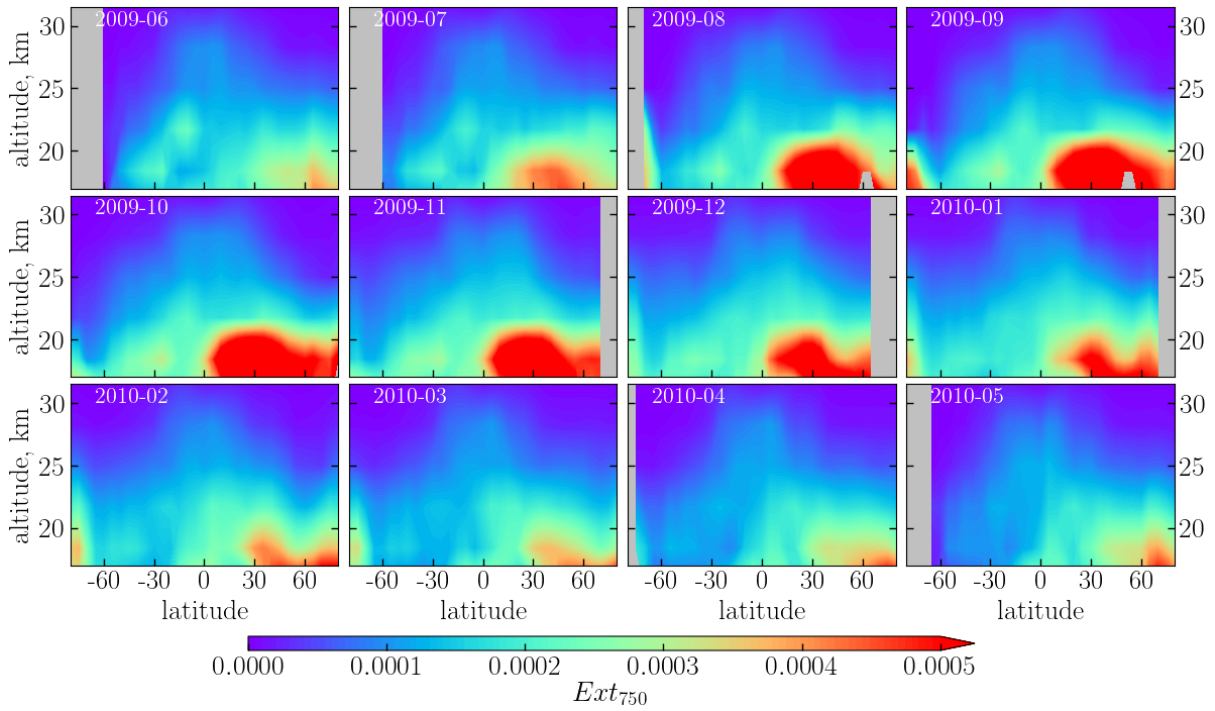

Figure 9.7. Evolution of the Ext_{750} with the time within a year after Sarychev eruption, based on the monthly mean V1.4 SCIAMACHY *Ext* data.

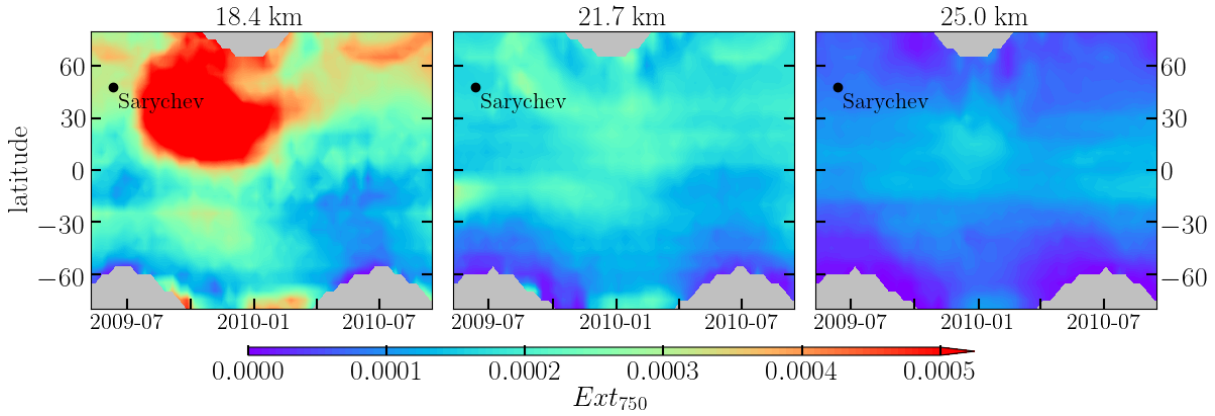

Figure 9.8. Evolution of Ext_{750} at different altitudes after Sarychev eruption, based on the 10-day averaged V1.4 SCIAMACHY *Ext* data.

eruption. There is only a small increase in tropics around 20-30° N about a half a year later after the eruption.

As BDC, the main mechanism of the stratospheric transport, implies the upward motion in the tropics, poleward motion in the mid-latitudes and downward motion in the poles, one expects, that the stratospheric aerosols and related to it *Ext* increase move mainly polewards. Since the observed propagation differs from theoretically predicted one, it is decided to analyze the distribution of *Ext* after the eruption over the globe. The 10-day averaged *Ext* at 18.4 km is presented as a function of latitude and longitude within three months after the eruption in Fig. 9.9. The date in the left upper corner of each map shows the start date of the 10-day period used for averaging. It is seen that in the

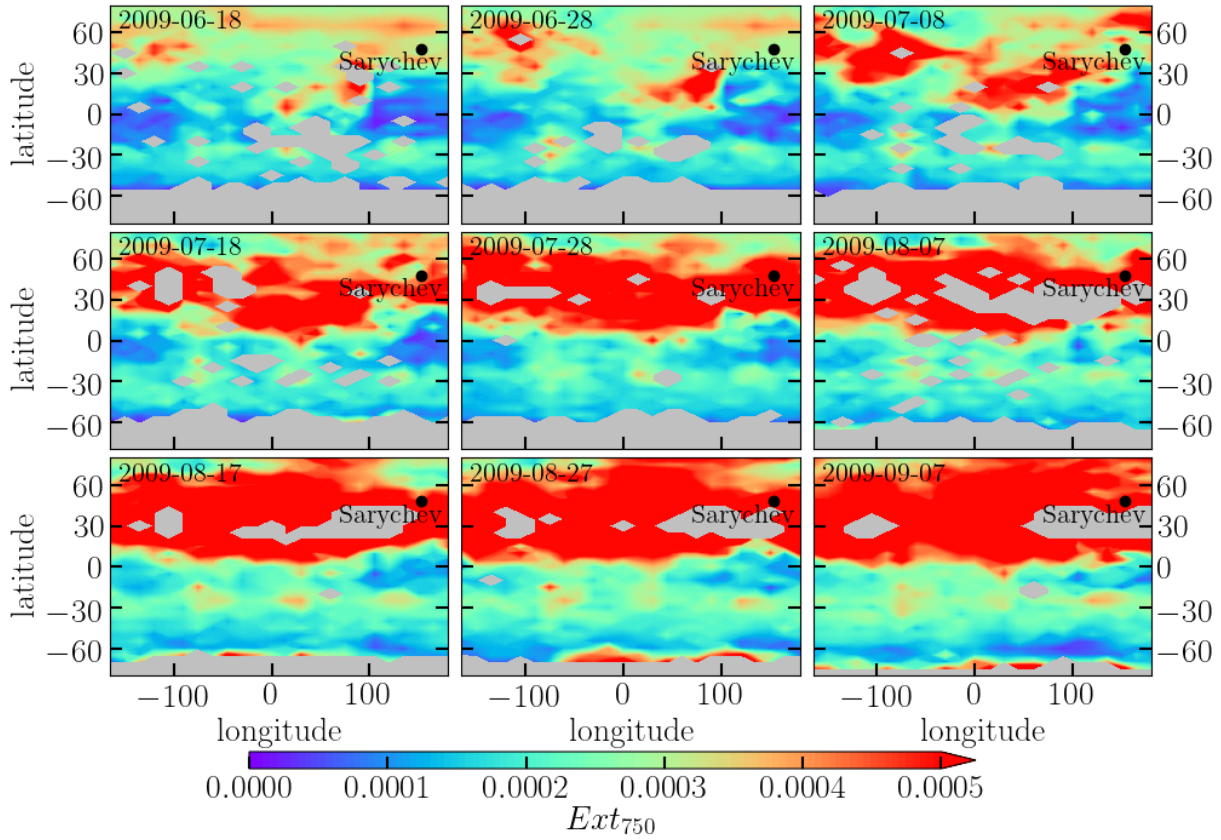

Figure 9.9. Evolution of Ext_{750} at 18.4 km after Sarychev eruption, based on the 10-day averaged V1.4 SCIAMACHY *Ext* data.

first 10-day period the volcanic plume slowly starts to move along the 60° N latitude covering all longitudes. A small increase is also seen in the tropical region of the Eastern Hemisphere. This increase is linked to the Asian Monsoon anticyclone. Thus, the aerosols related to the eruption were captured on the eastern side of the anticyclone and isolated by it. Similar pathways were reported for other trace gases by Park et al. [2007]. Ten days later the increase in the mid-latitudes of Western Hemisphere is clearly observed, and the increase in the Monsoon region becomes stronger. In the first days of August 2009, the regions of the enhanced *Ext* grow creating a pathway from the Northern mid-latitudes of the Western Hemisphere towards the Eastern tropics. Later the volcanic plume spreads all around the Northern Hemisphere. Very similar results were reported by Kravitz et al. [2011], who presented the results of the Sarychev eruption simulation and compared them to OSIRIS and lidar data. Even though the results from the model are not in quite a perfect agreement with OSIRIS, the authors emphasized, that they trusted measured *Ext*. SCIAMACHY *Ext* data presented here agrees with OSIRIS results published in Kravitz et al. [2011]. The authors of the manuscript do not explain the way stratospheric aerosols spread around the globe, only state the fact. Most likely such transport is associated not only with BDC but also with the QBO phase at the time of the eruption and the Asian Monsoon. Thus, the fact that eruption occurred by the time, when Asian anticyclone was formed, resulted in the pathway from the location of the eruption to the Eastern tropics, and later the secondary meridional circulation spread the aerosols all over the tropics.

At the end of this section, it is important to mention the grey area below 18 km from about 45 to 65° N in August and September 2009 in Fig. 9.7 and several grey spots in Fig. 9.9, which result from improper cloud filtering. As it was noticed in Sec. 4.1 and 5.1.1, all values above 0.001 km^{-1} are considered to be cloud contaminated. This cloud filtering threshold seems to be too low. Since Sarychev eruption released a large amount of SO_2 directly into the stratosphere, a larger specific amount of stratospheric aerosol was formed in comparison to the other eruptions of the period. This lead to higher than the cloud threshold values of *Ext* next to the altitude of the injection. It should be noted that at the altitudes next to the tropopause, especially during the volcanic eruption it is hard to distinguish between the volcanic plume and cloud. To make the cloud filtering appropriate, each scan needs to be individually analyzed. It should be noted, that by the time of the work on *Ext* algorithm the existing cloud filtering algorithm by Eichmann et al. [2016] was known to have the disadvantage to tag the increased *Ext* as clouds. That was a motivation to choose the *Ext* threshold for cloud filtering instead; however, it resulted in the same issue. Since then Liebing [2016] developed a new cloud filtering algorithm, based on the statistical approach. This algorithm is expected to be more suitable to use for *Ext* retrievals. The implementation of this filtering is planned for the future (see Sec. 10.2).

9.3. Kelut eruption

The exceptionality of Kelut eruption is the height of *Ext* perturbations. To analyze the evolution of the volcanic plume, as for the previous eruptions, the monthly mean, as well as 10-day averaged, *Ext* values are used. Kelut erupted during the OMPS lifetime; thus, Ext_{869} from V1.0.9 is considered. The monthly mean values as a function of latitude and altitude within a year after the eruption are presented in Fig. 9.10 and 10-day averaged values are depicted in Fig.9.12 as a function of latitude and time at 18.5, 20.5, 22.5 and 24.5 km altitude.

Kelut, located in Indonesia (7.9° S, 112.3° E) erupted on 13 February 2014, releasing 200 kt of SO_2 at 19 km altitude (VEI 4). It should be noted, that some months later, on 30 May 2014, another Indonesian volcano, Sangeang Api (8.2° S, 119.1° E) released 100 kt of SO_2 to 17 km altitude (VEI 3) [Smithsonian Institution, 2017]. Those eruptions are very well tracked in Fig. 9.10. In February 2014 the stratospheric aerosols are in the background state. In March there is an obvious increase of *Ext* at the equator from 17 to about 21 km altitude. In April *Ext* increases even stronger around the equator with some plume "tail" moving down to the lower altitudes of the Southern Hemisphere mid-latitudes. This enhancement is even more intensified in May with plume at the equator moving higher up. At the end of May, Sangeang Api erupted, which lead to the additional increase of *Ext* in the lower altitudes of the Southern Hemisphere and lifting of the equator plume to the altitudes of about 23 km in June 2014. In July, August and September the *Ext* in Southern Hemisphere starts returning to the background state with the equator plume to move higher up in the altitude reaching about 24 km. Later, in October and November 2014 the equatorial plume starts to expand over the latitudes with *Ext* in the mid-latitudes of the Northern Hemisphere starting to increase. By December 2014 the

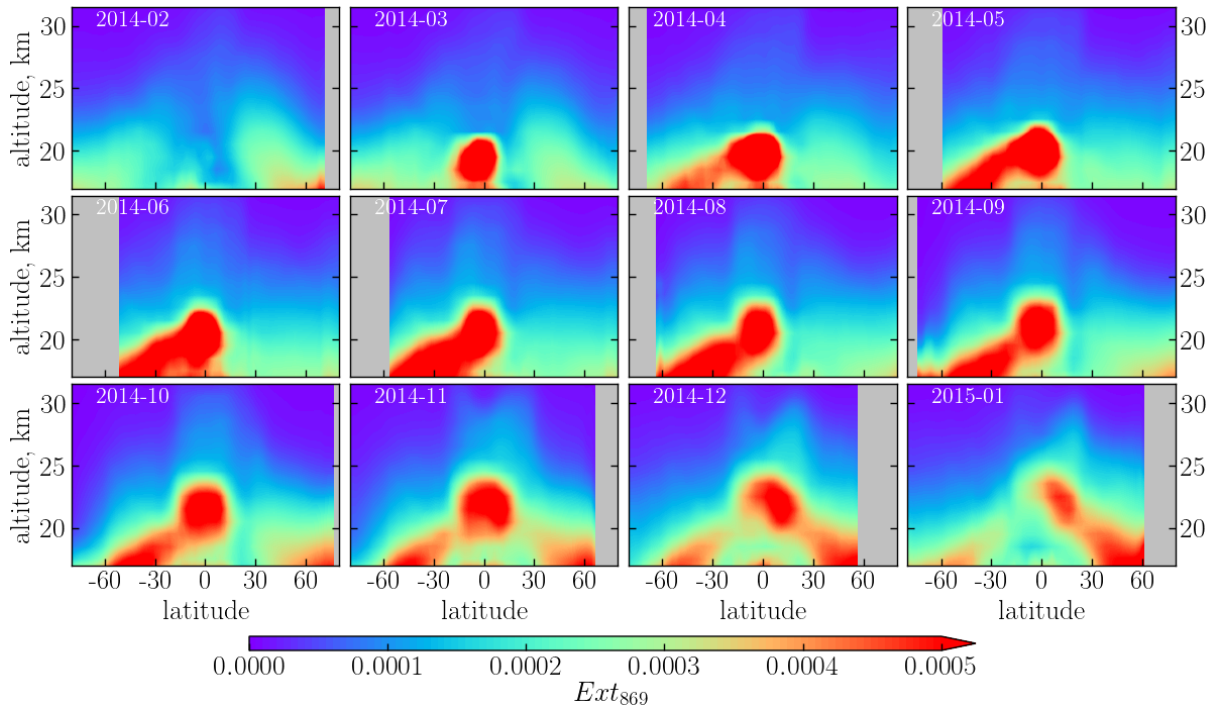

Figure 9.10. Evolution of the Ext_{869} with the time within a year after Kelut eruption, based on the monthly mean IUP V1.0.9 OMPS *Ext* data.

equatorial plume drifts to the Northern Hemisphere tropics. At the same time, the *Ext* increases in the Northern mid-latitudes and decreases in the Southern. In January 2015 the enhancements start to relax towards the background state.

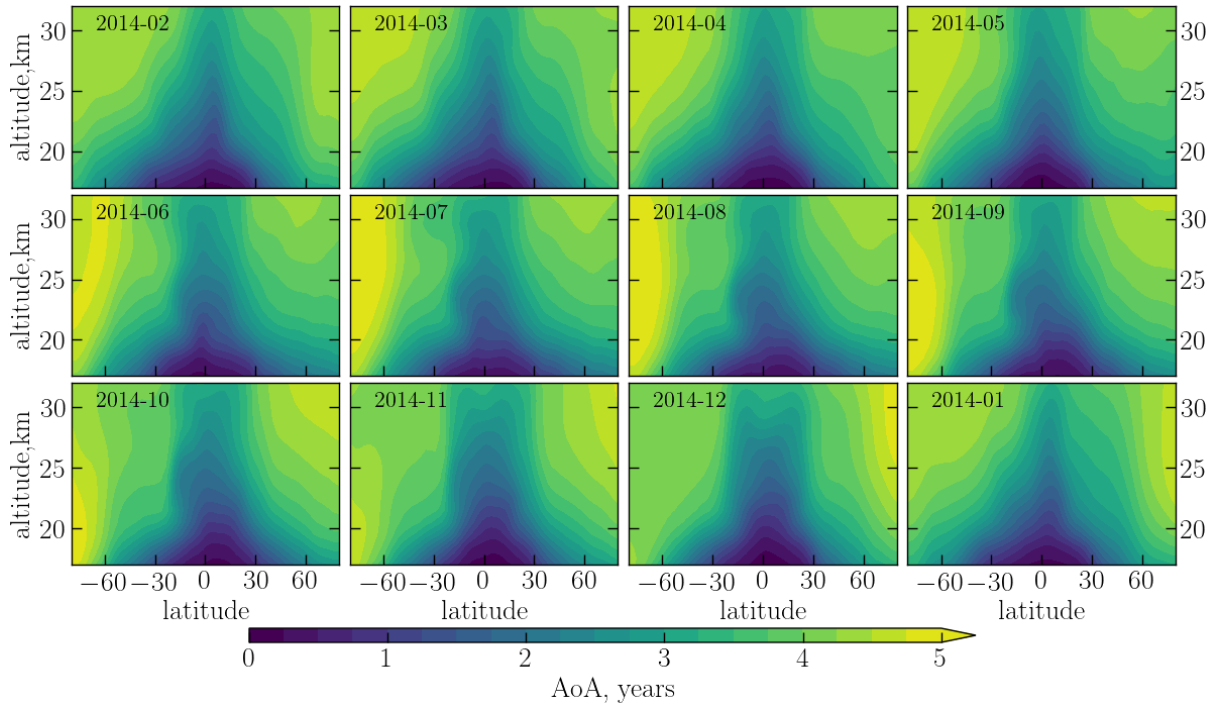

Figure 9.11. Evolution of the age of air with the time within a year after Kelut eruption, based on the monthly mean TOMCAT/SLIMCAT data.

Such a particular plume movement is a result of the BDC, in particular, its shallow branch. Since Kelut erupted in the tropical region, the SO_2 and the developed aerosols were lifted higher up with the time (March – September 2014). Additionally, the shallow branch of the BDC, which is stronger in the winter hemisphere, moved the aerosols towards the South pole in the period from April to September 2014, resulting in the *Ext* enhancement in those regions. The eruption of Sangeang Api in late May 2014 reinforced the plume over the equator, resulting in a longer lifetime of the aerosol enhancement, and its propagation higher up in the altitude (July to September 2014). In October 2014, when the shallow branch of the BDC started to intensify the Northern hemisphere, where the winter was about to come, *Ext* started to increase there. The larger *Ext* increase was observed at the northern latitudes later in the winter (November 2014 – January 2015). Basically, the tropical region was acting like an aerosol reservoir, and BDC was transporting this aerosol towards the hemisphere, where the BDC was stronger.

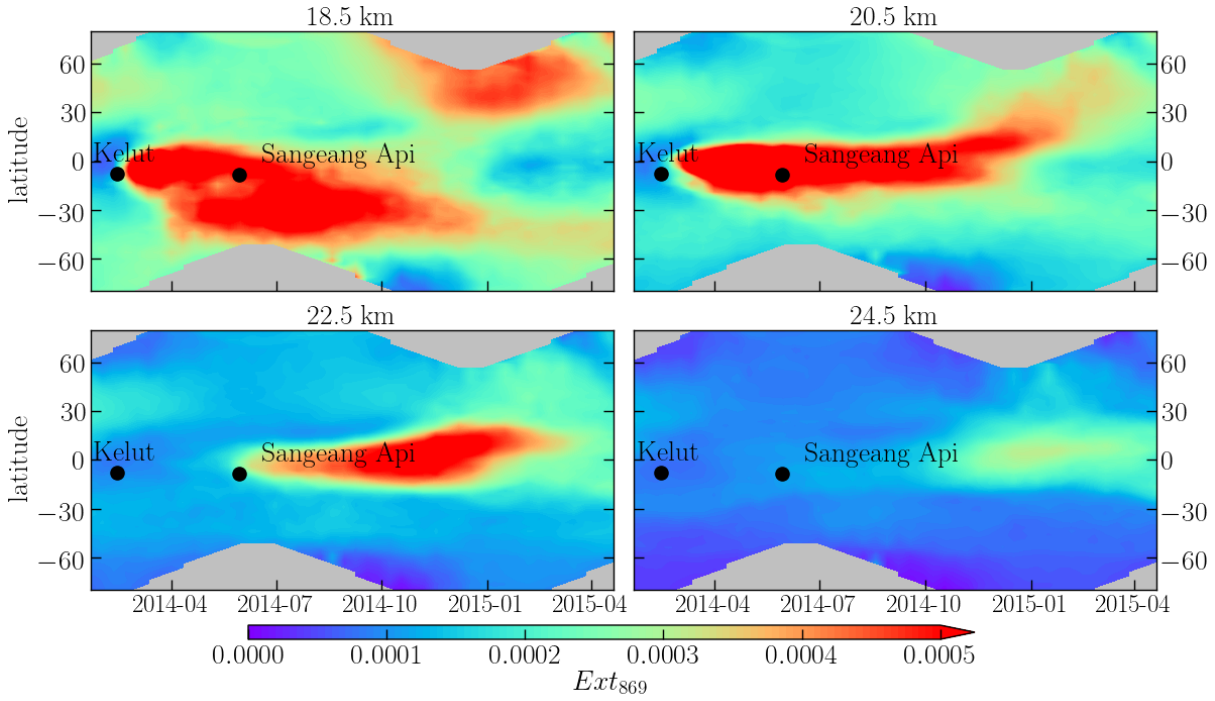

Figure 9.12. Evolution of the Ext_{869} at different altitudes during Kelut eruptions, based on the 10-day averaged IUP V1.0.9 OMPS *Ext* data.

The connection of the aerosol transportation with the BDC is additionally illustrated by the age of air analysis. To demonstrate the circulation patterns at the time of Kelut eruption, monthly mean age of air from TOMCAT/SLIMCAT model is presented in Fig. 9.11 for the same latitudes, altitudes and time as in Fig. 9.10. It is seen, that in February and March 2014 age of air at the lower altitudes of the Southern Hemisphere is slightly younger than in the Northern Hemisphere. The central rod in these months is slightly shifted to the Northern Hemisphere. In April 2014 the central rod is located closer to the equator, with younger air situated again at the lower altitudes of the Southern Hemisphere. This pattern explains the observed in these months propagation of the volcanically induced aerosols towards the South Pole. In May 2014 the age of air becomes more or less symmetrical with respect to the equator. In July the central pattern shifts to

the Southern Hemisphere, becoming more tilted with the height. In July and August, the central rod was slightly tilted towards the south, which explains, why the Ext plume was located mainly in the Southern Hemisphere. In September 2014 the central rod becomes broader, and the younger air prevails at the lower altitudes of the Northern Hemisphere. This results in the Ext plume to be redistributed more symmetrically with respect to the equator, as well as in a slight increase of Ext over the polar latitudes of the Northern Hemisphere. The shift of the circulation in October 2014 towards the North Pole (the younger air at the lower altitudes is located again in the Northern Hemisphere) is responsible for the propagation of the volcanic plume there. In November and December 2014 the plume migrates towards the Northern hemisphere, where the air is younger, and the circulation is stronger. In January 2015 the conditions become more similar to those in February 2014. Though the perturbation from volcano is relaxing.

The movement of stratospheric aerosols with the shallow branch of the BDC is as well seen on the example of the 10-day averaged Ext_{869}, presented in Fig. 9.12. Ext increases at 18.5 km right after the eruption, as a result of not only SO_2 but also significant ash release at that altitude [Vernier et al., 2016]. The plume is additionally fortified after the Sangeang Api eruption, moving towards the southern hemisphere with the time and weakening in the beginning of 2015. The altitude of 20.5 km the plume reaches some weeks later after the eruption. It is also interesting that at that altitude the plume was keeping its position in the tropics for over half a year until late 2014, when it started to move towards the north, leading to the Ext increase in the northern mid-latitudes, which lasted up to early 2015. The aerosol perturbation from Kelut eruption reaches 22.5 km approximately in early June 2014 with plume being increased late 2014 after Sangeang Api eruption. The plume at this altitude is moving towards the north, however not as strong, as the lower altitudes. The increase of Ext_{869} after both eruptions reaches 24.5 km in late 2014 and lasted until early 2015, when Ext starts to decrease again. This increase is noticeable in the tropical region of the Northern Hemisphere (0 – 30° N). A delayed increase of Ext at higher altitudes represents the tape-recorder effect mentioned in Sec. 5.2. After Kelut eruption it was especially strong, because of two reasons. First, the volcano is located in the tropics, where the upward movement, related to the BDC is quite steady. Second, the increase is intensified after Sangeang Api eruption which happens to be located very close to Kelut. It should be additionally noticed, that generally, the aerosol propagation after a tropical eruption is rather predictable in case the data on stratospheric circulation is provided. As it was seen of all the tropical eruptions (Manam, Tavurvur and Kelut), the movement of the aerosols and the Ext increase is quite straightforward in respect to monthly mean stratospheric age of air values.

9.4. Canadian Wildfires

For the analysis of the extra-tropical enhanced Ext event during the OMPS lifetime, it is decided to look at the Canadian Wildfires of 2017. These fires were quite significant, and the Aerosol Index during this event was reported to be the highest during the satellite observation era [Khaykin et al., 2018, & references therein]. Additionally, Ansmann et al. [2018] noticed, that the aerosol optical depth over Central Europe reached the value even

higher than after Pinatubo eruption. The increase of Ext after those fires lasted as long as after a moderate volcanic eruption (see Sec. 5.2), making it scientifically attractive.

The Wildfires started on 6 July 2017 and lasted until late September. The starting point was located at about 51.7° N, 121.3° W with 900 000 ha of forest burned down. By the end of 2017 it was considered to be the worst British Columbia Wildfires; however, 2018 might overcome that record (by the time of writing the Wildfires of 2018 were still active).

For the plume evolution study, in Fig. 9.13 the monthly mean Ext are presented within 8 months after the start of the Wildfires as a function of latitude and altitude. The 10-day averaged Ext_{869} behavior with time and latitude is presented at 18.5, 20.5 and 22.5 km in Fig. 9.14. It is decided to look at the lower altitudes than the ones used in the Kelut analysis, because the wildfires Ext enhancement did not reach as high altitudes as volcanic eruptions. The lower altitudes are not considered, because they are rather cloud contaminated.

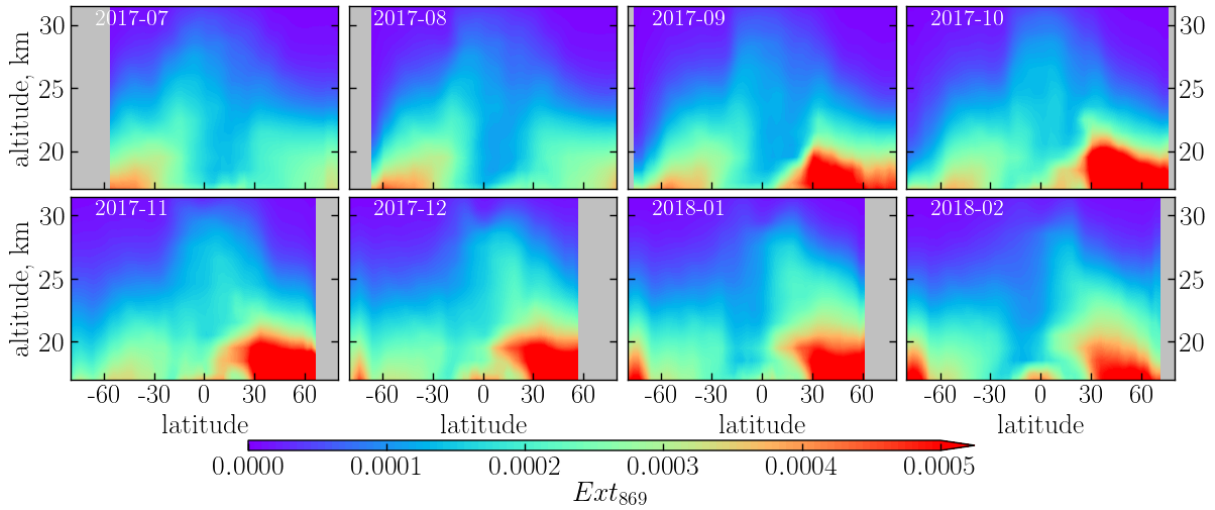

Figure 9.13. Evolution of the Ext_{869} with the time within 8 months after Canadian Wildfires, based on the monthly mean IUP V1.0.9 OMPS Ext data.

The monthly mean Ext_{869}, presented in Fig. 9.13, shows that in July 2017, right after the start of the fires, the Ext in the Northern hemisphere is still in the background condition. In August it seems to increase slightly, but not high enough to track the difference. In September, however, the perturbations reach altitudes up to about 20 km and spread over mid-latitudes of the Northern Hemisphere. Ext also slightly increases in the tropical region of the Northern Hemisphere. In October, the plume reaches its most abundant extension spreading north from 30° N at the altitudes below 22 km. In November the plume starts to decrease, which continues until February 2018. All that time, the plume has an anvil shape, covering the region below 21 km in the tropics and having a slight increase in Ext at about 20 km in the tropics. The slight perturbations from the fires reach altitudes of about 25 km in December 2017 and January 2018, starting to disappear in February.

The plume development is distinctively seen in Fig. 9.14. The perturbations from the fires reach 18.5 km altitude at the beginning of September 2017 and last at that altitude until

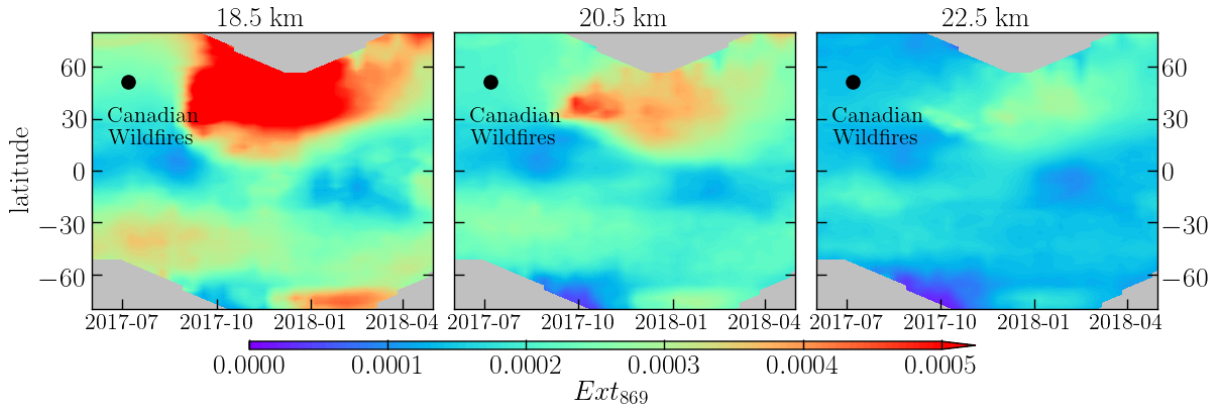

Figure 9.14. Evolution of the Ext_{869} at different altitudes during Canadian Wildfires, based on the 10-day averaged IUP V1.0.9 OMPS *Ext* data.

early 2018, starting to decrease by that time. Mostly, the plume stays the whole time within the mid-latitudes Northern Hemisphere, expanding to the tropics in a light manner, unlike e.g. Sarychev eruption, which spread down to the equator. The plume reaches 20.5 km altitude approximately at the same time as 18.5 km; however, the enhancement is not that high. The plume lifetime at that altitude is approximately the same as 18.5 km. The *Ext* at the altitude of 22.5 km is perturbed by the fires significantly later (from October 2017 to April 2018). Generally, these results agree with those from Ansmann et al. [2018], Khaykin et al. [2018].

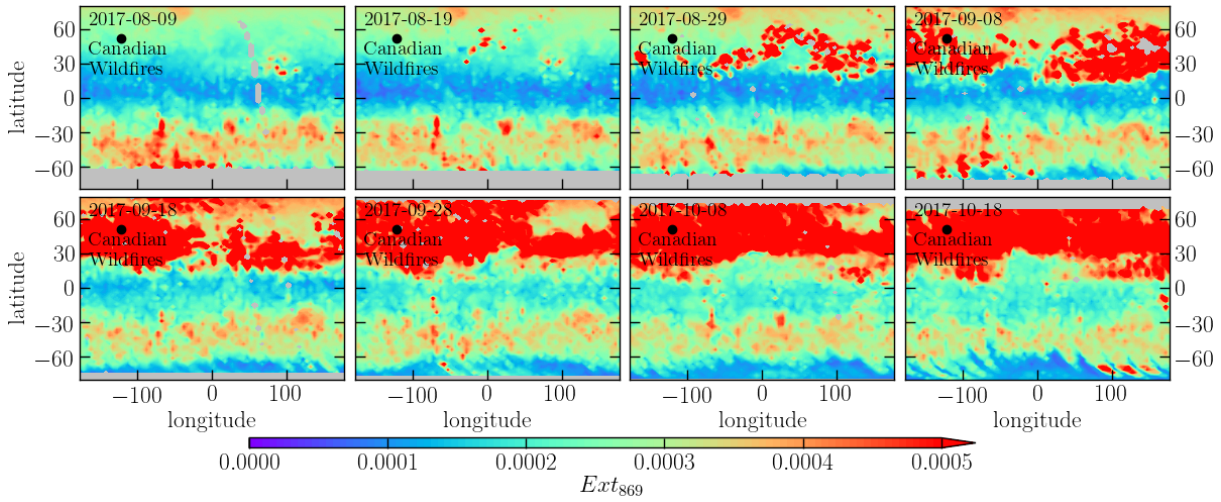

Figure 9.15. Evolution of the Ext_{869} at 18.5 km during Canadian Wildfires, based on the 10-day averaged IUP V1.0.9 OMPS *Ext* data.

In order to track that slight tropical increase in *Ext*, as for Sarychev eruption the 10-day averaged Ext_{869} values are presented in Fig. 9.15 as a function of latitude and longitude. As the perturbation from the Wildfires has not reached stratosphere momentarily, it is decided to start the analysis in early August 2017. Thus, for the period ending on 9 August 2017, *Ext* in the Northern Hemisphere is more or less in the background condition. The only exception is a small region the tropics of the Eastern Hemisphere. This enhancement is related to Asian Monsoon Anticyclone (the mechanism is described in

Sec. 1.3 and Randel et al. [2010]). For the next 10 days, Ext pattern in the Northern Hemisphere remains almost the same, except the mid-latitudes over the 170° W. Most likely, these are the first signs of the Wildfires plume, which are more obvious in the next 10-day period. It is also well seen, that as in case of Sarychev the aerosols are captured by Asian Monsoon and in then transported all over the globe. However, in comparison to Sarychev, the increase in the tropics does not last long and does not propagate below 15° N. Most likely, this is due to the smaller aerosol amount reached the stratosphere during the Wildfires.

Here it should be noted, that the extra-tropical enhanced aerosol loading events differ from the tropical ones. While the perturbation from the tropical Kelut eruption spread all over the globe within a year, the perturbations from extra-tropical events tend to stay in the Hemisphere, where they occurred. As it was explained earlier, the cause for that is stratospheric transport, in particular, BDC. This is one of the reasons, why the tape-recorder effect after the tropical volcanic eruptions is more pronounced. With the rising air in the tropics the aerosols reach higher altitudes within some time. In the northern latitudes, the upward movements are not as common. Canadian Wildfires, however, are not the conventional extra-tropical case study. The smoke from the fires reached the stratosphere within a PyroCb cloud, which is an extreme form of convection [Fromm et al., 2010]. Nevertheless, PyroCbs are responsible for the transport of the aerosols precursors to the stratosphere not significantly affecting the transport within the stratosphere.

Another remark is related to the retrieval of Ext during the Wildfires. The problem is that during biomass burning events not only sulphuric compounds are released into the stratosphere, but also a large amount of soot, whose physical parameterization (e.g. form, distribution, content) differs from the droplets of H_2SO_4. Therefore during the forward modeling and retrieval, additional uncertainties are introduced. For this reason, additional studies on whether the current assumptions on stratospheric aerosol composition are representative during biomass burning events should be done.

10

Conclusions and outlook

10.1. Conclusions

In the thesis, the retrieval algorithms developed to obtain stratospheric aerosol parameters, as well as the resulting products, were discussed. The actual work was split into three parts: the first one covers the aerosol extinction coefficient (Ext) retrievals from limb-scatter instruments and challenges related to them. In the second part, retrieval of the aerosol particle size distribution (PSD) parameters from SCIAMACHY limb measurements and related problems were discussed. Case studies analyzing several volcanic eruptions were presented in the last, third, part.

Aerosol extinction coefficient

In the first part, Ext retrieval algorithms from SCIAMACHY and OMPS measurements are presented. In comparison to the previously published V1.1, I updated SCIAMACHY V1.4 Ext retrieval algorithm dropping the shorter wavelength normalization. The developed product contains Ext at 750 nm, which is retrieved simultaneously with the albedo. I compared the obtained product to SAGE II and OSIRIS. Both comparisons show good results in the tropics (differences below 20%) with higher discrepancies in the polar regions. According to my studies, those discrepancies are related to the fixed aerosol PSD parameters assumption used for the limb-viewing instruments. I demonstrated that for limb instruments the changes in the assumed PSD result in more than 100% changes in the retrieved Ext in the polar regions of both hemispheres. I as well adopted the V1.4 Ext algorithm to OMPS measurements. However, due to a coarser spectral resolution, Ext is retrieved at 869 nm. The OMPS product needs further improvements and lacks validation, but it can already be used in the evaluation of volcanic activity or biomass burning events. Generally, the analysis of the global Ext databases from both, SCIAMACHY and OMPS, shows the increase in Ext after volcanic eruptions, as well as tape-recorder effects after some of them.

Aerosol particle size distribution

In the framework of the thesis, I developed a retrieval algorithm to obtain two parameters of the stratospheric aerosol PSD (R_{mod} and σ) from SCIAMACHY limb measurements. In this retrieval, a fixed vertical distribution of the aerosol N is assumed, and N is not retrieved. Wavelength dependent surface albedo is included in the retrieval. The algorithm uses the measurements of the scattered light at seven wavelengths and normalization to the extraterrestrial solar irradiance. My investigation of the averaging kernels showed good sensitivity in the altitude range from 18 to 32 km for both retrieved parameters.

From the investigation of the sensitivity of limb-scatter and solar occultation instruments to the aerosol particles of different size, I concluded that limb-scatter instruments are sensitive to the aerosol particles of smaller size, and thus, provide more accurate PSD information than solar occultation instruments, in particular, during periods with low aerosol loading. In contrast, occultation instruments provide Exts which are associated with smaller uncertainties than the ones from the limb instruments.

I assessed the errors in the obtained (R_{mod}, σ) and recalculated (w, Ext and Ångström exponents) parameters using the synthetic retrievals. For the scenarios with unperturbed N, the errors typically are about 5–10%, while for the perturbed N, the errors increase to 10–30% depending on the parameter. The only exception is the Ångström exponent, whose maximal errors are 5% even for the perturbed cases.

I applied the developed retrieval algorithm to SCIAMACHY measurements, and generated the first, and for now, unique dataset of two PSD parameters from an instrument measuring scattered light in the limb viewing geometry. My analysis of the retrieval results demonstrates an increase of R_{mod} in the altitude range from 18 to 25 km after volcanic eruptions, while w does not show any distinct behavior (can increase, decrease or remain unchanged). Tape-recorder effect or a delayed response of the aerosol parameters to the volcanic eruptions for higher altitudes is observed for both, R_{mod} and w. Additionally, I analyzed the Ångström exponent obtained from the Ext values, which I recalculated from PSD dataset. I have seen that the Ångström exponent can either increase, decrease or remain unchanged after a volcanic eruption. My analysis showed that changes in $\alpha_{750/1530}$ are driven by changes in both R_{mod} and w (or r_{med} and σ), and an infinite number of pairs of these parameters provides the same value of $\alpha_{750/1530}$. Thus, I concluded, that it is impossible to derive any reliable information on the changes in the aerosol size based solely on the Ångström exponent for one wavelength pair. This can only be done if at least one of the PSD parameters is provided in addition.

In order to validate the product, I compared the retrieval results to the SAGE II data. This comparison shows an agreement within 30% for effective radii in the lower altitudes, getting better with increasing altitude to better than 10% above 25 km. For all altitudes, there is a systematic negative bias. The differences between the recalculated Ext and SAGE II data are within ±25%, which agrees with theoretically determined errors for SCIAMACHY. Ångström exponent ($\alpha_{525/1020}$) differences vary from 40% at 10 km to 10% at 30 km, with SAGE II values being systematically lower. Furthermore, I compared SCIAMACHY Ångström exponents ($\alpha_{750/1530}$) to those from OSIRIS. The relative difference between the instruments is decreasing from 7% at the lowermost altitudes to 4%

at the uppermost altitudes. The absolute values of $\alpha_{750/1530}$ differ by less than 0.2, and both relative and absolute differences are within the theoretically determined errors of $\alpha_{750/1530}$ for those instruments. My time series analysis of the collocated datasets showed that the differences do not change significantly with time and are not correlated with any remarkable events, such as volcanic eruptions. I analyzed on a qualitative level the dependency between R_{mod} and σ from SCIAMACHY and OPCs. This dependency for both instruments is very similar; however, a quantitative assessment is impossible for now.

Case studies

At the end of the thesis, I analyzed in details four volcanic eruptions, as well as one biomass burning event. During the SCIAMACHY lifetime tropical eruptions of Manam and Tavurvur, as well as the extratropical eruption of Sarychev Peak, were taken into consideration. For all three eruptions, *Ext* was analyzed. Additionally, for Manam and Tavurvur the changes in PSD parameters were investigated. The eruption of Kelut and Canadian Wildfires 2017 were studied based on OMPS *Ext* product.

My studies demonstrated that for the tropical eruptions perturbations in *Ext* can reach altitudes higher than 25 km, because of the strong equatorial upwelling caused by the BDC. For all tropical eruptions, the area around the equator acts like a reservoir, from which aerosols are transported to the hemisphere, where the circulation is stronger. I analyzed the circulation patterns based on the monthly mean age of air data from the TOMCAT/SLIMCAT model provided by Prof. Chipperfield. My analysis of the PSD parameters showed, that the R_{mod} increased after an eruption; however, in case of Tavurvur eruption, w also increased because this eruption superposed with the one of Soufriere Hills occurred some months earlier. I also demonstrated that tropical eruptions are associated with the strong tape-recorder effect, which is a result of the transport of aerosol or its precursors with the BDC.

For the extra-tropical increased *Ext* events, the perturbation does not reach as high altitudes as the perturbation in the tropics, however, weak volcanic signatures can still be seen at 25 km. For biomass burning events, even for such strong ones as Canadian Wildfires 2017, perturbations reach maximum 22 km. The tape-recorder effect is not so distinct in the mid-latitudes, because there is no pronounced upwelling at these latitudes. For events occurring in the Northern Hemisphere in the summer season, the Asian Monsoon anticyclone can play an important role, being responsible for the propagation of the perturbation into the tropical region. It was the case for both, Sarychev eruption in June 2009 and Canadian Wildfires in July-August 2017, however, it does not necessarily have to happen. Generally, for the mid-latitudes events the perturbation stays in the hemisphere, where the volcanic eruption or biomass burning occurred.

10.2. Outlook

In the thesis, a lot of problems related to the retrieval of stratospheric aerosol parameters from limb-scatter instruments were discussed. Some of the problems, mostly related to the

aerosol extinction coefficient retrieval, are well known and were mentioned in the previous publications [e.g. Loughman et al., 2018, Rieger et al., 2018] and are actively discussed at the Stratospheric Sulfur and its Role in Climate (SSiRC) community meetings. However, there is a specific plan to improve the products described in the dissertation. Most of the tasks are planned to be solved in the framework of VolImpact research group.

For *Ext* product from SCIAMACHY better cloud filtering should be implemented. For V1.4 SCIAMACHY the values of $Ext_{750} > 0.001$ km^{-1} were considered to be cloud contaminated; however, this approach leads to the partial filtering of volcanic plumes (e.g. in case of Sarychev eruption discussed in Sec. 9.2). For that reason, the new cloud filtering algorithm developed by Liebing [2016] should be used instead. This algorithm, as mentioned in Ch. 8, is based on the statistical approach, which helps to distinguish better between clouds and volcanic plumes. It is planned to try both, pre-retrieval cut-off of the cloud contaminated tangent altitudes as well as post-retrieval filtering.

The improvements of the SCIAMACHY *Ext* product could help as well for the OMPS retrieval. If the Liebing [2016] algorithm shows better results in cloud filtering, it can be adopted to OMPS measurements. However, as the first step, the OMPS V1.0.9 *Ext* retrieval algorithm should be improved. As was mentioned in Sec. 4.2, in the current version Ext_{869} profiles have oscillations. The way of reducing these oscillations should be found.

As soon as OMPS *Ext* product is improved, it would be beneficial to merge it with SCIAMACHY to provide longer-term time series. However, multiple challenges have to be overcome. First, *Ext* products SCIAMACHY V1.4 and OMPS V1.0.9 were obtained at the different wavelengths (750 and 869 nm, respectively). For OMPS use of 750 nm as retrieval wavelength is not sufficient, however, for SCIAMACHY it is possible to reprocess the data at 869 nm. Another challenge is the transfer function: SCIAMACHY and OMPS products have just two-month overlap. This time period is not enough for merging. For that reason, some third source of information should be taken into consideration. The possible candidates are the spaceborne measurements from OSIRIS or CALIOP. However, the measurement techniques of both instrument require additional assumptions for the *Ext* retrieval. The best solution would be to use solar occultation instruments, but in the end of 2000s – beginning of 2010s there was no occultation instrument, which would provide global *Ext* product. There is also a possibility to use stratospheric models outputs, as a transfer function. This approach seems to be the best option, but deeper research should be done in that field.

With respect to PSD parameters, multiple improvements should be made. Firstly, the algorithm should be expanded to the extratropical regions. Second, not only completely cloud free profiles should be taken into consideration, but also cloud contaminated ones. Many studies should be done to implement that, but here the studies done for aerosol extinction coefficient might help as well.

The next step would be to retrieve or put a better constraint on particle number density. One possible way is to combine limb and occultation measurements, using the later to constraint N. Another possibility to constraint or estimate N would be through the use of collocated profiles of stratospheric H_2SO_4 concentrations. For SCIAMACHY the

use of the MIPAS H_2SO_4 aerosol volume density dataset [Günther et al., 2018] might be appropriate. However, synergistic use of the data from two different instruments is not straightforward and is a subject of the further studies.

The adaptation of SCIAMACHY PSD retrieval algorithm to OMPS is quite challenging. As it was highlighted multiple times, OMPS spectral information is rather limited. For that reason, it is believed, that the PSD parameters could be retrieved even with higher uncertainties. It might be possible, though, to retrieve only R_{mod} or obtain the Ångström exponent. Another possibility to improve OMPS stratospheric aerosol product would be through the use of SCIAMACHY PSD parameters climatology in Ext retrieval to minimize the p_a uncertainty. Additionally, SCIAMACHY PSD parameters retrieval algorithm can be applied to the upcoming Atmospheric Limb Tracker for Investigation of the Upcoming Stratosphere (ALTIUS) mission. Nowadays, the mission is planned to be launched in 2022. According to the current plan, ALTIUS will measure in limb viewing geometry, not only in the UV part of the spectrum but also in visible and NIR channel. The wavelengths intervals from 440 to 800 nm as well as from 900 to 1800 nm will be covered, which makes it possible to use SCIAMACHY algorithm for it. The specifications, as well as the exact measurement wavelengths, have not been revealed yet.

At the end, a comprehensive SCIAMACHY PSD product validation is planned to be done. This will be possible as soon as Deshler et al. [2018] will release their new OPCs products. This is believed to provide better information on the fine mode of PSD. Additionally, the OPCs data should be fitted by unimodal distribution all the times to be comparable with SCIAMACHY. The validation of the current SCIAMACHY PSD product can be done, even before the algorithm will be expanded to the other latitudes. This is because during SCIAMACHY lifetime there were three measurement campaigns in Darwin (13° S) in 2005, Teresina (5° S) in 2008 as well as Niamey (13° N) in 2006 and 2008. The measurements from these campaigns should be reprocessed as well.

List of Figures

List of Tables

Abbreviations and acronyms

α Ångtröm exponent

ACE Atmospheric Chemistry Experiment

AERONET Aerosol Robotic Network

ALTIUS Atmospheric Limb Tracker for Investigation of the Upcoming Stratosphere

β_{aer} aerosol extinction cross-section

BDC Brewer-Dobson Circulation

BIRA Belgian Institute for Space Aeronomy

CALIOP Cloud-Aerosol Lidar with Orthogonal Polarization Lidar

CARIBIC Civil Aircraft for Regular Investigation of the Atmosphere Based on an Instrument Container

CCD charge coupled device

ECMWF European Centre for Medium-Range Weather Forecasts

ECSTRA Extinction Coefficient for STRatospheric Aerosol

Envisat Environmental satellite

ERBS Earth Radiation Budget Satellite

ESA European Space Agency

Ext aerosol extinction coefficient

η_a aerosol scattering coefficient

FCAS Focused Cavity Aerosol Spectrometer

GloSSAC Global Space-based Stratospheric Aerosol Climatology

GMAO Global Modelling and Assimilation Office

GOMOS Global Ozone Monitoring by Occultation of Stars

HALOE Halogen Occultation Experiment

$\mathbf{I}_{sol}$ solar irradiance spectrum

ISS International Space Station

IUP Institute of Environmental Physics, University of Bremen

MAESTRO Measurement of Aerosol Extinction in the Stratosphere and Troposphere Retrieved by Occultation

MAP maximum a posteriori probability

MART multiplicative algebraic reconstruction technique

MIPAS Michelson Interferometer for Passive Atmospheric Sounding

N particle number density

NASA National Aeronautics and Space Administration

NIR near-infrared

OE optimal estimation

OMI Ozone Monitoring Instrument

OMPS Ozone Mapper and Profiler Suite

OPAC Optical Properties of Aerosols and Clouds

OPC Optical Particle Counter

OSIRIS Optical Spectrograph and InfraRed Imager System

p_a aerosol phase function

POAM Polar Ozone and Aerosol Measurement

PSCs Polar Stratospheric Clouds

PSD particle size distribution

QBO quasi-biennial oscillation

r_{eff} effective radius

r_{med} median radius

R_{mod} mode radius

RTM radiative transfer model

σ distribution width parameter

SAGE Stratospheric Aerosol and Gas Experiment

SAM Stratospheric Aerosol Measurement

SCIAMACHY Scanning Imaging Absorption Spectrometer for Atmospheric Chartography

SSA solar scattering angle

SSiRC Stratospheric Sulfur and its Role in Climate

SNPP Suomi National Polar-orbiting Partnership

TP tangent point

UHSAS Ultra-High Sensitivity Aerosol Spectrometer

USask University of Saskatchewan

UTLS Upper Troposphere Lower Stratosphere

UV ultraviolet

VEI Volcanic Explosivity Index

w absolute distribution width

References

ACE-MAESTRO-Team. ACE-MAESTRO level 2 version 3.13 data description and file format, 2018. URL https://databace.scisat.ca/level2/mae_v3.13/ACE-MAESTRO-V3.13-Data.pdf.

A. Ångström. On the atmospheric transmission of sun radiation and on dust in the air. *Geografiska Annaler*, 11(2):156–166, 1929.

A. Ansmann, H. Baars, A. Chudnovsky, I. Mattis, I. Veselovskii, M. Haarig, P. Seifert, R. Engelmann, and U. Wandinger. Extreme levels of Canadian wildfire smoke in the stratosphere over central Europe on 21–22 august 2017. *Atmospheric Chemistry and Physics*, 18(16):11831–11845, 2018. doi: 10.5194/acp-18-11831-2018. URL https://www.atmos-chem-phys.net/18/11831/2018/.

C. Arosio, A. Rozanov, E. Malinina, K.-U. Eichmann, T. von Clarmann, and J. P. Burrows. Retrieval of ozone profiles from OMPS limb scattering observations. *Atmospheric Measurement Techniques*, 11(4):2135–2149, 2018. doi: 10.5194/amt-11-2135-2018. URL https://www.atmos-meas-tech.net/11/2135/2018/.

B.R. Barkstrom and G.L. Smith. The earth radiation budget experiment: Science and implementation. *Reviews of Geophysics*, 24(2):379–390, 1986.

R. Bauer, A. Rozanov, C. A. McLinden, L. L. Gordley, W. Lotz, J. M. Russell III, K. A. Walker, J. M. Zawodny, A. Ladstätter-Weißenmayer, H. Bovensmann, and J. P. Burrows. Validation of SCIAMACHY limb NO_2 profiles using solar occultation measurements. *Atmospheric Measurement Techniques*, 5(5):1059–1084, 2012. doi: 10.5194/amt-5-1059-2012. URL https://www.atmos-meas-tech.net/5/1059/2012/.

P.K. Bhartia, Glenn Jaross, Jack Larsen, and Al Fleig. Science team evaluation of the OMPS limb profiler. Technical report, NASA, 2013.

C. Bingen, D. Fussen, and F. Vanhellemont. A global climatology of stratospheric aerosol size distribution parameters derived from SAGE II data over the period 1984–2000: 1. methodology and climatological observations. *Journal of Geophysical Research: Atmospheres*, 109(D6), 2004.

C. Bingen, C.E. Robert, K. Stebel, C. Brühl, J. Schallock, F. Vanhellemont, N. Mateshvili, M. Höpfner, T. Trickl, J.E. Barnes, et al. Stratospheric aerosol data records for the climate change initiative: Development, validation and application to chemistry-climate modelling. *Remote Sensing of Environment*, 2017.

S.E. Bishop. The remarkable sunsets. *Nature*, 29(755):573, 1884.

A. E. Bourassa, C. A. McLinden, C. E. Sioris, S. Brohede, A. F. Bathgate, E. J. Llewellyn, and D. A. Degenstein. Fast NO_2 retrievals from Odin-OSIRIS limb scatter measurements. *Atmospheric Measurement Techniques*, 4(5):965–972, 2011. doi: 10.5194/amt-4-965-2011. URL `https://www.atmos-meas-tech.net/4/965/2011/`.

A. E. Bourassa, C. Z. Roth, D. J. Zawada, L. A. Rieger, C. A. McLinden, and D. A. Degenstein. Drift-corrected Odin-OSIRIS ozone product: algorithm and updated stratospheric ozone trends. *Atmospheric Measurement Techniques*, 11(1):489–498, 2018. doi: 10.5194/amt-11-489-2018. URL `https://www.atmos-meas-tech.net/11/489/2018/`.

A.E. Bourassa, L.A. Rieger, N.D. Lloyd, and D.A. Degenstein. Odin-OSIRIS stratospheric aerosol data product and SAGE III intercomparison. *Atmospheric Chemistry and Physics*, 12(1):605–614, 2012.

H. Bovensmann, J.P. Burrows, M. Buchwitz, J. Frerick, S. Noël, V.V. Rozanov, K.V. Chance, and A.P.H. Goede. SCIAMACHY: Mission objectives and measurement modes. *Journal of the Atmospheric Sciences*, 56(2):127–150, 1999.

C. A. M. Brenninkmeijer, P. Crutzen, F. Boumard, T. Dauer, B. Dix, R. Ebinghaus, D. Filippi, H. Fischer, H. Franke, U. Frieβ, J. Heintzenberg, F. Helleis, M. Hermann, H. H. Kock, C. Koeppel, J. Lelieveld, M. Leuenberger, B. G. Martinsson, S. Miemczyk, H. P. Moret, H. N. Nguyen, P. Nyfeler, D. Oram, D. O'Sullivan, S. Penkett, U. Platt, M. Pupek, M. Ramonet, B. Randa, M. Reichelt, T. S. Rhee, J. Rohwer, K. Rosenfeld, D. Scharffe, H. Schlager, U. Schumann, F. Slemr, D. Sprung, P. Stock, R. Thaler, F. Valentino, P. van Velthoven, A. Waibel, A. Wandel, K. Waschitschek, A. Wiedensohler, I. Xueref-Remy, A. Zahn, U. Zech, and H. Ziereis. Civil aircraft for the regular investigation of the atmosphere based on an instrumented container: The new CARIBIC system. *Atmospheric Chemistry and Physics*, 7(18):4953–4976, 2007. doi: 10.5194/acp-7-4953-2007. URL `https://www.atmos-chem-phys.net/7/4953/2007/`.

L.A. Brinkhoff, A. Rozanov, R. Hommel, C. von Savigny, F. Ernst, H. Bovensmann, and J.P. Burrows. Ten-year SCIAMACHY stratospheric aerosol data record: Signature of the secondary meridional circulation associated with the quasi-biennial oscillation. In *Towards an Interdisciplinary Approach in Earth System Science*, pages 49–58. Springer, 2015.

M. I. Budyko. *Izmenenie klimata*. Gidrometeoizdat, 1974.

J.P. Burrows, E. Hölzle, A.P.H. Goede, H. Visser, and W. Fricke. SCIAMACHY—scanning imaging absorption spectrometer for atmospheric chartography. *Acta Astronautica*, 35(7):445–451, 1995.

Z. Chen, P. K. Bhartia, R. Loughman, P. Colarco, and M. DeLand. Improvement of stratospheric aerosol extinction retrieval from OMPS/LP using a new aerosol model. *Atmospheric Measurement Techniques*, 11(12):6495–6509, 2018. doi: 10.5194/amt-11-6495-2018. URL `https://www.atmos-meas-tech.net/11/6495/2018/`.

M. P. Chipperfield. New version of the TOMCAT/SLIMCAT off-line chemical transport model: Intercomparison of stratospheric tracer experiments. *Quarterly Journal of the Royal Meteorological Society*, 132(617):1179–1203, 2006. doi: 10.1256/qj.05.51. URL `https://rmets.onlinelibrary.wiley.com/doi/abs/10.1256/qj.05.51`.

J.F. Cronin. Recent volcanism and the stratosphere. *Science*, 172(3985):847–849, 1971.

E.L. Crow and K. Shimizu. Lognormal distributions: Theory and practice. *Marcel Decker*, 1988.

P.J. Crutzen. The possible importance of CSO for the sulfate layer of the stratosphere. *Geophysical research letters*, 3(2):73–76, 1976.

P.J. Crutzen. Albedo enhancement by stratospheric sulfur injections: A contribution to resolve a policy dilemma? *Climatic change*, 77(3):211–220, 2006.

R.P. Damadeo, J.M. Zawodny, L.W. Thomason, and N. Iyer. SAGE version 7.0 algorithm: application to SAGE II. *Atmospheric Measurement Techniques*, 6(12):3539–3561, 2013.

M. DeLand, P.K. Bhartia, P. Xu, and T. Zhu. OMPS limb profiler aerosol extinction product AER675: Version 0.5 data release notes, 2016. URL `https://ozoneaq.gsfc.nasa.gov/media/docs/OMPS_LP_AER675_V0.5_Release_Notes.pdf`.

T. Deshler. A review of global stratospheric aerosol: Measurements, importance, life cycle, and local stratospheric aerosol. *Atmospheric Research*, 90(2):223–232, 2008.

T. Deshler, M.E. Hervig, D.J. Hofmann, J.M. Rosen, and J.B. Liley. Thirty years of in situ stratospheric aerosol size distribution measurements from Laramie, Wyoming (41 n), using balloon-borne instruments. *Journal of Geophysical Research: Atmospheres*, 108(D5), 2003.

T. Deshler, M. Kovilakam, B. Lou, T. Peter, L. Kalnajs, and D. Degenstein. Retrieval of aerosol size distributions from in situ particle counter measurements accounting for instrument counting efficiency, and comparisons with satellite measurements of extinction and estimates of aerosol surface area. Planned to be submitted to J. Geophys. Res., 2018.

O. Dubovik, A. Smirnov, B.N. Holben, M.D. King, Y.J. Kaufman, T.F. Eck, and I. Slutsker. Accuracy assessments of aerosol optical properties retrieved from Aerosol Robotic Network (AERONET) Sun and sky radiance measurements. *Journal of Geophysical Research: Atmospheres*, 105(D8):9791–9806, 2000.

K.-U. Eichmann, L. Lelli, C. von Savigny, H. Sembhi, and J.P. Burrows. Global cloud top height retrieval using SCIAMACHY limb spectra: model studies and first results. *Atmospheric Measurement Techniques*, 9:793–815, 2016.

A. Engel, T. Möbius, H. Bönisch, U. Schmidt, R. Heinz, I. Levin, E. Atlas, S. Aoki, T. Nakazawa, S. Sugawara, et al. Age of stratospheric air unchanged within uncertainties over the past 30 years. *Nature Geoscience*, 2(1):28, 2009.

F. Ernst. *Stratospheric aerosol extinction profile retrievals from SCIAMACHY limb-scatter observations*. PhD thesis, Staats-und Universitätsbibliothek Bremen, 2013.

F. Ernst, C. von Savigny, A. Rozanov, V. Rozanov, K.-U. Eichmann, L.A. Brinkhoff, H. Bovensmann, and J.P. Burrows. Global stratospheric aerosol extinction profile retrievals from SCIAMACHY limb-scatter observations. *Atmospheric Measurement Techniques Discussions*, 5(4):5993–6035, 2012.

H. Fischer, M. Birk, C. Blom, B. Carli, M. Carlotti, T. von Clarmann, L. Delbouille, A. Dudhia, D. Ehhalt, M. Endemann, et al. MIPAS: an instrument for atmospheric and climate research. *Atmospheric Chemistry and Physics*, 8(8):2151–2188, 2008.

M. Fromm, D.T. Lindsey, R. Servranckx, G. Yue, T. Trickl, R. Sica, P. Doucet, and S. Godin-Beekmann. The untold story of pyrocumulonimbus. *Bulletin of the American Meteorological Society*, 91(9):1193–1210, 2010.

D. Fussen and C. Bingen. Volcanism dependent model for the extinction profile of stratospheric aerosols in the uv-visible range. *Geophysical research letters*, 26(6):703–706, 1999.

J.C. Fyfe, K. von Salzen, J.N.S. Cole, N.P. Gillett, and J.-P. Vernier. Surface response to stratospheric aerosol changes in a coupled atmosphere–ocean model. *Geophysical Research Letters*, 40(3):584–588, 2013.

M. Gottwald and H. Bovensmann. *SCIAMACHY - Exploring the Changing Earth's Atmosphere*. Springer, Dordrecht, 2011. ISBN 9789048198962. doi: 10.1007/978-90-481-9896-2.

R.G. Grainger. Some useful formulae for aerosol size distributions and optical properties, 2018. URL `http://eodg.atm.ox.ac.uk/user/grainger/research/aerosols.pdf`.

R.G. Grainger, A. Lambert, C.D. Rodgers, F.W. Taylor, and T. Deshler. Stratospheric aerosol effective radius, surface area and volume estimated from infrared measurements. *Journal of Geophysical Research: Atmospheres*, 100(D8):16507–16518, 1995.

A. Günther, M. Höpfner, B.-M. Sinnhuber, S. Griessbach, T. Deshler, T. von Clarmann, and G. Stiller. MIPAS observations of volcanic sulfate aerosol and sulfur dioxide in the stratosphere. *Atmospheric Chemistry and Physics*, 18(2):1217–1239, 2018.

J.E. Hansen and L.D. Travis. Light scattering in planetary atmospheres. *Space Science Reviews*, 16(4):527–610, 1974.

M. Hess, P. Koepke, and I. Schult. Optical properties of aerosols and clouds: The software package OPAC. *Bulletin of the American meteorological society*, 79(5):831–844, 1998.

M.H. Hitchman, M. McKay, and C.R. Trepte. A climatology of stratospheric aerosol. *Journal of Geophysical Research: Atmospheres*, 99(D10):20689–20700, 1994.

D. Hofmann, J. Barnes, M. O'Neill, M. Trudeau, and R. Neely. Increase in background stratospheric aerosol observed with lidar at mauna loa observatory and boulder, colorado. *Geophysical Research Letters*, 36(15), 2009.

A.R. Hogg. The mount agung eruption and atmospheric turbidity. *Australian J. Sci*, 26 (4):119–120, 1963.

R.J. Holton. An introduction to dynamic meteorology, 2004.

M. Höpfner, C. D. Boone, B. Funke, N. Glatthor, U. Grabowski, A. Günther, S. Kellmann, M. Kiefer, A. Linden, S. Lossow, H. C. Pumphrey, W. G. Read, A. Roiger, G. Stiller, H. Schlager, T. von Clarmann, and K. Wissmüller. Sulfur dioxide (SO_2) from MIPAS in the upper troposphere and lower stratosphere 2002–2012. *Atmospheric Chemistry and Physics*, 15(12):7017–7037, 2015. doi: 10.5194/acp-15-7017-2015. URL `https://www.atmos-chem-phys.net/15/7017/2015/`.

IPCC. *Climate Change 2013: The Physical Science Basis. Contribution of Working Group I to the Fifth Assessment Report of the Intergovernmental Panel on Climate Change*. Cambridge University Press, Cambridge, United Kingdom and New York, NY, USA, 2013. ISBN ISBN 978-1-107-66182-0. doi: 10.1017/CBO9781107415324. URL `www.climatechange2013.org`.

D.J. Ivy, S. Solomon, D. Kinnison, M.J. Mills, A. Schmidt, and R.R. Neely. The influence of the calbuco eruption on the 2015 antarctic ozone hole in a fully coupled chemistry-climate model. *Geophysical Research Letters*, 44(5):2556–2561, 2017.

H. Jäger. Long-term record of lidar observations of the stratospheric aerosol layer at garmisch-partenkirchen. *Journal of Geophysical Research: Atmospheres*, 110(D8), 2005.

G. Jaross, P. K. Bhartia, G. Chen, M. Kowitt, M. Haken, Z. Chen, P. Xu, J. Warner, and T. Kelly. OMPS limb profiler instrument performance assessment. *Journal of Geophysical Research: Atmospheres*, 119(7):4399–4412, 2014. ISSN 2169-8996. doi: 10.1002/2013JD020482. URL `http://dx.doi.org/10.1002/2013JD020482`.

J. Jia, A. Rozanov, A. Ladstätter-Weißenmayer, and J. P. Burrows. Global validation of SCIAMACHY limb ozone data (versions 2.9 and 3.0, iup bremen) using ozonesonde measurements. *Atmospheric Measurement Techniques*, 8(8):3369–3383, 2015. doi: 10.5194/amt-8-3369-2015. URL `https://www.atmos-meas-tech.net/8/3369/2015/`.

N.L. Johnson, S. Kotz, and N. Balakrishnan. Continuous univariate distributions, 1994.

P.D. Jones and Y. Bayazitoglu. Coordinate systems for the radiative transfer equation in curvilinear media. *Journal of Quantitative Spectroscopy and Radiative Transfer*, 48(4): 427–440, 1992.

C.E. Junge and J.E. Manson. Stratospheric aerosol studies. *Journal of Geophysical Research*, 66(7):2163–2182, 1961.

C.E. Junge, C.W. Chagnon, and J.E. Manson. Stratospheric aerosols. *Journal of Meteorology*, 18(1):81–108, 1961.

S.M. Khaykin, S. Godin-Beekmann, A. Hauchecorne, J. Pelon, F. Ravetta, and P. Keckhut. Stratospheric smoke with unprecedentedly high backscatter observed by lidars above southern france. *Geophysical Research Letters*, 45(3):1639–1646, 2018.

B. Kravitz, A. Robock, A. Bourassa, T. Deshler, D. Wu, I. Mattis, F. Finger, A. Hoffmann, C. Ritter, L. Bitar, et al. Simulation and observations of stratospheric aerosols from the 2009 Sarychev volcanic eruption. *Journal of Geophysical Research: Atmospheres*, 116(D18), 2011.

S. Kremser, L.W. Thomason, M. Hobe, M. Hermann, T. Deshler, C. Timmreck, M. Toohey, A. Stenke, J.P. Schwarz, R. Weigel, et al. Stratospheric aerosol—observations, processes, and impact on climate. *Reviews of Geophysics*, 2016.

S. Kühl, J. Pukite, T. Deutschmann, U. Platt, and T. Wagner. SCIAMACHY limb measurements of NO2, BrO and OClO. retrieval of vertical profiles: Algorithm, first results, sensitivity and comparison studies. *Advances in Space Research*, 42(10):1747–1764, 2008.

C. Li, N. A. Krotkov, S. Carn, Y. Zhang, R. J. D. Spurr, and J. Joiner. New-generation NASA Aura Ozone Monitoring Instrument (OMI) volcanic SO_2 dataset: algorithm description, initial results, and continuation with the suomi-npp ozone mapping and profiler suite (OMPS). *Atmospheric Measurement Techniques*, 10(2):445–458, 2017. doi: 10.5194/amt-10-445-2017. URL `https://www.atmos-meas-tech.net/10/445/2017/`.

P. Liebing. New limb cloud detection algorithm theoretical basis document, 2016. URL `http://www.iup.uni-bremen.de/~patty/Limb_Clouds/atbd_limbcloudsV2.pdf`.

K.-N. Liou. *An introduction to atmospheric radiation*, volume 84. Elsevier, 2002.

E.J. Llewellyn, N.D. Lloyd, D.A. Degenstein, R.L. Gattinger, S.V. Petelina, A.E. Bourassa, J.T. Wiensz, E.V. Ivanov, I.C. McDade, B.H. Solheim, et al. The OSIRIS instrument on the odin spacecraft. *Canadian Journal of Physics*, 82(6):411–422, 2004.

R. Loughman, P. K. Bhartia, Z. Chen, P. Xu, E. Nyaku, and G. Taha. The ozone mapping and profiler suite (OMPS) limb profiler (LP) version 1 aerosol extinction retrieval algorithm: theoretical basis. *Atmospheric Measurement Techniques*, 11(5):2633–2651, 2018. doi: 10.5194/amt-11-2633-2018. URL `https://www.atmos-meas-tech.net/11/2633/2018/`.

E. Malinina, A. Rozanov, L. Rieger, A. Bourassa, H. Bovensmann, J. P. Burrows, and D. Degenstein. Stratospheric aerosol characteristics from space-borne observations: extinction coefficient and ångström exponent. *Atmospheric Measurement Techniques Discussions*, 2018:1–28, 2018a. doi: 10.5194/amt-2018-328. URL `https://www.atmos-meas-tech-discuss.net/amt-2018-328/`.

E. Malinina, A. Rozanov, V. Rozanov, P. Liebing, H. Bovensmann, and J. P. Burrows. Aerosol particle size distribution in the stratosphere retrieved from SCIAMACHY limb measurements. *Atmospheric Measurement Techniques*, 11(4):2085–2100, 2018b. doi: 10.5194/amt-11-2085-2018. URL `https://www.atmos-meas-tech.net/11/2085/2018/`.

M.P. McCormick. SAGE II: an overview. *Advances in Space Research*, 7(3):219–226, 1987.

C.A. McLinden, A.E. Bourassa, S. Brohede, M. Cooper, D.A. Degenstein, W.J.F. Evans, R.L. Gattinger, C.S. Haley, E.J. Llewellyn, N.D. Lloyd, et al. OSIRIS: A decade of scattered light. *Bulletin of the American Meteorological Society*, 93(12):1845–1863, 2012.

G. Mie. Beiträge zur optik trüber medien, speziell kolloidaler metallösungen. *Annalen der physik*, 330(3):377–445, 1908.

S. Noël, H. Bovensmann, M.W. Wuttke, J.P. Burrows, M. Gottwald, E. Krieg, A.P.H. Goede, and C. Muller. Nadir, limb, and occultation measurements with SCIAMACHY. *Advances in Space Research*, 29(11):1819–1824, 2002.

S. Oberländer, U. Langematz, and S. Meul. Unraveling impact factors for future changes in the Brewer-Dobson circulation. *Journal of Geophysical Research: Atmospheres*, 118 (18):10–296, 2013.

Clive Oppenheimer. Climatic, environmental and human consequences of the largest known historic eruption: Tambora volcano (indonesia) 1815. *Progress in physical geography*, 27(2):230–259, 2003.

M. Park, W. J. Randel, A. Gettelman, S.T. Massie, and J.H. Jiang. Transport above the asian summer monsoon anticyclone inferred from Aura Microwave Limb Sounder tracers. *Journal of Geophysical Research: Atmospheres*, 112(D16), 2007.

T. Popp, G. De Leeuw, C. Bingen, C. Brühl, V. Capelle, A. Chedin, L. Clarisse, O. Dubovik, R. Grainger, J. Griesfeller, et al. Development, production and evaluation of aerosol climate data records from european satellite observations (aerosol_cci). *Remote sensing*, 8(5):421, 2016.

W.J. Randel, M. Park, L. Emmons, D. Kinnison, P. Bernath, K.A. Walker, C. Boone, and H. Pumphrey. Asian monsoon transport of pollution to the stratosphere. *Science*, 328(5978):611–613, 2010.

P. J. Rasch, S. Tilmes, R.P. Turco, A. Robock, L. Oman, C.-C. J Chen, G.L. Stenchikov, and R.R. Garcia. An overview of geoengineering of climate using stratospheric sulphate aerosols. *Philosophical Transactions of the Royal Society of London A: Mathematical, Physical and Engineering Sciences*, 366(1882):4007–4037, 2008.

L. A. Rieger, E. P. Malinina, A. V. Rozanov, J. P. Burrows, A. E. Bourassa, and D. A. Degenstein. A study of the approaches used to retrieve aerosol extinction, as applied to limb observations made by OSIRIS and SCIAMACHY. *Atmospheric Measurement Techniques Discussions*, 2018:1–21, 2018. doi: 10.5194/amt-2017-446. URL `https://www.atmos-meas-tech-discuss.net/amt-2017-446/`.

L.A. Rieger, A.E. Bourassa, and D.A. Degenstein. Stratospheric aerosol particle size information in Odin-OSIRIS limb scatter spectra. *Atmospheric Measurement Techniques*, 7(2):507–522, 2014.

L.A. Rieger, A.E. Bourassa, and D.A. Degenstein. Merging the OSIRIS and SAGE II stratospheric aerosol records. *Journal of Geophysical Research: Atmospheres*, 120(17): 8890–8904, 2015.

A. Robock. Important research questions on volcanic eruptions and climate. *Past Global Changes Magazine*, 23(2):68, 2015. doi: 10.22498/pages.23.2.68.

A. Robock and J. Mao. The volcanic signal in surface temperature observations. *Journal of Climate*, 8(5):1086–1103, 1995.

C.D. Rodgers. *Inverse methods for atmospheric sounding: theory and practice*, volume 2. World scientific, 2000.

A. Rozanov. Modeling of radiative transfer through a spherical planetary atmosphere. 2001.

A. Rozanov, S. Kühl, A. Doicu, C. McLinden, J. Pukite, H. Bovensmann, J. P. Burrows, T. Deutschmann, M. Dorf, F. Goutail, K. Grunow, F. Hendrick, M. von Hobe, S. Hrechanyy, G. Lichtenberg, K. Pfeilsticker, J. P. Pommereau, M. Van Roozendael, F. Stroh, and T. Wagner. Bro vertical distributions from sciamachy limb measurements: comparison of algorithms and retrieval results. *Atmospheric Measurement Techniques*, 4(7):1319–1359, 2011a. doi: 10.5194/amt-4-1319-2011. URL `https://www.atmos-meas-tech.net/4/1319/2011/`.

A. Rozanov, K. Weigel, H. Bovensmann, S. Dhomse, K.-U. Eichmann, R. Kivi, V. Rozanov, H. Vömel, M. Weber, and J.P. Burrows. Retrieval of water vapor vertical distributions in the upper troposphere and the lower stratosphere from SCIAMACHY limb measurements. *Atmospheric Measurement Techniques*, 4(5):933–954, 2011b.

V.V. Rozanov, A.V. Rozanov, A.A. Kokhanovsky, and J.P. Burrows. Radiative transfer through terrestrial atmosphere and ocean: software package SCIATRAN. *Journal of Quantitative Spectroscopy and Radiative Transfer*, 133:13–71, 2014.

M. Sato, J.E. Hansen, M.P. McCormick, and J.B. Pollack. Stratospheric aerosol optical depths, 1850–1990. *Journal of Geophysical Research: Atmospheres*, 98(D12):22987–22994, 1993.

S. Self, R. Gertisser, Th. Thordarson, M.R. Rampino, and J.A. Wolff. Magma volume, volatile emissions, and stratospheric aerosols from the 1815 eruption of tambora. *Geophysical Research Letters*, 31(20), 2004.

J.M. Siddaway and S.V. Petelina. Transport and evolution of the 2009 australian black saturday bushfire smoke in the lower stratosphere observed by OSIRIS on Odin. *Journal of Geophysical Research: Atmospheres*, 116(D6), 2011.

Smithsonian Institution. Global volcanism program database, 2017. URL `http://volcano.si.edu/search_eruption.cfm`.

S. Solomon. Stratospheric ozone depletion: A review of concepts and history. *Reviews of Geophysics*, 37(3):275–316, 1999.

S. Solomon, J.S. Daniel, R.R.III Neely, J.-P. Vernier, E.G. Dutton, and L.W. Thomason. The persistently variable "background" stratospheric aerosol layer and global climate change. *Science*, 333(6044):866–870, 2011.

G. Taha, D.F. Rault, R.P. Loughman, A.E. Bourassa, and C. von Savigny. SCIAMACHY stratospheric aerosol extinction profile retrieval using the OMPS/LP algorithm. *Atmospheric Measurement Techniques*, 4(3):547–556, 2011.

S. Tegtmeier, M.I. Hegglin, J. Anderson, A. Bourassa, S. Brohede, D. Degenstein, L. Froidevaux, R. Fuller, B. Funke, J. Gille, et al. SPARC data initiative: A comparison of ozone climatologies from international satellite limb sounders. *Journal of Geophysical Research: Atmospheres*, 118(21):12–229, 2013.

L. Thomason and Th. Peter. SPARC Assessment of Stratospheric Aerosol Properties (ASAP). Technical report, SPARC, 2006. URL `http://www.sparc-climate.org/publications/sparc-reports/`.

L. W. Thomason, S. P. Burton, B.-P. Luo, and T. Peter. SAGE II measurements of stratospheric aerosol properties at non-volcanic levels. *Atmospheric Chemistry and Physics*, 8(4):983–995, 2008. doi: 10.5194/acp-8-983-2008. URL `https://www.atmos-chem-phys.net/8/983/2008/`.

L. W. Thomason, N. Ernest, L. Millán, L. Rieger, A. Bourassa, J.-P. Vernier, G. Manney, B. Luo, F. Arfeuille, and T. Peter. A global space-based stratospheric aerosol climatology: 1979–2016. *Earth System Science Data*, 10(1):469–492, 2018. doi: 10.5194/essd-10-469-2018. URL `https://www.earth-syst-sci-data.net/10/469/2018/`.

L.W. Thomason and L.R. Poole. Use of stratospheric aerosol properties as diagnostics of antarctic vortex processes. *Journal of Geophysical Research: Atmospheres*, 98(D12): 23003–23012, 1993.

C.R. Trepte and M.H. Hitchman. Tropical stratospheric circulation deduced from satellite aerosol data. *Nature*, 355(6361):626, 1992.

S. Twomey. *Introduction to the mathematics of inversion in remote sensing and indirect measurements*, volume 3. Elsevier, 1977.

F. Vanhellemont, N. Mateshvili, L. Blanot, C.E. Robert, C. Bingen, V. Sofieva, F. Dalaudier, C. Tétard, D. Fussen, E. Dekemper, et al. AerGOM, an improved algorithm for stratospheric aerosol extinction retrieval from GOMOS observations–part 1: Algorithm description. *Atmospheric Measurement Techniques*, 9(9):4687–4700, 2016.

J.-P. Vernier, L.W. Thomason, and J. Kar. CALIPSO detection of an asian tropopause aerosol layer. *Geophysical Research Letters*, 38(7), 2011.

J.-P. Vernier, T.D. Fairlie, T. Deshler, M. Natarajan, T. Knepp, K. Foster, F.G. Wienhold, K.M. Bedka, L. Thomason, and C. Trepte. In situ and space-based observations of the kelud volcanic plume: The persistence of ash in the lower stratosphere. *Journal of Geophysical Research: Atmospheres*, 121(18), 2016.

F.E. Volz. Twilight phenomena caused by the eruption of agung volcano. *Science*, 144 (3622):1121–1122, 1964.

C. von Savigny, F. Ernst, A. Rozanov, R. Hommel, K.-U. Eichmann, V. Rozanov, J.P. Burrows, and L.W. Thomason. Improved stratospheric aerosol extinction profiles from SCIAMACHY: validation and sample results. *Atmospheric Measurement Techniques*, 8(12):5223–5235, 2015.

S.F. Watts. The mass budgets of carbonyl sulfide, dimethyl sulfide, carbon disulfide and hydrogen sulfide. *Atmospheric Environment*, 34(5):761–779, 2000.

K. Weigel, A. Rozanov, F. Azam, K. Bramstedt, R. Damadeo, K.-U. Eichmann, C. Gebhardt, D. Hurst, M. Kraemer, S. Lossow, W. Read, N. Spelten, G. P. Stiller, K. A. Walker, M. Weber, H. Bovensmann, and J. P. Burrows. UTLS water vapour from SCIAMACHY limb measurements v3.01 (2002–2012). *Atmospheric Measurement Techniques*, 9(1):133–158, 2016. doi: 10.5194/amt-9-133-2016. URL `https://www.atmos-meas-tech.net/9/133/2016/`.

J. C. Willson, D Axisa, S. Borrmann, C. Brock, R. Gao, H. Johnson, A. Kupc, M. Reeves, and C. Williamson. In situ measurements of stratospheric aerosol size distribution. In *Workshop on the Measurement of Stratospheric Aerosol*, 2017.

D. J. Zawada, L. A. Rieger, A. E. Bourassa, and D. A. Degenstein. Tomographic retrievals of ozone with the OMPS limb profiler: algorithm description and preliminary results. *Atmospheric Measurement Techniques*, 11(4):2375–2393, 2018. doi: 10.5194/amt-11-2375-2018. URL `https://www.atmos-meas-tech.net/11/2375/2018/`.

D.J. Zawada, S.R. Dueck, L.A. Rieger, A.E. Bourassa, N.D. Lloyd, and D.A. Degenstein. High-resolution and monte carlo additions to the SASKTRAN radiative transfer model. *Atmospheric Measurement Techniques*, 8(6):2609–2623, 2015.